LA-13160-MS

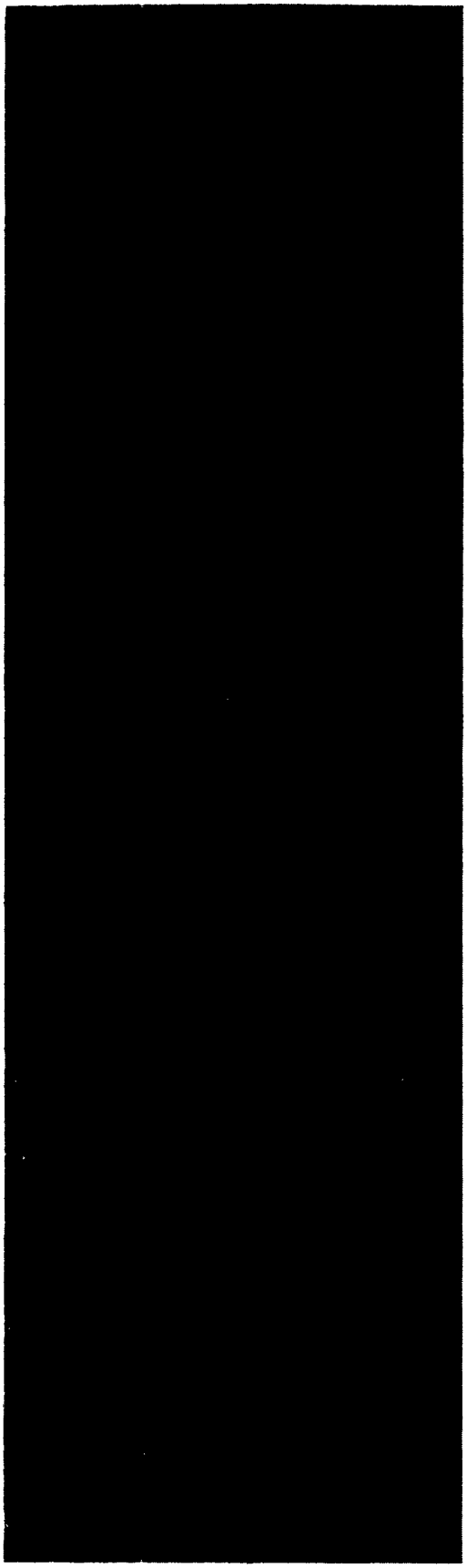

Predictions of Tracer Transport in Interwell Tracer Tests at the C-Hole Complex

Yucca Mountain Site Characterization Project Report Milestone 4077

Los Alamos
NATIONAL LABORATORY

Los Alamos National Laboratory is operated by the University of California for the United States Department of Energy under contract W-7405-ENG-36.

This work was supported by the Yucca Mountain Site Characterization Office as part of the Civilian Radioactive Waste Management Program. This project is managed by the U.S. Department of Energy, Yucca Mountain Site Characterization Project.

An Affirmative Action/Equal Opportunity Employer

LA-13160-MS

UC-814
Issued: September 1996

Predictions of Tracer Transport in Interwell Tracer Tests at the C-Hole Complex

Yucca Mountain Site Characterization Project Report
Milestone 4077

Paul W. Reimus

Los Alamos
NATIONAL LABORATORY
Los Alamos, New Mexico 87545

Table of Contents

PREDICTIONS OF TRACER TRANSPORT IN INTERWELL TRACER TESTS AT THE C-HOLE COMPLEX

Yucca Mountain Site Characterization Project Report
Milestone 4077

by

Paul W. Reimus

ABSTRACT

Particle-tracking models were developed to simulate conservative and reactive tracer transport in interwell tracer tests in the saturated, fractured media at the C-Hole complex near Yucca Mountain, Nevada. Because there is little existing data at the C-Holes to support estimates of a nonhomogeneous or anisotropic hydraulic conductivity field, the models assume that the media are homogeneous and isotropic. However, dual porosity effects, such as matrix diffusion and borehole storage effects, which may be very important at the C-Holes because of the large injection interval volumes relative to injected volumes of tracer solution, are accounted for in the models. Simulations were conducted to investigate sensitivities to (1) type of tracer (fracture flow only, nonsorbing solute, sorbing solute), (2) injection/ production strategy (flow rates and durations), (3) injection well (C#1 or C#2), (4) fracture porosity, (5) matrix porosity, (6) average fracture aperture, (7) sorption parameter (K_d), (8) solute diffusion coefficient, (9) formation dispersivity, and (10) whether the aquifer being tested can be considered confined or unconfined (i.e., 2-D and 3-D models).

The simulations suggest that the most direct approach to studying the effects of solute matrix diffusion and sorption at the C-Holes is to conduct multiple tracer tests at different flow rates in the same formation and between the same two wells (other formations and other wells could be tested later). Conceptual models that account for solute matrix diffusion and sorption in saturated, fractured media would be tested by observing and interpreting differences in (1) breakthrough curves of different tracers in the same test and (2) breakthrough curves of the same tracers in tests at different flow rates. In order to ensure that differences in breakthrough curves from different tests can be attributed primarily to

matrix diffusion and/or sorption, it is essential that all tests be conducted with a minimal amount of tracer holdup in the injection boreholes, and that tests at different flow rates be conducted in such a way that flow field dispersion (that is, dispersion due to flow streamlines of different lengths and velocities) is approximately the same in each test. These criteria can best be met by conducting fully-recirculating tests at different flow rates. However, practical considerations at the C-Holes (and in fully-recirculating tests, in general) suggest that it may be better to conduct convergent tracer tests at different flow rates, with the provision that tracer injection be followed by a water chase of at least two injection interval volumes to ensure that the tracer is flushed out of the injection borehole.

1.0 INTRODUCTION

This report presents predictions of tracer transport in interwell tracer tests that are to be conducted at the C-Hole complex at the Nevada Test Site on behalf of the Yucca Mountain Site Characterization Project. The predictions are used to make specific recommendations about the manner in which the tracer tests should be conducted to best satisfy the needs of the Project. The objective of the tracer tests is to study flow and species transport under saturated conditions in the fractured tuffs near Yucca Mountain, Nevada, the site of a potential high-level nuclear waste repository. The potential repository will be located in the unsaturated zone within Yucca Mountain. The saturated zone beneath and around the mountain represents the final barrier to transport to the accessible environment that radionuclides will encounter if they breach the engineered barriers within the repository and the barriers to flow and transport provided by the unsaturated zone. Background information on the C-Holes is provided in Section 1.1, and the planned tracer testing program is discussed in Section 1.2.

1.1 Background

The C-Holes (UE-25 C#1, UE-25 C#2, and UE-25 C#3; henceforth referred to as C#1, C#2, and C#3) are located in an easterly draining valley near Bow Ridge, approximately 1.5 miles east of the proposed eastern edge of the potential repository within Yucca Mountain. The holes were drilled in 1983 and 1984 and have since been extensively logged and hydrologically tested by the United States Geological Survey (USGS). Each well penetrates to approximately 900 m below the surface, with the water table being approximately 400 m below surface. The surface configuration of the wells and a summary of the well coordinates at depth is shown in Fig. 1. Figure 2 illustrates the vertical stratigraphy and lithology at the C-Holes below the water table. The water table occurs essentially at the boundary between the Topopah Spring Member of the Paintbrush Tuff and the Tuffaceous Beds of the Calico Hills. The stratigraphy/lithology

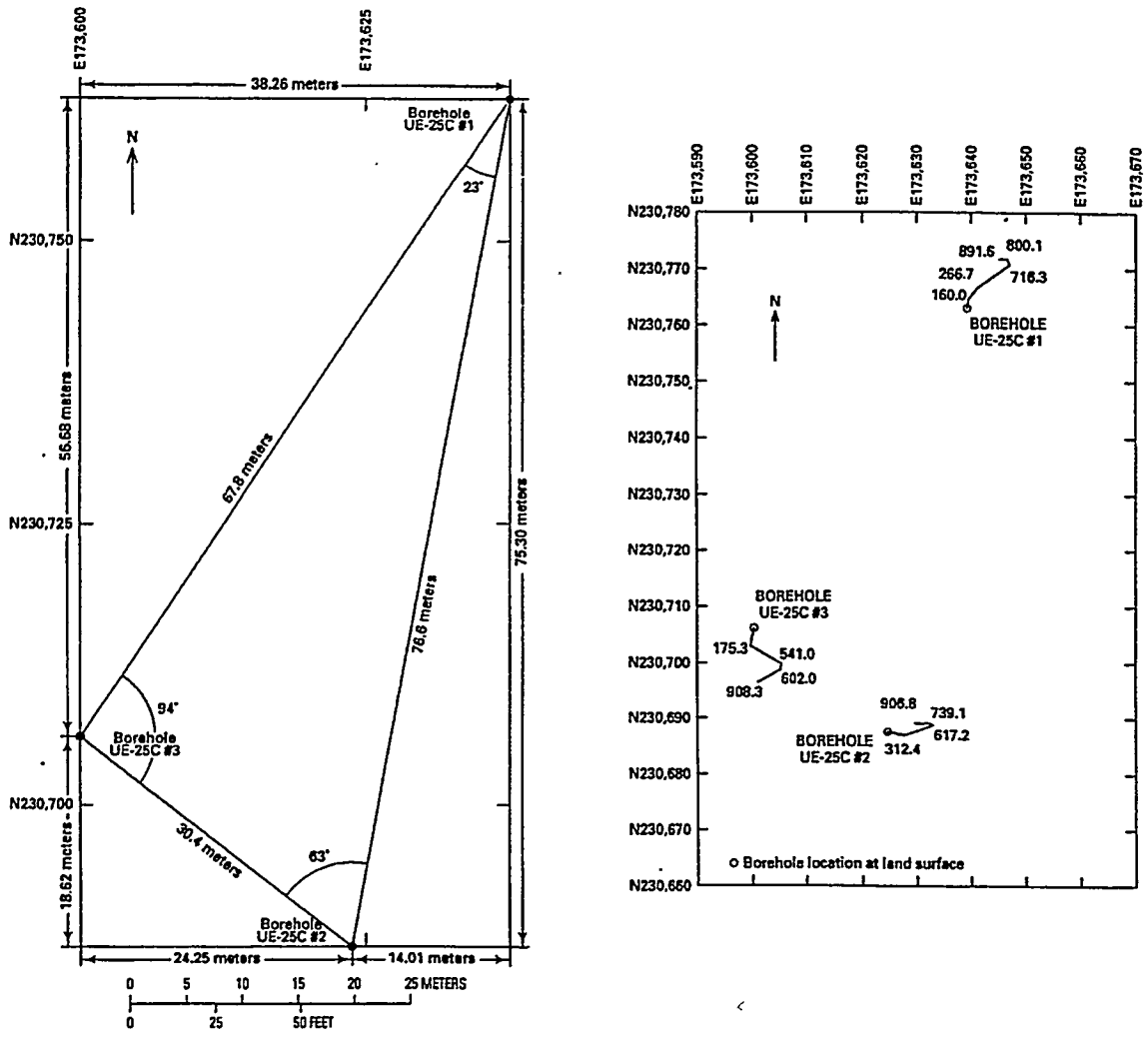

Fig. 1. Surface configuration of the C-Holes (left) and summary of vertical deviations at depth (right). Coordinates and depths are in meters. (From Geldon 1993.)

below the water table is shown in three dimensions in Fig. 3. A thorough description of the C-Holes and the geology and hydrology in their vicinity is provided by Geldon (1993 and in press).

Figures 4, 5, and 6 show the current best estimates of the matrix porosity, fracture density, and bulk hydraulic conductivity, respectively, as a function of depth below the water table in the C-Holes. Porosities were determined by the USGS using a combination of gamma-gamma logging and helium injection of core samples. Fracture densities were determined from videotape logs conducted in C#1. The bulk hydraulic conductivities shown in Fig. 6 were estimated by Geldon (in press) using available hydrologic data collected during aquifer testing and from various logs at the C-Holes since 1984. The spheres shown in Figs. 3-6 indicate the current locations of inflatable packers in each well. The lines shown emanating from the wells in Fig. 6 indicate where significant inflow occurred during pumping tests in the mid-1980s. The lengths of the lines are

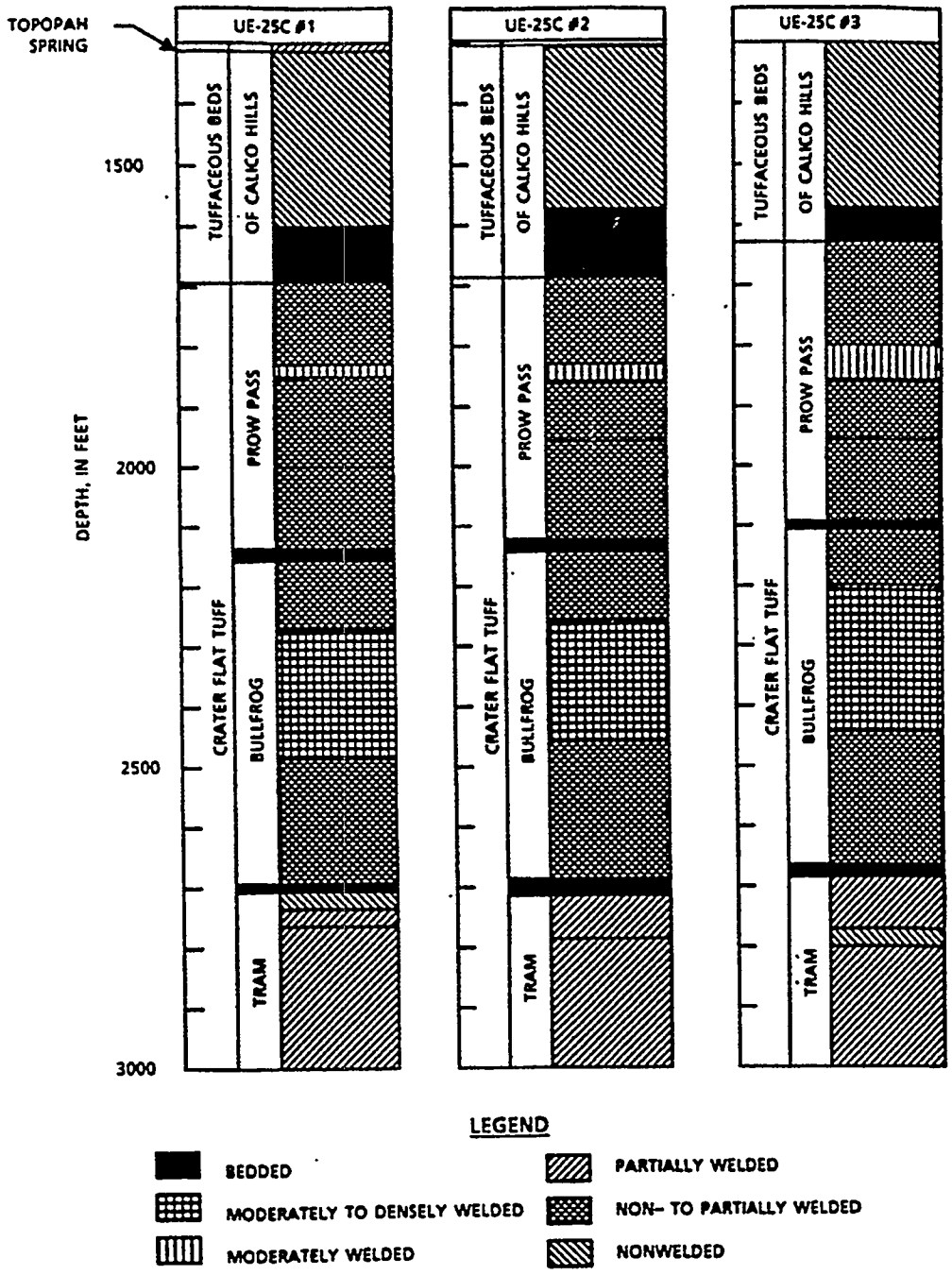

Fig. 2. Summary of stratigraphy and lithology in the C-Holes (below the water table). (From Office of Civilian Radioactive Waste Management, 1988)

proportional to the percentage of the total flow that occurred within each well (comparisons of flows in different wells are not valid). It should be noted that measured pore-scale permeabilities of core samples from the C-Holes suggest that bulk hydraulic conductivities exceed matrix hydraulic conductivities by over three orders of magnitude in each of the intervals in the C-Holes. Thus, flow in the saturated zone at the C-Holes is expected to be dominated by fractures (permeability in the matrix can be neglected as a first approximation).

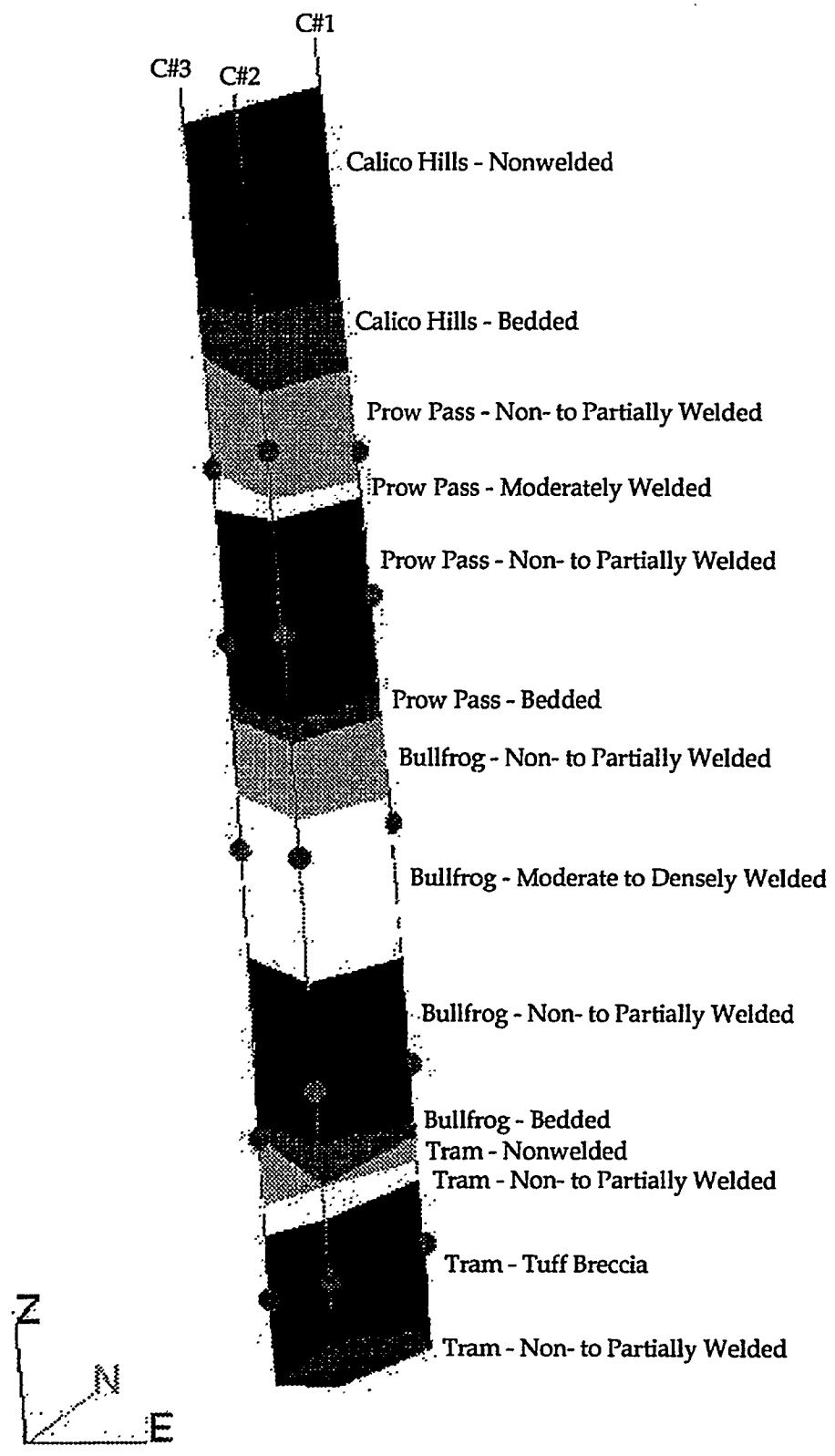

Fig. 3. 3-D representation of stratigraphy and lithology below the water table at the C-Holes. Spheres indicate current locations of inflatable packers. Data from Geldon (1993).

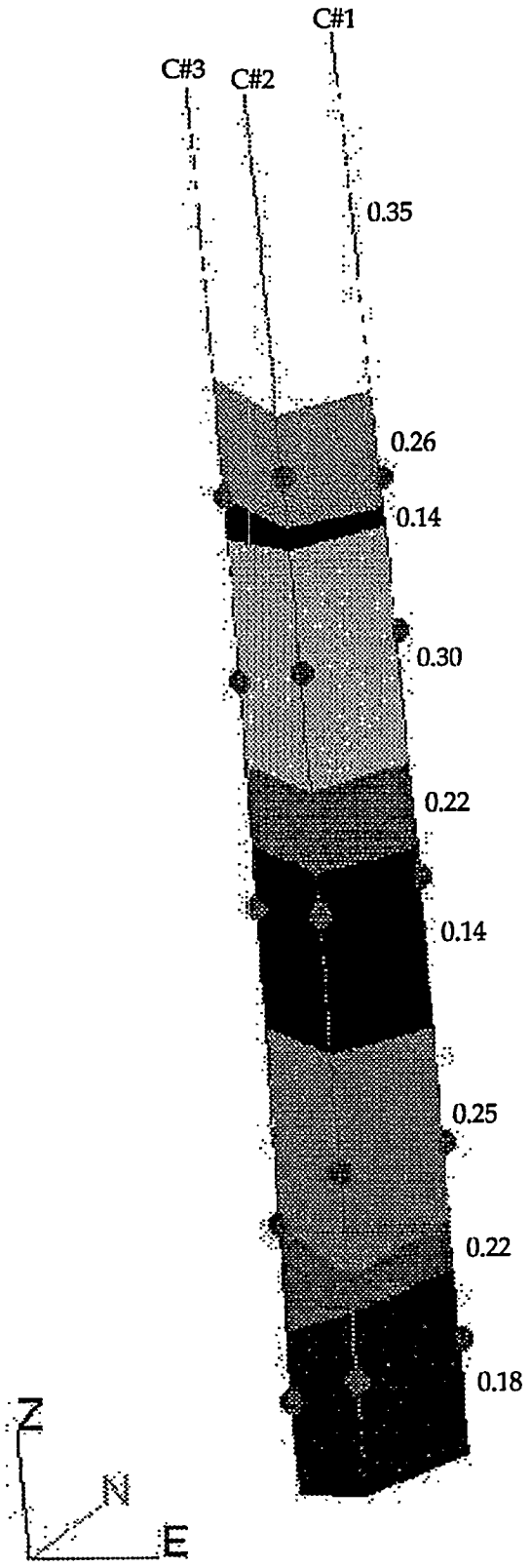

Fig. 4. 3-D representation of matrix porosity below the water table at the C-Holes (numbers indicate porosity). Spheres indicate current locations of inflatable packers. Data from Geldon (1993).

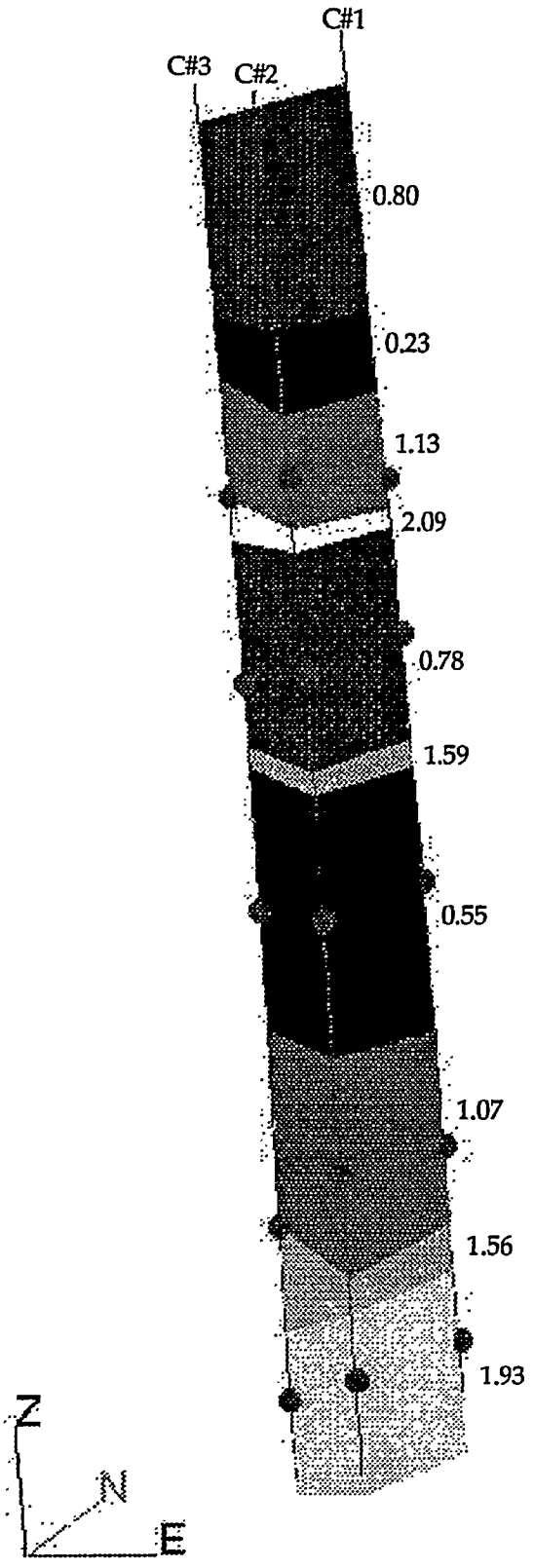

Fig. 5. 3-D representation of fracture densities below the water table at the C-Holes (numbers indicate fractures/m). Spheres indicate current locations of inflatable packers. Data from Geldon (1993).

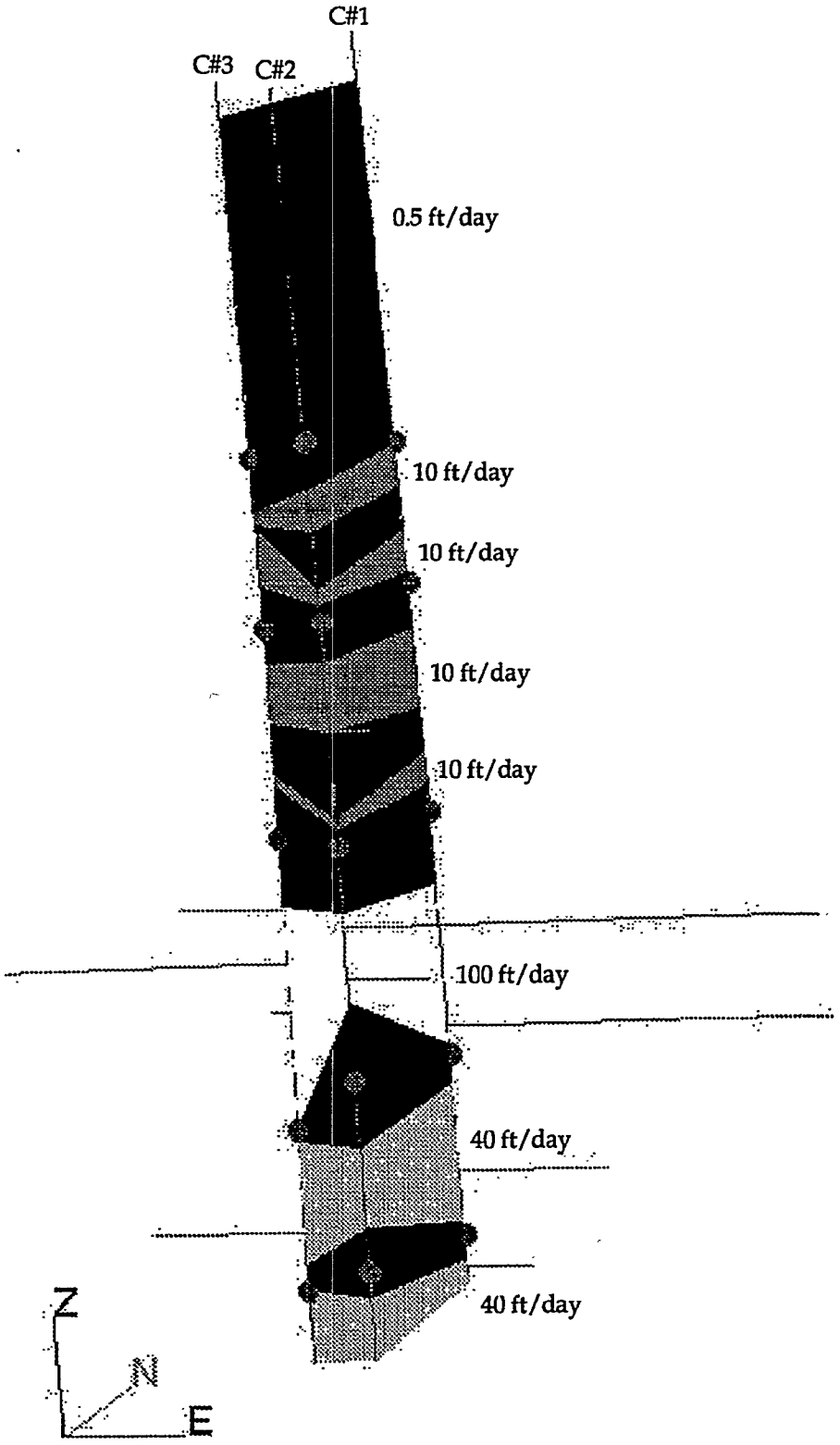

Fig 6. 3-D representation of hydraulic conductivities below the water table at the C-Holes. Black bands are nonconducting zones. Lengths of horizontal lines are proportional to inflow rates during pump tests in the mid-1980s. Spheres indicate current locations of inflatable packers. Data from Geldon (1993).

Geldon has identified 4 separate "aquifers" below the water table: the Calico Hills, Prow Pass-Upper Bullfrog, Bullfrog, and Tram aquifers — corresponding to the units in which they occur. Each of these aquifers has been assigned a different hydraulic conductivity by Geldon (see Fig. 6). The aquifers are separated from each other by low conductivity zones. As shown in Fig. 6, some of the aquifers also contain horizontal "bands" of low conductivity that separate more conductive intervals from each other within an aquifer.

As indicated by Figs. 3-6, inflatable packer strings containing five packers have been lowered into each of the C-Holes. The current packer locations were chosen by the USGS to allow isolation of the different "aquifers" and/or conductive intervals identified by Geldon. Each packer is located in a nonconductive zone in between two conductive zones. A submersible pump with variable speed control has been included in the packer string in C#3 (about 100 ft below the water table). This pump can be used to extract water from any isolated zone in C#3 at up to about 200 gallons per minute. C#3 will probably serve as the production well in all of the tracer tests conducted at the C-Holes because the composite transmissivity of this well is significantly larger than that of the other wells. This greater transmissivity will allow greater pumping rates to be maintained without drawing water down to the pump inlet. Pressure and temperature transducers have been installed between each pair of packers, above the top packer, and below the bottom packer in each hole.

By the time tracer tests are conducted, it should be possible to introduce tracers into any packed-off interval in C#1 or C#2 using a variety of injection methods. Tracers will be introduced through sliding sleeves located just below the packers in the 2-7/8" piping that makes up the packer strings. Tracer tests will be conducted in either radial convergent mode, where tracers are injected into C#1 or C#2 and then allowed to "converge" in the radial flow field to the pumped well (C#3), or in recirculating mode, where some or all of the produced water from C#3 is (re)injected into C#1 or C#2 behind the tracer solution. Options for injecting tracers in convergent tracer tests will include (1) forcing tracer solution out of the 1.66" injection tubing using compressed gas and a wiper plug to push the tracer solution through a cracking valve located near the open sliding sleeve, (2) forcing tracer solution out of the 1.66" tubing by chasing it with water pumped by a progressing cavity pump, or (3) pumping tracer solution directly into the 2-7/8" piping with one sliding sleeve open. The latter two options would allow the tracer solution to be "chased" into the borehole by any desired amount of water, thus helping to "push" tracers out of the dead volume in the borehole and into the formation. If tracer tests are conducted in partial or complete recirculating mode, tracer solution will either be "dumped" or metered into the recirculation loop at the surface. Details of the injection equipment and other downhole equipment are provided in Bureau of Reclamation 1993.

1.2 Tracer Testing Program

The tracer testing program at the C-Holes will involve the use of conservative solute tracers, reactive solute tracers, and microspheres. The objective of the program is to generate data for developing and testing conceptual models of flow and radionuclide transport over large scales in the fracture-dominated flow in the saturated zone, with emphasis on studying the mechanisms of solute matrix diffusion and sorption. These

phenomena could potentially increase radionuclide travel times by several orders of magnitude over groundwater travel times in fractures. The USGS is responsible for tracer tests involving conservative solutes, and Los Alamos is responsible for tests involving reactive solutes and microspheres. The rationale behind the tracer tests and the information that the tests will provide for the Yucca Mountain Site Characterization Project are discussed in detail in the Study Plans for conservative tracer testing (USGS 1990) and reactive tracer testing (LANL 1989). A summary of the pertinent information in these study plans is provided here.

Testing with conservative solute tracers (i.e., tracers that do not sorb or react in any way with the rock surfaces) is expected to yield information on water flow through the saturated zone. Because of their small (molecular) size and nonreactivity, these tracers should move through the groundwater system in the same manner as water molecules. However, because of diffusion, they will not necessarily remain in the mobile water in the fractures of the system. Instead, they will be free to diffuse out of the fractures and into the stagnant water in the pores of the tuff matrix, a process known as matrix diffusion. Because the fractures are very narrow (<1 mm), conservative solutes are expected to have ample opportunity to diffuse into the matrix during their transit through the saturated zone in the tracer tests. Also, because the matrix porosity at the C-Holes is much greater than the fracture porosity (~0.2 vs. ~0.001), the tracers could spend considerably more time in the matrix than in the fractures, thus significantly delaying their arrival at the production well and suppressing their recovery in the tests.

Reactive solute tracers will diffuse into the matrix and sorb to rock surfaces that they come in contact with, thus delaying their arrival and suppressing their recovery even more than conservative solutes. Reactive tracers will be used at the C-Holes to ascertain whether sorption parameters derived from laboratory batch sorption measurements and column transport tests can be used to predict transport in the field. In making such an assessment, it is always important to compare the breakthrough of the sorbing species to that of a conservative solute, as this is the only credible method of being able to differentiate between the effects of sorption and the effects of hydrodynamic dispersion and matrix diffusion in the system. It is assumed that the conservative and reactive solutes will move through the system in exactly the same manner except that the reactive solute will sorb while the conservative solute will not. Thus, differences between the observed transport behavior of the two tracers will be attributed solely to sorption of the reactive tracer.

Polystyrene microsphere tracers (size range 0.3 to 1.0 μm) offer a unique opportunity to accomplish two related objectives in a tracer test: (1) study the potential transport of colloidal contaminants through the saturated zone using an admittedly imperfect but nevertheless colloidal tracer, and (2) study transport through fractures in the saturated zone using a tracer that is too large to diffuse into the matrix. If they do not significantly settle or deposit onto fracture surfaces, microspheres should provide a measure of the travel time and dispersion associated with the mobile water in the fractures (without being influenced by the stagnant water in the matrix). This information would be invaluable in assessing the effects of matrix diffusion on solute tracers.

As stated earlier, the tracer tests will focus on investigating the processes of matrix diffusion and sorption because these processes offer the potential to increase the travel times of radionuclides within the saturated zone by several orders of magnitude over

what would be predicted by assuming that radionuclides travel only within fractures and do not sorb to mineral surfaces. The tracer testing program is expected to proceed roughly as follows:

- The USGS and its subcontractor, the University of Nevada Las Vegas (UNLV), will conduct radially convergent conservative tracer tests using a suite of fluorinated benzoic acids (FBAs) as tracers. The FBAs initially will be injected as a slug into a packed-off zone in C#1 or C#2 using the compressed gas/wiper plug injection method mentioned in Section 1.1. If poor recovery is achieved, the USGS/UNLV may consider one of the other injection methods described in Section 1.1. The FBAs will be analyzed using high-pressure liquid chromatography with a UV absorbance detector. The tracer tests probably will initially be conducted in the Bullfrog "aquifer" (between the 3rd and 4th packers from the surface) because this "aquifer" has the largest hydraulic conductivity in the C-Holes. However, a final decision on which intervals to inject tracer into and withdraw from will not be made until hydraulic responses from different intervals are determined during hydraulic pumping tests.
- Reactive tracer tests will be conducted only after a significant recovery of conservative tracer has been achieved. This prerequisite stems from the recognition that a significant recovery of conservative tracers is essential if any recovery of a reactive tracer is to be expected. Also, unsuccessful reactive tracer tests will jeopardize future reactive tracer testing because any sorbing tracer that remains in the formation after a test could potentially contaminate future tests. Ideally, the reactive tracer tests should be run under the same flow conditions (i.e., the same flow rates into and out of wells) as the conservative tracer tests to allow legitimate comparisons to be made between the tests. Lithium bromide will be used as tracer in all reactive tracer tests, with lithium ion serving as the sorbing solute and bromide ion serving as a conservative solute. Lithium will be analyzed by inductively-coupled plasma/atomic emission spectroscopy (ICP/AES), and bromide will be analyzed by ion chromatography (IC). Lithium sorption to C-Holes tuffs has been extensively characterized in laboratory experiments at Los Alamos. Lithium was chosen as a sorbing tracer because it sorbs weakly enough that a reasonable recovery can be expected in tracer tests (a more strongly sorbing tracer would never make it to the production well).
- Carboxylate-modified latex (CML) polystyrene microspheres will be used as tracers in select experiments to assess colloid transport and transport through fractures without diffusion into the tuff matrix. CML microspheres have been selected as colloid tracers because of their near-neutral buoyancy (specific gravity of 1.05), which will minimize settling, and because of their high negative surface charge density, which will minimize electrochemical attachment to rock surfaces. These microspheres have been shown in laboratory experiments at Los Alamos to transport through fractures with less attenuation than ordinary carboxylated polystyrene microspheres or silica microspheres (Reimus 1995). The CML microspheres will be tagged with fluorescent dyes and analyzed by flow cytometry (Steinkamp et al. 1991).

As the tracer testing program matures, partial and complete recirculation of the produced water from C#3 will be considered in tracer tests, and testing of intervals other

than the Bullfrog "aquifer" (or whichever aquifer is initially tested) will be pursued. The tracer transport predictions explore tradeoffs between different injection/production strategies as well as sensitivities of tracer transport to the following test/system parameters: (1) type of tracer (fracture flow only, nonsorbing solute, sorbing solute), (2) injection well (C#1 or C#2), (3) fracture porosity, (4) matrix porosity, (5) average fracture aperture, (6) sorption parameter (i.e., K_d), (7) solute diffusion coefficient, (8) formation dispersivity, and (9) whether the aquifer being tested can be considered confined or unconfined. The models used for tracer transport predictions are described in Section 2, and the results of the predictions are presented in Section 3. Recommendations for tracer testing are discussed in Section 4, and future modeling work is discussed in Section 5.

2.0 PARTICLE-TRACKING MODELS

Two- and three-dimensional particle-tracking models have been developed to simulate interwell tracer tests in fractured media. The models are not restricted to simulating tracer experiments at the C-Holes or in fractured media, but they have features developed specifically to simulate some of the unique aspects of the C-Holes tests. For instance, because of the large diameter of the C-Holes (10 inches), and the length of the packed-off intervals (as much as a few hundred feet), the dead volume of the injection zones will be so large (~1000 gal) that the rate at which tracer enters the formation could be significantly influenced by the injection strategy, especially if tracer injection is not followed by water chase or recirculation. This, in turn, could have a significant influence on the tracer breakthrough curves because much of the observed dispersion at the production well could be the result of slow injection of tracer into the groundwater system rather than true dispersion in the system. The models assume an exponential decay of tracer concentrations in the injection borehole (i.e., ideal mixing in the borehole) with a time constant equal to the borehole volume divided by the flow rate out of the borehole. This exponential decay is shown to be important when there is no water chase or recirculation because of the very low flow rates out of the borehole that occur under these conditions.

2.1 Principles of Particle-Tracking

Before describing the specific features of the models, the principles of particle-tracking calculations are briefly reviewed. Detailed discussions of particle tracking methods applied to contaminant transport problems are provided by Kinzelbach (1987), Tompson et al. (1987), and Tompson and Gelhar (1990). Particle-tracking calculations require the existence of a flow field solution before a transport problem can be solved. Assuming that a flow field solution exists, the following equation can be used to follow the progress of a solute particle through the flow field given a starting position (Tompson et al. 1987):

$$\mathbf{x}(t+\Delta t) = \mathbf{x}(t) + \mathbf{A}\cdot\Delta t + \mathbf{B}\cdot\mathbf{z}\sqrt{\Delta t} \qquad (1)$$

where, $\mathbf{x}(t)$ = particle position vector at time t,
Δt = time increment,
$\mathbf{A} = \mathbf{v} + \nabla \cdot \mathbf{D} + \mathbf{D}\,\nabla \ln \varepsilon$ ($\mathbf{A}$, $\mathbf{v}$, $\mathbf{D}$, and ε are functions of $\mathbf{x}$),
$\mathbf{v}$ = fluid velocity vector,
ε = porosity,
$\mathbf{D} = D_{ij} = (\alpha_T V + D)\delta_{ij} + (\alpha_L - \alpha_T)\, v_i v_j / V$ = symmetric dispesion tensor,
α_L = longitudinal dispersivity (tangent to velocity vector),
α_T = transverse dispersivity (normal to velocity vector),
δ_{ij} = kronecker delta (1 when $i = j$, 0 when $i \neq j$),
V = magnitude of velocity vector $\mathbf{v}$,
v_i, v_j = i and j components of velocity vector,
D = molecular diffusion coefficient,
$\mathbf{B}$ = diagonal tensor that satisfies $\mathbf{D}^* = 0.5\,\mathbf{B}\,\mathbf{B}^T$
$\mathbf{D}^*$ = diagonalized form of $\mathbf{D}$ (i.e., $\mathbf{D} = \mathbf{R}\,\mathbf{D}^*\,\mathbf{R}^T$), where $\mathbf{R}$ is defined in equation (3) below,
$\mathbf{R}$ = rotation matrix consisting of orthonormal eigenvectors of $\mathbf{D}$ (as columns - see equation 3), and
$\mathbf{z}$ = vector of random and independent components that are normally distributed with a mean of zero and a variance of 1.

The term in equation (1) accounts for all deterministic particle motions, including those due to fluid motion ($\mathbf{v}$), gradients in the dispersion coefficient ($\nabla \cdot \mathbf{D}$), and gradients in porosity ($\mathbf{D} \cdot \nabla \ln \varepsilon$). The terms containing $\mathbf{D}$ in $\mathbf{A}$ could be expressed in terms of $\mathbf{R}$ and $\mathbf{B}$, but that is not done here because these terms are assumed to be negligible in comparison to the fluid velocity term, $\mathbf{v}$. Dispersivity or porosity gradients are generally important only at boundaries between media or at saturation boundaries in unsaturated media, and neither of these situations is considered in this study. The last term in equation (1) accounts for stochastic particle motions resulting from the dispersion tensor.

With a dispersion tensor given by $D_{ij} = (\alpha_T V + D)\delta_{ij} + (\alpha_L - \alpha_T)\, v_i v_j / V$, it can be shown (Tompson et al. 1987) that $\mathbf{B}$ is given by

$$\mathbf{B} = \begin{bmatrix} \sqrt{2(\alpha_L V + D)} & 0 & 0 \\ 0 & \sqrt{2(\alpha_T V + D)} & 0 \\ 0 & 0 & \sqrt{2(\alpha_T V + D)} \end{bmatrix} \qquad (2)$$

The rotation matrix, $\mathbf{R}$, is not unique, but a convenient choice for computational purposes suggested by Tompson et al. (1987) is:

$$\mathbf{R} = \begin{bmatrix} \frac{v_1}{V} & \frac{-v_2}{\beta} & \frac{-\left(v_2^2 + v_3^2 + v_1 v_3\right)}{\beta V} \\ \frac{v_2}{V} & \frac{\left(v_1 + v_3\right)}{\beta} & \frac{\left[v_2\left(v_1 - v_3\right)\right]}{\beta V} \\ \frac{v_3}{V} & \frac{-v_2}{\beta} & \frac{\left(v_1^2 + v_2^2 + v_1 v_3\right)}{\beta V} \end{bmatrix} \qquad (3)$$

where, $\beta = \sqrt{V^2 + 2v_1 v_3 + v_2^2}$ for $V > 0$.

The first column of **R** is the normalized eigenvector of **D** in the direction of flow, and the other columns are vectors that are mutually orthogonal to this one. Note that **R** will be a function of location in the flow field.

To predict tracer transport behavior in a flow system, it is necessary to simulate the movement of a large number of particles through the system using equation 1. The number of particles should be large enough to allow a statistically meaningful estimate of particle residence time distribution(s) in the system. A frequency distribution of the particle residence times is mathematically analogous to a breakthrough curve provided that (1) the particles are introduced into the system in a representative manner at all inflow locations, and (2) all time delays not associated with transport through the groundwater flow system are properly accounted for. These issues are discussed in the next section.

2.2 Introduction of Particles into a Flow System and Time Delays not Associated with Groundwater Flow

The first step in properly introducing particles into a flow system in a particle-tracking model involves constructing a cumulative probability density function in which the incremental probabilities are proportional to flow rates into the system at the entry locations. For instance, if a flow system has three discrete entry locations with flow rates of 1, 2, and 3 (arbitrary units), the probability of entering the system at these locations will be 1/6, 1/3, and 1/2, respectively. In this case, a discrete cumulative probability density function with probability cutoffs at 1/6, 1/2, and 1 would be constructed. A uniformly distributed random number between 0 and 1 would then be generated using an appropriate algorithm, and the entrance location would be determined from the location that corresponds to the value of the random number. For instance, if 0.336 were selected as the random number in this example, the entry location would be the one with a flow rate of 2 because 0.336 falls between 1/6 and 1/2, which is the portion of the cumulative probability density function that corresponds to the entry location with a flow rate of 2. This technique is used in the interwell tracer transport

particle-tracking models to determine the location at which particles enter the groundwater flow system from the injection well.

Time delays that are not associated with groundwater flow but which must be considered in particle-tracking models include (1) travel times in pipes, (2) residence times in boreholes, and (3) delays associated with the finite duration of the injection pulse. These delays are handled in the interwell tracer transport particle-tracking models as follows:

(1) Pipe flow is assumed to be plug flow, and the delay time is therefore a simple deterministic time that is given by the volume of the pipe divided by the flow rate.
(2) Boreholes are assumed to be well mixed. The time that a particle spends in a borehole is determined by randomly sampling a uniform distribution between 0 and 1 and then using the following equation to calculate the residence time:

$$\Delta t = \left(\frac{V_B}{F}\right)\ln(u) \qquad (4)$$

where, Δt = time spent in borehole,
V_B = volume of packed-off interval in borehole,
F = flow rate out of packed-off interval in borehole, and
u = uniformly distributed random number in the interval [0,1].

Implementation of equation (4) results in exponentially distributed residence times with a mean of V_B/F, which is what is expected for a well-mixed volume. Note that F is the sum of the injection rate into the packed-off interval, the flow through the interval induced by pumping at the production well, and the flow through interval resulting from the ambient flow field.

(3) Delays associated with injection pulse duration are handled by randomly sampling a uniform distribution between 0 and 1 and then using the resulting number as the fraction of total pulse time at which the particle enters the borehole.

2.3 Flow Fields Used in Particle-Tracking Models

To simulate tracer transport in the groundwater system between an injection well and a production well using equation (1), a flow field must be defined between the two wells. Because there are essentially no data available that would support the use of directionally-dependent hydraulic conductivities or permeabilities to predict flow fields at the C-Holes (other than in the vertical direction), it is assumed for this study that the media at the C-Holes are homogeneous and isotropic. This is undoubtedly not a valid assumption, but any other assumption would be equally unlikely given the existing paucity of data. By assuming a homogeneous and isotropic media, it is possible to use potential theory to predict flow fields, thus obviating the need to do complex flow calculations. In potential theory, flow is assumed to emanate from or converge to a well in perfectly symmetrical fashion. Because the flow equations are linear, it is possible to determine the flow field resulting from two or more injection or production wells by

simply superimposing (that is, summing) the flow fields that result from each well. An ambient flow rate and flow direction (i.e., flow resulting from the natural gradient) can also be superimposed on the flows resulting from wells.

The 2-D and 3-D particle-tracking models correspond to a confined aquifer (where the wells are fully-penetrating) and an unconfined aquifer, respectively. In the 2-D model, flow from each well is considered to be radially convergent or divergent with no component in the vertical (z-) direction. The physical situation corresponding to this type of model is illustrated in Fig. 7. The natural coordinate system to use in the 2-D model is cylindrical coordinates (r,θ); where lines of equipotential from a single well are lines of constant radius (circles) and streamlines are lines of constant θ. The natural coordinate system to use in the 3-D model is a conjugate coordinate system of revolution known as prolate spheroidal coordinates, illustrated in Fig. 8 (Happel and Brenner 1965). In this coordinate system, surfaces of constant ξ correspond to equipotential surfaces and surfaces of constant η correspond to streamlines. The two different models (2-D and 3-D) should effectively bound the expected behavior at the C-Holes; the "aquifers" are probably neither completely confined nor completely unconfined.

The radial flow rate as a function of distance from a single well in the 2-D case is given by the equation

$$v(r) = \frac{Q}{2\pi b \gamma r} \tag{5}$$

where, $v(r)$ = velocity in radial direction, m/sec
Q = volumetric flow rate into (+) or out of (-) well, m^3/sec
b = length of injection/production interval (i.e., distance between packers), m, and
γ = effective fracture porosity.

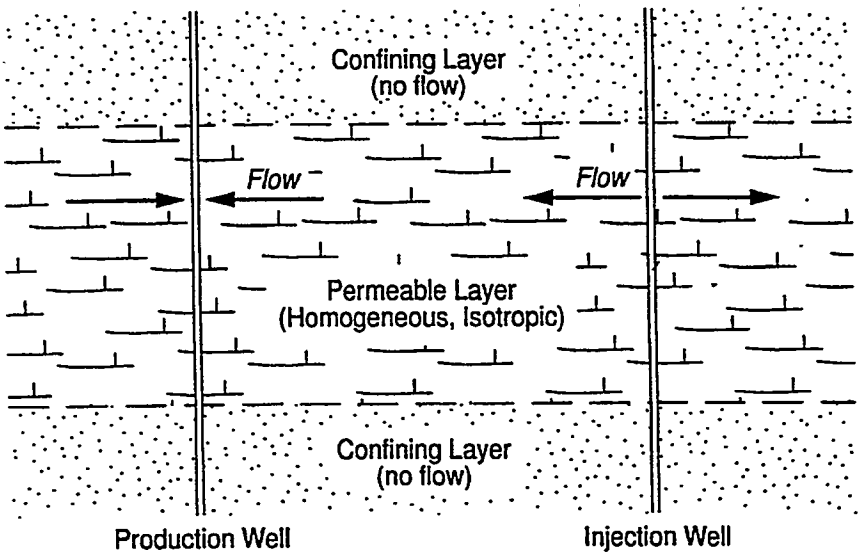

Fig. 7. Physical situation corresponding to 2-D particle-tracking model (completely confined aquifer).

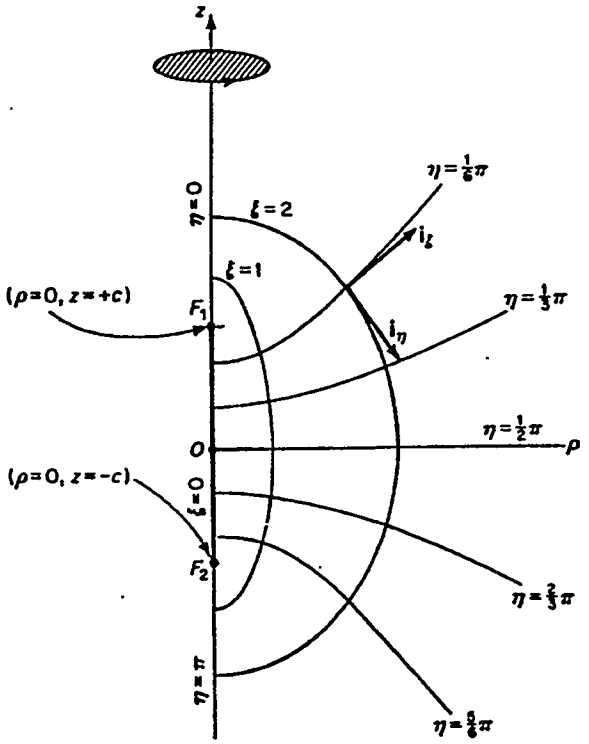

Fig. 8. Prolate spheroidal coordinate system used to describe 3-D flow through a homogeneous, isotropic medium (from Happel and Brenner 1965).

The situation in 3-D is considerably more complicated and is covered in Appendix A, which also includes a general discussion of the mathematical relationships between prolate spheroidal coordinates and cartesian coordinates and between velocity components in each coordinate system.

The key to describing a composite flow field that is a linear combination of flow from two wells is to relate the velocity vectors in the natural coordinate system of each well to velocity components in a common coordinate system. It is convenient to use cartesian coordinates as the common coordinate system. For two wells that are separated by a distance X (with x-y coordinates (0,0) and (X,0), respectively) and with flow rates - Q_1 and Q_2, respectively, it can be shown that the x- and y- velocity components at any arbitrary point (x,y) in 2-D space are given by

$$v_x = \frac{-Q_1}{2\pi b\gamma\sqrt{\left(x^2+y^2\right)}}\cos\left[\mathrm{Tan}^{-1}\left(\frac{y}{x}\right)\right] + \frac{Q_2}{2\pi b\gamma\sqrt{\left((x-X)^2+y^2\right)}}\cos\left[\mathrm{Tan}^{-1}\left(\frac{y}{(x-X)}\right)\right] \quad (6a)$$

$$v_y = \frac{-Q_1}{2\pi b\gamma\sqrt{\left(x^2+y^2\right)}}\sin\left[\mathrm{Tan}^{-1}\left(\frac{y}{x}\right)\right] + \frac{Q_2}{2\pi b\gamma\sqrt{\left((x-X)^2+y^2\right)}}\sin\left[\mathrm{Tan}^{-1}\left(\frac{y}{(x-X)}\right)\right] \quad (6b)$$

Equations (6) can be seen by inspection to be equivalent to

$$v_x = v_1(r_1)\cos\alpha + v_2(r_2)\cos\beta \tag{7a}$$

$$v_y = v_1(r_1)\sin\alpha + v_2(r_2)\sin\beta \tag{7b}$$

where, $v_1(r_1)$ = radial velocity resulting from well 1 in cylindrical coordinate system centered at well $1(r_1,\alpha)$,
$v_2(r_2)$ = radial velocity resulting from well 2 in cylindrical coordinate system centered at well $2(r_2,\beta)$,
α = angle formed by line connecting (x,y), well 1, and the axis between wells, and
β = angle formed by line connecting (x,y), well 2, and the axis between wells.

Equations (6) and (7) assume no ambient flow. The analogous development in 3-D is given in Appendix A.

It is well known (Freeze and Cherry 1979, Drost 1968) that boreholes perturb otherwise uniform flow fields such that flow streamlines are distorted into the borehole and the effective flow rate is greater through the hole than the surrounding formation (see Fig. 9). This phenomenon occurs as a result of the much lower flow resistance offered by the borehole than the surrounding formation. In the limit of an infinitely greater flow resistance in the formation than in the borehole, the flow through the borehole will be twice what it would be through a similar cross-section in an unperturbed flow field. This phenomenon is important when tracers are injected into a well

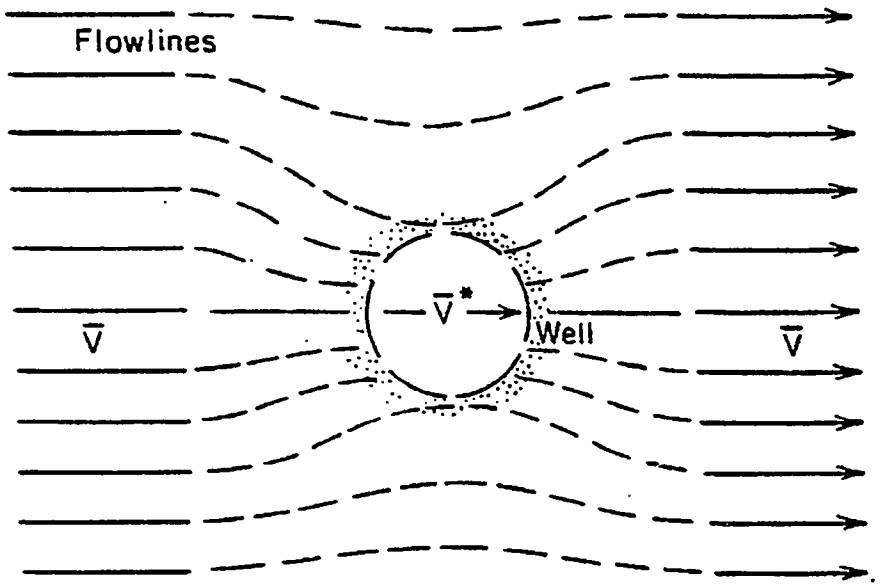

Fig. 9. Distortion of flow streamlines in the vicinity of a borehole (from Freeze and Cherry 1979).

without water chase or recirculation because under these conditions tracers can enter the formation only as a result of the induced flow from the production well, and this flow could vary by a factor of two depending on the relative flow resistances assumed for the formation and the borehole. Flow field distortion near an injection well is explicitly accounted for in the particle-tracking models. Derivations of the appropriate equations in 2-D are given in Appendix B. These same equations are used to perturb flow in the x- and y-directions in 3-D flow. Although this is not strictly correct (because perturbations should also occur in the z-direction) it is considered an adequate approximation because the z-component of flow near the injection well should be relatively small compared to the x- and y- components (with exceptions near the ends of the well).

2.4 Particle Trajectories Between Wells

The particles in the particle-tracking models follow specific trajectories from the injection well to the production well depending on where they enter the groundwater system from the injection well. Model-generated particle trajectories corresponding to different recirculation ratios in both 2-D and 3-D are shown in Figs. 10-16. Figure 13 shows 2-D trajectories near an injection well in the case of no recirculation and assuming a negligible borehole flow resistance relative to formation flow resistance. This figure illustrates that the particle-tracking model properly accounts for flow field distortion around a borehole. Examination of particle trajectory plots such as those of Figs. 10-16 has proven invaluable in verifying that the models are working properly.

Because nearly all the particle trajectories have outward curvature between the two wells, numerical errors almost always tend to increase particle travel distances and travel times relative to true distances and times. For this reason, it is important to minimize numerical errors when updating the positions of particles as they are "stepped" through the flow domain. The following model features are implemented to help minimize numerical errors:

(1) A 4th-order Runge-Kutta algorithm is used to update particle positions at each time step rather than a much simpler and more computationally efficient Euler algorithm. It was found that the computational penalty associated with using the Runge-Kutta algorithm was offset by the increased accuracy of the algorithm. If an Euler algorithm is used, particles tend to "fan out" more than they should, resulting in longer trajectories and longer travel times.

(2) Time and distance steps are kept very small near the wells, particularly near the injection well. Errors in travel distances and travel times are especially sensitive to numerical errors that occur close to the injection well because a small error in position near the well can result in the erroneous placement of a particle on a trajectory that has a much longer length than the correct trajectory. Time and distance increments are forced to be proportional to the distance from the nearest well. However, upper limits on the increments are imposed when particles are large distances from the wells.

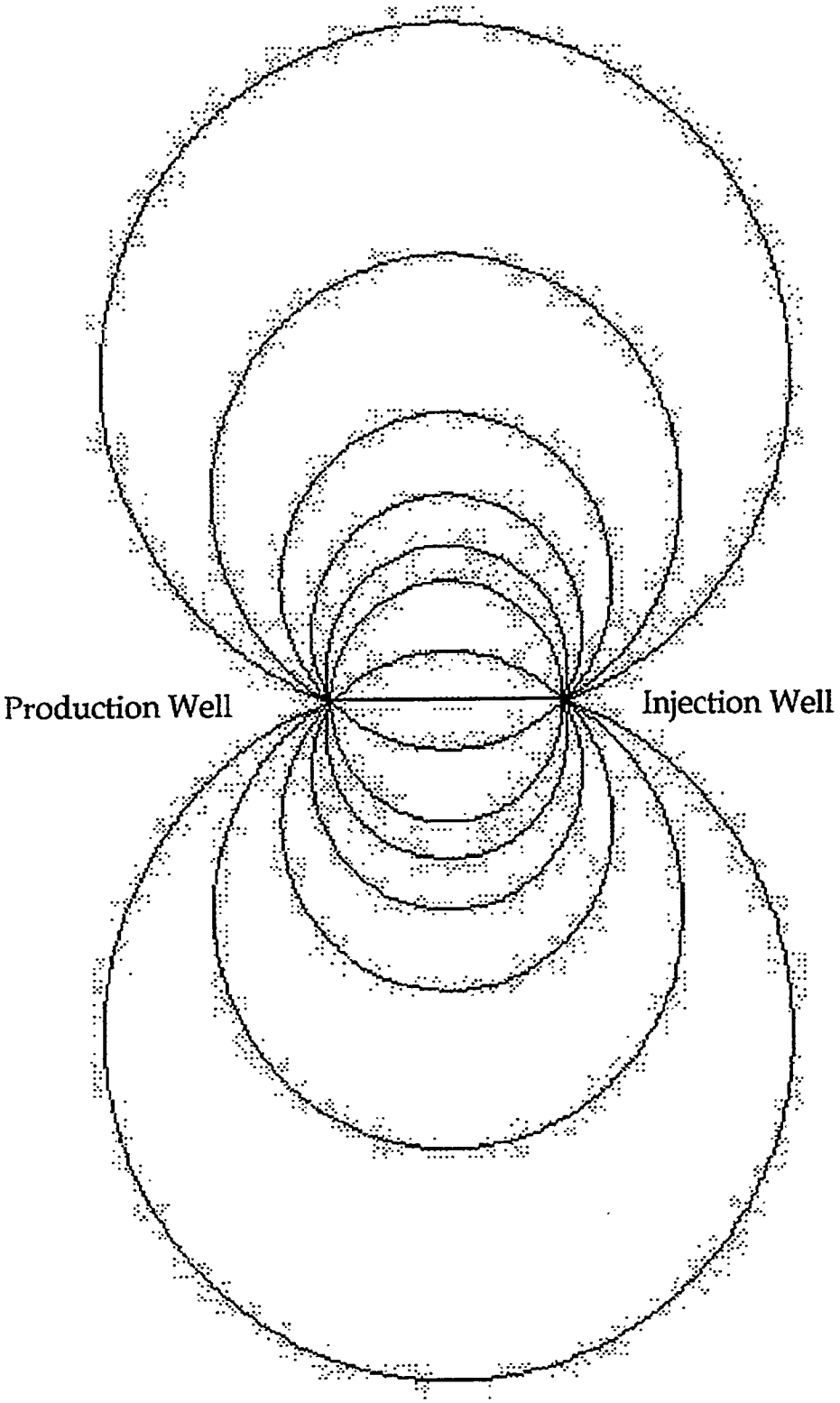

Fig. 10. Interwell particle trajectories in 2-D at 100% recirculation (trajectories are in x-y plane).

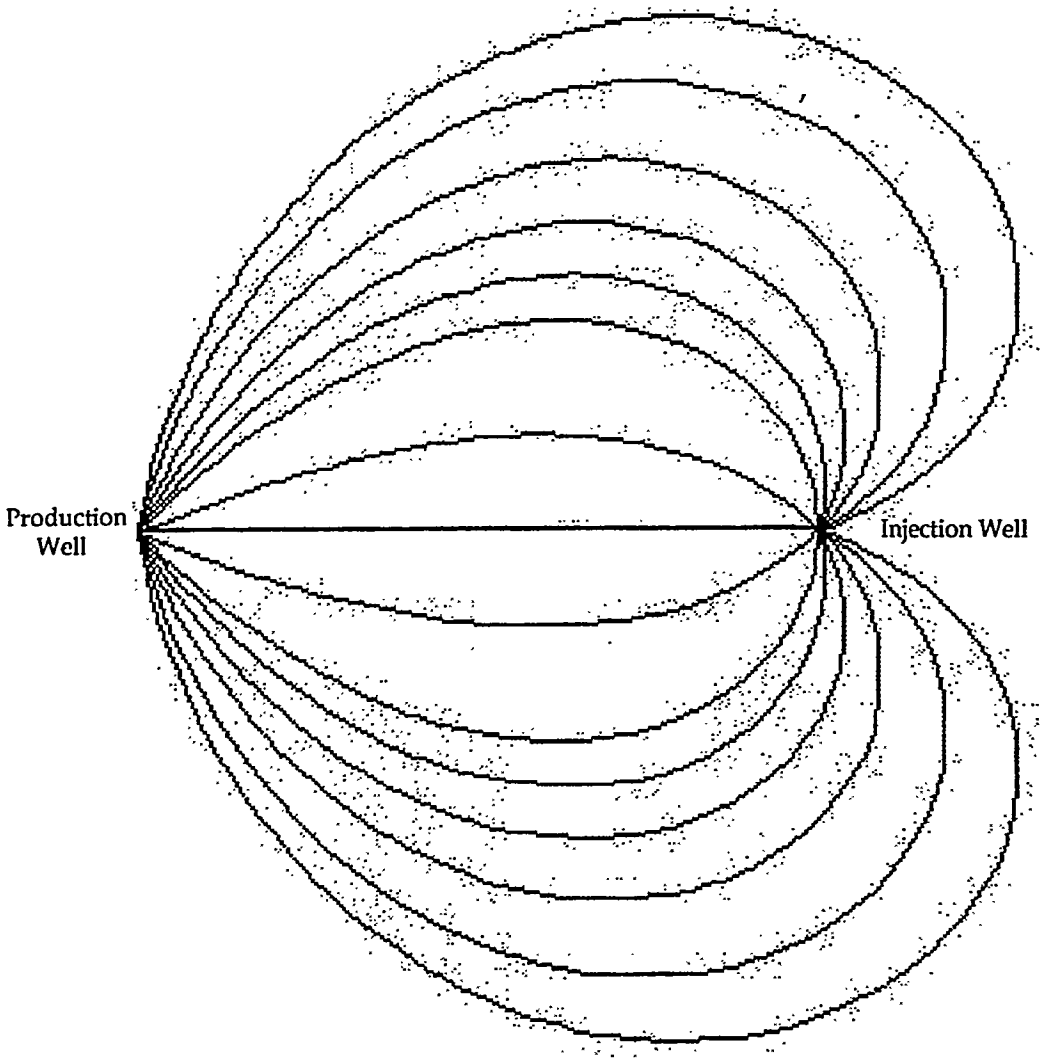

Fig. 11. Interwell particle trajectories in 2-D at 50% recirculation (trajectories are in x-y plane).

2.5 Simulation of Different Types of Tracer Particles

The transport of three different types of particles are simultaneously simulated whenever the 2-D or 3-D particle-tracking models are exercised. These particles correspond to (1) a species that remains only in the fractures of the flow system, (2) a species that can diffuse out of the fractures and into the rock matrix but does not sorb to the matrix, and (3) a species that diffuses into the rock matrix and sorbs to the matrix according to a reversible, linear adsorption isotherm. In the context of the planned reactive tracer tests at the C-Holes, these species are intended to correspond to (1) polystyrene microspheres, (2) bromide ion, and (3) lithium ion, respectively. All three types of particles follow the same streamlines through the system (that is, trajectories are not independently calculated for each type of particle), but the latter two particles experience additional time delays as they move through the system to account for time spent in the matrix either as a result of matrix diffusion or as a result of matrix diffusion

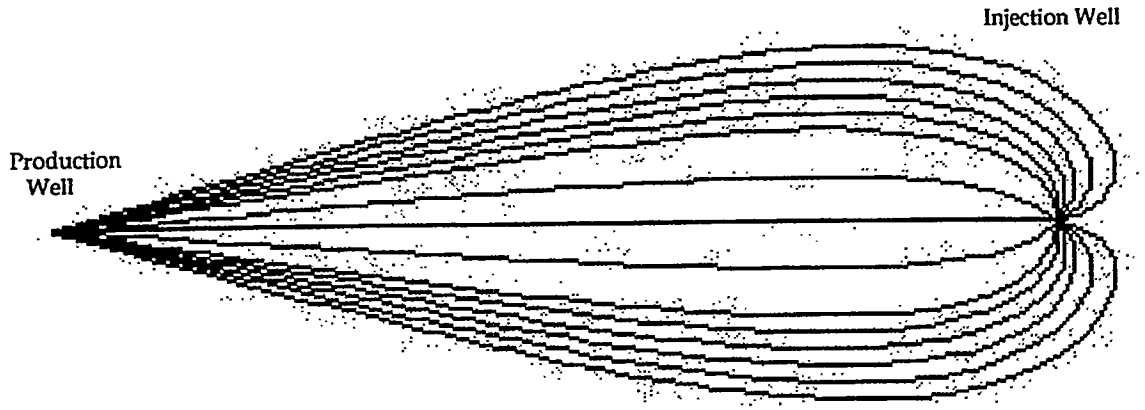

Fig. 12. Interwell particle trajectories in 2-D at 10% recirculation (trajectories are in x-y plane).

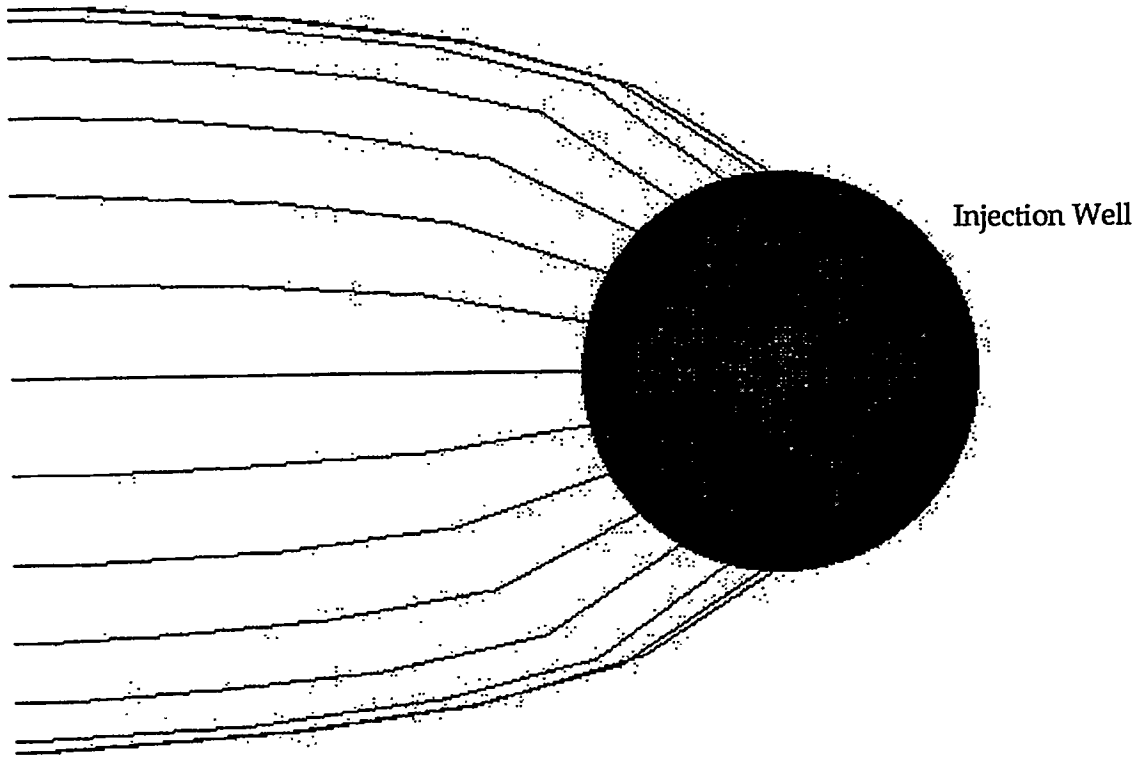

Fig. 13. 2-D interwell particle trajectories near an injection borehole with no recirculation. Trajectories show effects of flow field distortion caused by the borehole. Trajectories are in x-y plane.

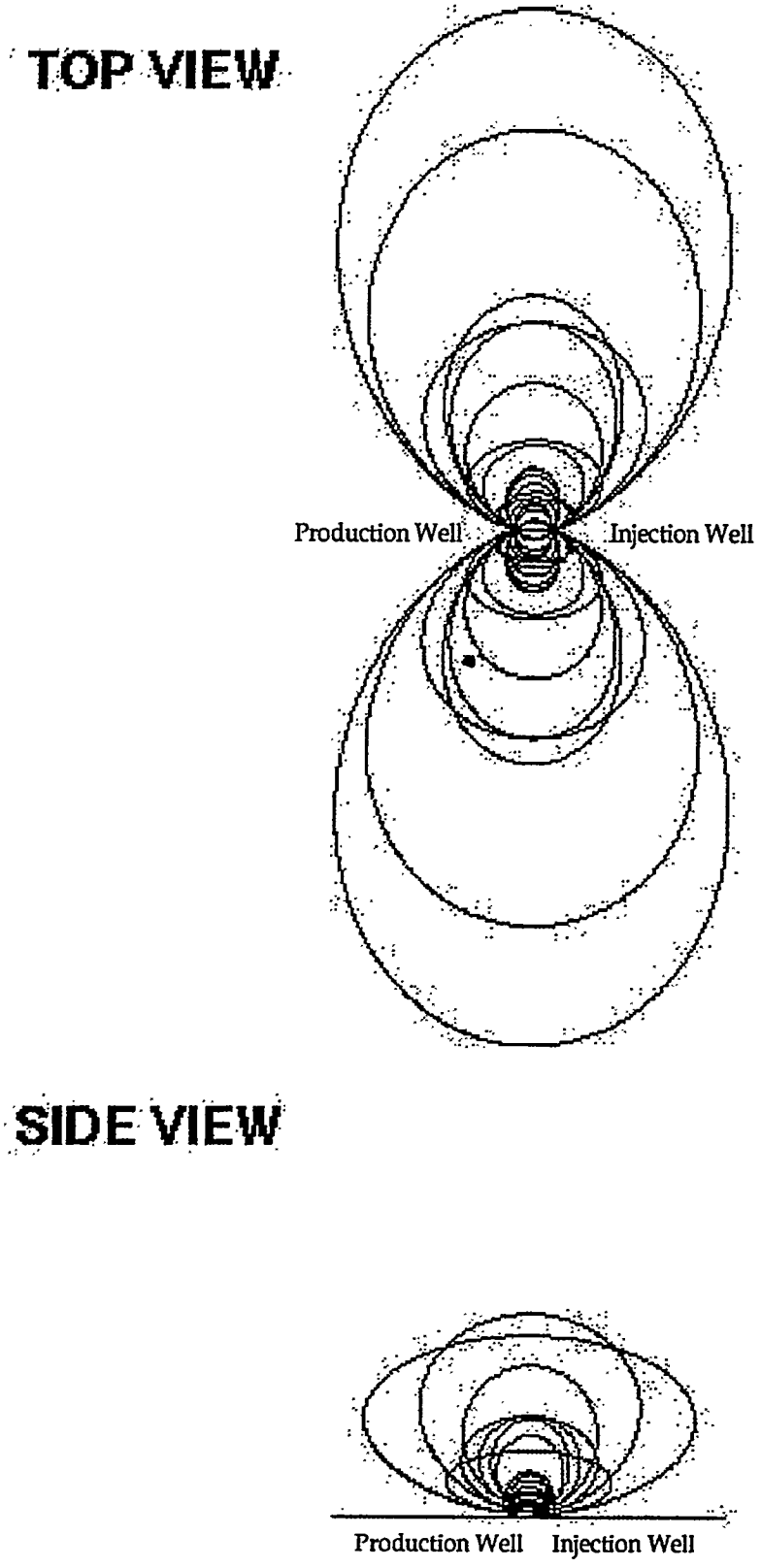

Fig. 14. Interwell particle trajectories in 3-D at 100% recirculation. Packed-off intervals have the same z centerline. Only trajectories at or above the centerline are shown. Particle trajectories below the centerline are symmetrical to those above centerline.

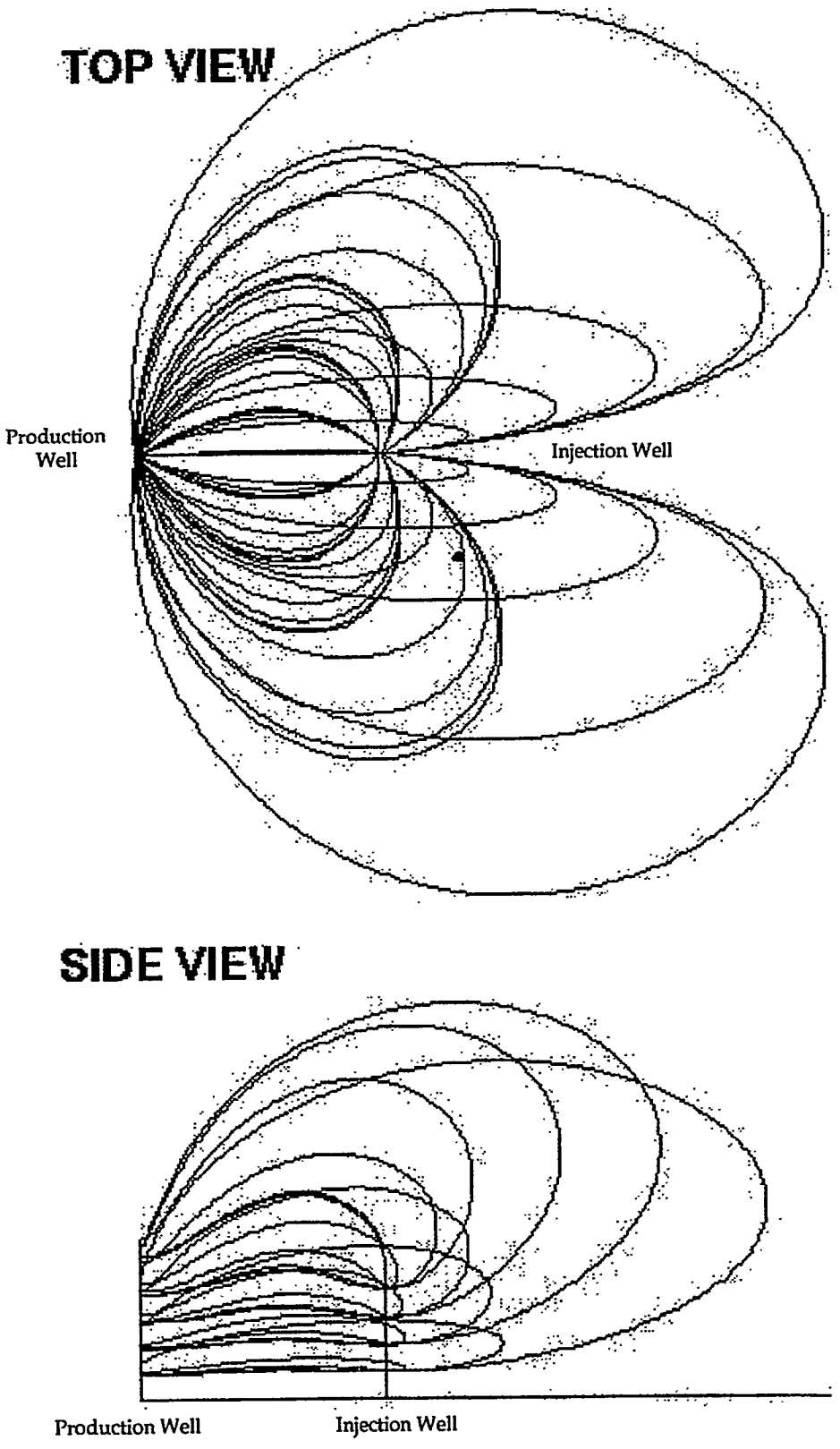

Fig. 15. Interwell particle trajectories in 3-D at 50% recirculation. Packed-off intervals have the same z centerline. Only trajectories at or above the centerline are shown. Particle trajectories below the centerline are symmetrical to those above centerline.

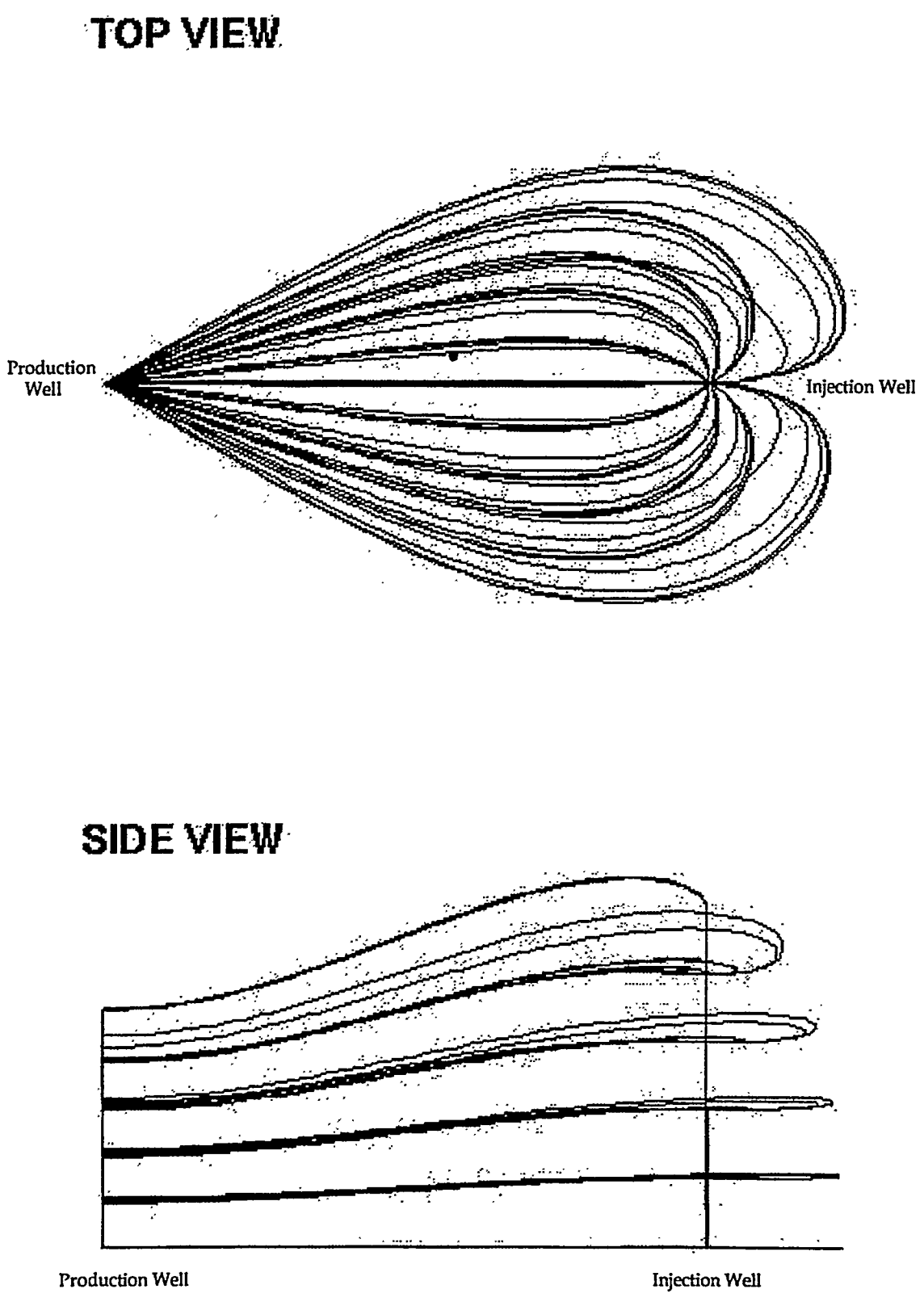

Fig. 16. Interwell particle trajectories in 3-D at 10% recirculation. Packed-off intervals have the same z centerline. Only trajectories at or above the centerline are shown. Particle trajectories below the centerline are symmetrical to those above centerline.

plus sorption to the matrix. Sorption to fracture walls is not explicitly accounted for, although this should not be a serious limitation because the majority of the surface area available for sorption will be in the matrix at the C-Holes. The travel time increments associated with the latter two types of particles are given by the following equation, which is a rearrangement of an analytical solution for fracture transport attributable to Starr et al. (1985):

$$\Delta t = \Delta t_o + \frac{\Delta t_o^2 \varepsilon^2 \tau D R}{a^2 [\text{Inverfc}(U(0,1))]} \tag{8}$$

where, Δ = particle time increment,
Δt_o = time increment of particle that does not diffuse into matrix,
ε = matrix porosity,
τ = matrix tortuosity,
D = free diffusion coefficient of species represented by particle,
R = retardation coefficient to account for sorption,
a = fracture aperture,
Inverfc(x) = the inverse of the complementary error function, and
U(0,1) = uniformly distributed random number between 0 and 1.

When equation (8) is used to calculate the time delay of a nonsorbing species, the retardation coefficient, R, is set equal to 1. The retardation coefficient is related to system parameters and measurable sorption parameters using the following well known formula (Freeze and Cherry 1979):

$$R = 1 + \frac{\rho_B K_d}{\varepsilon} \tag{9}$$

where, K_d = linear distribution coefficient, ml H_20/g solid
ρ_B = bulk density of solid, g/cm^3.

The approach of using equation (8) to delay particle times for matrix diffusion and sorption has been used by others to simulate solute transport through fractured media (Moreno and Neretnieks 1993). However, the analytical solution developed by Starr et al. must be used with caution because it is based on certain assumptions that may not necessarily be valid in a forced gradient system. The Starr solution assumes that (1) the fractures are parallel-plate channels, (2) there is no dispersion in the direction of flow (i.e., plug flow), (3) there is no concentration gradient in the fractures in the direction perpendicular to flow (i.e., there is sufficient time for the species to diffuse across the channels and flatten out any concentration profiles), (4) fractures are parallel to each other and are far enough apart that the solute diffusing into the matrix does not encounter solute from adjacent fractures (this allows the matrix to be modeled as a semi-infinite medium), and (5) diffusion into the matrix occurs only in the direction perpendicular to the fractures. It can be shown (Reimus, 1995) that assumptions (4) and (5) are satisfactory when considering tracer transport in forced-gradient experiments because the time

scales in such experiments are short enough that the distance of diffusion into the matrix is very short, and the concentration gradient in the matrix is essentially perpendicular to the fractures. Also, when evaluating tracer transport, predictions are not terribly sensitive to assumption (1) provided that the aperture of the parallel plates is a good approximation of the average volumetric aperture experienced by the tracers in the system. Assumption (2) is not really important because dispersion in the flow direction can be accounted for in the particle-tracking models using equation (1); it will be reflected as a distribution of times, Δt_o, (in equation 8) associated with traveling specified distance increments.

Assumption (3), therefore, is the only assumption that could cause significant problems when using the Starr solution in the particle-tracking models. The problem is that when the average fluid residence time in a fracture is short relative to the time it takes the species to diffuse across the width of the fracture, significant concentration profiles perpendicular to flow can be expected (with lower concentrations near the fracture walls), and equation (8) will effectively overpredict diffusion into the matrix. In the limit of a very short fluid residence time in the fracture, the tracer will not even sense the matrix, and it will move through the fracture as if the fracture walls are nonporous. A useful dimensionless parameter to assess the relative significance of diffusion across fractures is

$$N_{DL} = \frac{\sqrt{D \cdot \Delta t_o}}{a} \qquad (10)$$

where, N_{DL} = dimensionless parameter,
D = free diffusion coefficient, and
Δt_o = fluid residence time in fracture (same as in equation 8).

This parameter is essentially the ratio of the characteristic distance that a species diffuses during the time it spends in the fracture to the fracture aperture, a. It has been shown (Reimus, 1995), that when $N_{DL} > 1.5$, the Starr solution is essentially indistinguishable from the predictions obtained using a finite-difference model that fully accounts for concentration profiles perpendicular to flow in a parallel-plate channel. The Starr solution continues to yield reasonable approximations to the finite-difference solution until N_{DL} values are less than 1. Because of the computational burden associated with approximating matrix diffusion when the Starr solution is not strictly valid, it was decided to simply define a cutoff value of N_{DL} above which the Starr solution would be assumed valid and below which matrix diffusion would be completely ignored. For the simulations conducted for this report, the cutoff value in the particle-tracking models was set to $N_{DL} = 0.7$. Most of the particle-tracking calculations were found to be relatively insensitive to this cutoff value because the vast majority of the time that particles spend in the flow system is accumulated during time increments where N_{DL} is greater than 1.5.

Actual calculation of breakthrough curves is accomplished by compiling a frequency distribution, or histogram, of the number of different types of particles arriving at the

production wellhead as a function of time. The particles are "binned" into a user-specified number of bins starting at the first arrival time and ending at some user-specified cutoff time.

2.6 Accounting for Tracer Recirculation in Breakthrough Curves

A complication that occurs in partially- or fully-recirculating tracer tests is the reintroduction of any produced tracer into the groundwater system and its subsequent reappearance at the production well. When significant tracer recoveries are obtained in recirculating tests, it is common to observe multiple peaks in breakthrough curve(s). These peaks correspond to reinjections of a portion of the tracer mass that was originally injected. This phenomenon adds complexity to the interpretation of a tracer test because one is generally more interested in the "once-through" breakthrough curve that would result from an instantaneous injection of tracer and no recirculation (i.e., the true residence time distribution) than in the convoluted breakthrough curve resulting from the continuous reinjection of produced tracer. Obtaining a "once-through" breakthrough curve from a recirculating curve is a classic exercise in deconvolution. The starting point for this exercise is the convolution integral (Levenspiel 1972, Robinson and Tester 1984):

$$C_{out}(t) = \left(\frac{Q_{in}}{Q_{out}}\right) \int_0^t C_{in}(t-\tau)\, E(\tau)\, d\tau \qquad (11)$$

where, $E(t)$ = true residence time distribution ("once-through" breakthrough curve),
$C_{in}(t)$ = concentration of tracer injected into system at time t,
$C_{out}(t)$ = concentration of tracer produced at time t,
Q_{in} = flow rate into injection well (assumed constant for all t), and
Q_{out} = flow rate out of production well (assumed constant for all t).

The flow rate ratio in equation (11) accounts for tracer dilution when the injection flow rate is less than the production flow rate. Normally, one obtains $C_{out}(t)$ from the uncorrected breakthrough curve in a tracer test, and $C_{in}(t)$ is determined from the known injection pulse (at early times) plus $C_{out}(t)$ (at later times, after tracer appears at the production well). E(t) is then obtained (deconvolved) by solving equation (11), generally by numerical integration.

Our concern in this study is not to obtain E(t) from tracer data, but rather to predict $C_{out}(t)$ given a predicted E(t) and an injection pulse, $C_{in}(t)$. When a tracer test with continuous recirculation is simulated, the particle-tracking models always calculate a "once-through" breakthrough curve, E(t), assuming a dirac-delta function input of tracer and using the user-specified recirculation flow rate. Another "once-through" breakthrough curve is calculated for the initial tracer pulse injected into the system (this pulse will not be instantaneous and may be injected and chased at a different flow rate than the recirculation rate). The tracer concentrations at the production well resulting from

the initial pulse are then taken to be the values of $C_{in}(t)$, whereupon equation (11) is used to "conolve" $C_{in}(t)$ with the previously calculated E(t) to obtain $C_{out}(t)$, the breakthrough curve that includes the effects of recirculation. Note that because $C_{in}(t) = C_{out}(t)$ for all t > injection pulse time, and because $C_{out}(t)$ depends on all $C_{in}(\tau<t)$, it is necessary to continually update values of $C_{in}(t)$ before calculating any future $C_{out}(t)$'s. Whenever there is recirculation, the particle-tracking models always calculate a breakthrough curve without the effects of recirculation and one with the effects of recirculation. These can then be compared to determine the incremental effect of including recirculated tracer in the breakthrough curves.

2.7 User Options in Exercising the Particle-Tracking Models

The user has several options (user-specified inputs) when exercising the particle-tracking models. These are listed below.

- Distance between wells, meters.
- Length of packed-off intervals (only one length is specified for the 2-D model [both wells are assumed to have the same interval length]; two lengths are specified for the 3-D model, one for each well), meters.
- Radii of wells and radii of internal pipes (to allow calculation of cross-sectional area of the injection interval and of the pipes), meters.
- Distance from surface to injection/withdrawal points (to allow calculation of delay times in pipes), meters.
- Time delays in surface piping, sec.
- Injection, chase, and recirculation flow rates (gpm) , and duration times for the injection and chase periods (the chase and recirculation flow rates can be set to zero), sec.
- Velocity (m/sec) and direction (angle from axis between wells) of ambient groundwater flow (flow is assumed to be horizontal in 3-D model [no component in z-direction]).
- Relative permeabilities of boreholes and formation (to allow calculation of flow field distortion around injection borehole). Note: The flow field distortion calculations can be turned off by setting a flag; this is equivalent to setting the permeabilities equal to each other, but it allows faster computation times.
- Fracture porosity.
- Matrix porosity.
- Average fracture aperture, cm.
- Free diffusion coefficient of solutes (at the present time, only one value is specified for all species), /sec.
- Matrix tortuosity (multiplied by free diffusion coefficient to obtain diffusion coefficient in matrix).
- Retardation coefficient for sorbing solute.
- Peclet numbers tangent to flow and normal to flow. These are used to calculate the dispersivities α_L and α_T (see the definition of the dispersion tensor in Section 2.1) as follows:

$$\alpha_L = \frac{L}{N_{Pe(t)}} \tag{12a}$$

$$\alpha_T = \frac{L}{N_{Pe(n)}} \tag{12b}$$

where, L = distance between wells,
$N_{Pe(t)}$ = Peclet number tangent to flow, and
$N_{Pe(n)}$ = Peclet number normal to flow.

Note 1: When the Peclet numbers are set to zero, the dispersion tensor is set to zero (i.e., dispersion is "turned off"). Otherwise, larger Peclet numbers result in less dispersion.

Note 2: Dispersion is automatically "turned off" very close to the wells to avoid numerical errors that cause particles to "disperse" back into wells as they are leaving or to "disperse" to the opposite sides of wells, which is considered unrealistic.

This list of user-specified inputs is not all inclusive, but it contains all of the significant options that the user has control over.

2.8 Advantages and Limitations of the Particle-Tracking Models

The particle-tracking models were developed primarily because of the flexibility they offer in simulating different tracer injection schemes and different operational scenarios. Because of the inherent simplicity of particle-tracking models, this flexibility comes with minimal development and computational costs. Particle-tracking models also consume very little computer memory compared to typical finite-element or finite-difference codes, a feature which is attractive if one wishes to exercise models in the field on laptop computers that have memory restrictions.

The particle-tracking models developed for this study have some limitations that should be considered in future developments/enhancements of these or other models to predict and interpret tracer tests at the C-Holes. These limitations are listed below.

- Probably the most significant limitation is the assumption of a homogeneous, isotropic medium (other than the vertical confinement assumed when exercising the 2-D model). This assumption is inherent when using the flow fields described in Section 2.3, and it can only be relaxed by exercising an alternative model that is capable of calculating flow fields with a nonisotropic and/or spatially-dependent hydraulic conductivity tensor. As data become available to support estimates of a directionally-dependent hydraulic conductivity tensor at the C-Holes, the FEHMN code, a finite-element code developed at Los Alamos (Zyvoloski et al. 1995a, 1995b), will be implemented to predict flow fields and possibly to also predict tracer transport (see Section 5.0, Future Work).

- The models assume that the packed-off zones in the injection and production wells are ideally mixed. In reality, there will be no equipment or injection tools that can assure good mixing in the injection zone, and because the flow is expected to be fracture-dominated, the tracers could enter the formation much earlier or later than would be predicted by assuming ideal mixing. However, the error associated with assuming ideal mixing should become less important if tracer pulses are followed by a water chase or if recirculating tests are conducted, as these strategies will tend to "push" tracers out of the borehole and into the formation quickly relative to travel times between wells.
- Flow fields are assumed to respond instantaneously to changes in the injection rate into the injection well. That is, if a tracer injection pulse is not followed by a water chase, or if it is followed by a chase or recirculation at a different flow rate, there is no attempt to account for a pressure decay or a gradual flow rate transition in the system (the steady-state flow field at the new injection rate is assumed instantly). The production flow rate is always assumed to be constant during the entire tracer test.
- The injection and production wells are both assumed to be perfectly vertical (or at least perpendicular to the formation), and they are assumed to have the same elevation at the midpoint between the packers (same z-centerline). These assumptions are not strictly correct at the C-Holes, but the errors introduced as a result of the assumptions should be minor compared to the likely errors in the assumed flow fields.
- Sorption of reactive tracers to the fracture walls is ignored. To justify this assumption, one must consider that the retardation coefficient resulting from sorption to parallel-plate fracture walls is (Freeze and Cherry 1979):

$$R = 1 + \frac{2K_a}{a} \qquad (13)$$

where, K_a = distribution coefficient based on rock surface area, rock surface area, and
a = fracture aperture.

In batch sorption experiments conducted by Fuentes et al. (1989), lithium had a K_d of approximately 1cm^3 H_2O/g on crushed Prow Pass tuff (from the C-Holes) that had a surface area of at least 1900 cm^2/g (minimum value reported). Using these data (K_a= 1/ 1900 = 0.00053 cm^3 H_2O/cm^2), the retardation coefficient given by equation (13) will be ~1.05 for a fracture aperture of 0.2 mm. Thus, for reasonable fracture apertures, sorption to the fracture walls should have a negligible effect on lithium transport at the C-Holes. However, in systems with low matrix porosities and large distribution coefficients, it may be necessary to account for sorption to fracture walls.

3.0 RESULTS OF PARTICLE-TRACKING MODEL SIMULATIONS

A large number of particle-tracking simulations were conducted to investigate sensitivities to various parameters that will either be controlled or are subject to uncertainty at the C-Holes. The following parameters that can be controlled were varied in the simulations:

- Injection Well (C#1 or C#2)
- Volume of Injected Fluid
- Volume and Duration of Chase Fluid
- Recirculation Flow Rate (if any)
- Production Flow Rate (Withdrawal Rate out of C#3)

In all simulations, it was assumed that injection and production would be into/out of the Bullfrog "aquifer", which is between the 3rd and 4th packers from the surface in all three wells (see Figs. 3-6). This "aquifer" will probably be the first to be tested at the C-Holes because of its large hydraulic conductivity. Seven injection/chase/recirculation strategies were considered in the simulations:

(1) Injection of 120 gal. of tracer solution at a rate of 20 gpm for 6 min. (no chase or recirculation).
(2) Injection of 120 gal. of tracer solution at a rate of 20 gpm followed by a 60 min. chase of water at 20 gpm (total injection time of 66 min.: 6 min. of injection, and 60 min. chase)
(3) Injection of 120 gal. of tracer solution at a rate of 20 gpm followed by continuous partial recirculation of produced fluid at 20 gpm.
(4) Injection of 120 gal. of tracer solution at a rate of 20 gpm followed by a 120 min. chase of water at 20 gpm (total injection time of 126 min.: 6 min. of injection, and 120 min. chase)
(5) Injection of 120 gal. of tracer solution at a rate of 200 gpm (36 sec. injection time) followed by full recirculation of produced fluid at 200 gpm.
(6) Injection of 120 gal. of tracer solution at a rate of 100 gpm (36 sec. injection time) followed by full recirculation of produced fluid at 100 gpm.
(7) Injection of 120 gal. of tracer solution at a rate of 50 gpm (36 sec. injection time) followed by full recirculation of produced fluid at 50 gpm.

Most of the simulations focused on the 200 gpm production rate, injection into C#2 (the well closer to C#3), and the third injection strategy listed above.

Uncontrolled parameters that were varied in the simulations, and the parameter values that were used, are listed below:

- Confined or Unconfined Aquifer (**2-D** and 3-D models exercised)
- Fracture Porosity (**0.001**, 0.002)
- Matrix Porosity (0.11, **0.2**, 0.35)
- Retardation Coefficient (4.0, **7.5**, 12.0)
- Average Fracture Aperture (**0.02 cm**, 0.05 cm)

- Free Diffusion Coefficient of Solute (**10^{-5} cm^2/sec**, 10^{-6} cm^2/sec, 2 x 10^{-7} cm^2/sec)
- Peclet Numbers Tangent (**0**, 20, 5) and Normal (**0**, 100, 10) to Flow Direction (Note: Zero Peclet number means no dispersion.)

The boldface numbers are "base case" values. In cases where data exist, these values are the best estimates of the parameters for the Bullfrog tuff formation. The lower and upper values used for matrix porosities and retardation coefficients are lower and upper bounds based on available data. In calculating the retardation coefficient, K_d values of 0.3, 0.65, and 1.1 cm^3/g were used as lower, middle, and upper estimates (based on laboratory measurements of lithium sorption on Bullfrog tuff at different concentrations of lithium at 38°C - Robinson et al. in press). Equation (9) was used to calculate the retardation coefficient assuming a tuff bulk density of 2.0 g/cm^3 (based on a rock density of 2.6 g/cm^3 and a porosity of 0.2) and a matrix porosity of 0.2. The retardation coefficient was not adjusted for different values of matrix porosity (that is, the values of 4, 7.5, and 12 were used regardless of the matrix porosity chosen for a given simulation).

Parameters that were <u>not</u> varied in the simulations, and the values used for these parameters were

- Distance between wells: 86.1 m for C#1 to C#3, 31.7 m for C#2 to C#3 (average distances in Bullfrog tuff formation).
- Production interval length (distance between packers): 115.8 m in C#3.
- Injection interval length (distance between packers): 96.9 m in C#1, 93.6 m in C#2. <u>Note</u>: In the 2-D model, the production and injection intervals are assumed to be the same length. In this case, the length of the injection zone was used.
- Depth to injection/production zones: 700 m (approximate).
- Tortuosity in matrix: 0.1.
- Ambient flow rate: 2.8 x 10^{-6} m/sec.
- Ambient flow direction: 114 degrees east (north = 0 degrees).
- Borehole radii: 0.127 m (10 inches).
- Production pipe radius: 0.0365 m (2-7/8 inches).
- Injection pipe radius: 0.0365 m (2-7/8 inches).
- Number of particles simulated: 50,000.
- Cutoff time for simulations: 1,500,000 sec. (416.67 hrs).

All of these parameters (except for the last two, which simply controlled the simulations) were determined from the best available information. Although the injection tubing that initially will be used at the C-Holes is 1.66" in diameter, the injection tubing in the simulations was assumed to be 2-7/8" diameter. This difference has virtually no effect on the simulations, as the residence time in the tubing is trivial compared to the residence times in the boreholes and in the formation. Likewise, the simulations are very insensitive to the depth to the production zone and the production pipe radius.

The results of selected simulations are presented as plots of normalized concentration vs. time (from start of injection) in Appendix C. The normalized concentration is the tracer concentration observed at the production wellhead (mass/volume) divided by the total tracer mass injected, which has units of reciprocal volume. This quantity is

useful because the expected concentrations at the wellhead can be quickly calculated by multiplying the normalized concentration by the injected mass. For instance, if the peak normalized concentration is 5 x 10^{-7}/L and the injected tracer mass is 1000 g, the expected peak concentration at the wellhead will be 5 x 10^{-4} g/L, or 0.5 ppm. Most of the breakthrough curves in Appendix C have a "noisy" appearance, which is due to the fact that they are frequency distributions of the residence times of a finite number of simulated particles. The noise can be reduced by simulating a larger number of particles, but at an increased computational cost. It was found that 50,000 particles was a good compromise in the tradeoff between noise and computation time.

Figures C.1 to C.3 show breakthrough curves for the three different types of tracers (fracture-flow-only, nonsorbing solute, sorbing solute) for transport between C#1 and C#3. The fracture-flow-only tracer is intended to represent a polystyrene microsphere tracer that does not experience attenuation due to settling or deposition. Each of these figures corresponds to one of the first 3 injection/ production strategies described above. The parameter values used in the simulations correspond to the base case, which are the boldface values given above. Figures C.1 to C.3 clearly show that solute recovery from C#1 to C#3 is expected to be extremely low — probably too low to quantify. The reason for the low recovery of nonsorbing solute is matrix diffusion, and the essentially zero recovery of sorbing solute is due to both matrix diffusion and sorption to the matrix. However, it must be remembered that these simulations assume a homogeneous, isotropic medium. It can be concluded that if greater tracer recoveries are desired, one must hope that the actual parameter values in the formation differ from the estimated values in such a way that transport is enhanced and/or that there is anisotropic flow with the preferred flow direction being from C#1 to C#3. The latter may be a realistic hope, as the original selection of the C-Hole locations was based on the belief (from available geophysical data) that the preferred flow direction would be roughly from C#1 to C#3.

Figure C.4 shows the fracture flow breakthrough curves from Figs. C.1 to C.3 for each of the 3 injection/production strategies. The different shapes of the curves can be attributed to the different injection strategies and the large dead volume in the injection zone. When tracer injection is not followed by chase or recirculation, only a small amount of tracer is pushed into the formation during the injection phase, and the remainder must slowly move out of the borehole as a result of the low flow rate that the borehole sees in the flow field that converges to C#3. The resulting breakthrough curve is essentially an exponential decay that reflects the slowly decreasing tracer concentration in the well-mixed injection zone coupled with a time delay for transport from C#1 to C#3. When tracer injection is followed by a 1 hour chase of water at 20 gpm, the amount of tracer pushed into the formation is greatly increased, and consequently a much smaller amount remains in the injection zone to experience the exponential decay. When there is recirculation at 20 gpm, the exponential decay in the borehole is essentially unnoticeable because all the tracer is pushed into the formation quickly relative to the time it takes to move to C#3. The tracer peak also arrives significantly sooner when there is recirculation because the recirculation increases the effective flow rate toward C#3. Tracer dispersion appears to be greater with recirculation (although this is hard to distinguish from the exponential decay out of the injection zone) because the tracer is forced to follow trajectories that have a greater range of lengths and travel times than in the case of no recirculation (see Figs. 12 and 13). If borehole storage effects are ignored, dispersion will always appear to be greater as the recirculation ratio (ratio of injection to

production flow rate) increases. This apparent dispersion has nothing to do with the properties of the formation; it is strictly a byproduct of the flow fields associated with various recirculation ratios.

Figure C.5 shows fracture flow breakthrough curves from 3-D simulations of transport between C#1 and C#3. By comparing Figs. C.4 and C.5, it is seen that the assumption of an unconfined aquifer (3-D model) results in longer arrival times and lower recoveries than the assumption of a confined aquifer (2-D model), which is to be expected.

Figures C.6 and C.7 are similar to Figs. C.4 and C.5 except that they show the breakthrough curves of the nonsorbing solute between C#1 and C#3 (in 2-D and 3-D). It is important to note that it would be impossible to determine from the shapes of the curves whether borehole storage effects are influencing the tracer tests. If one were to interpret the breakthrough curves without accounting for borehole storage, one would reach different conclusions about each curve. The curve that best reflects the transport characteristics of the formation is the recirculation curve because in this case the tracer spends the least amount of time in the injection borehole. Breakthrough curves are not shown for the sorbing solute because there was essentially no recovery of this tracer in the C#1-to-C#3 simulations.

Figures C.8 through C.14 are the equivalent of Figs. C.1 through C.7 except that they show the results of transport simulations between C#2 and C#3 (otherwise, the same injection/production scenarios and base case parameter values were assumed). Additionally, Figs. C.15 and C.16 show breakthrough curves for a sorbing solute between C#2 and C#3. It is clear that the travel times are shorter and recoveries are greater between C#2 and C#3 than they are between C#1 and C#3 because of the shorter distance between the wells. It is also apparent that the shorter well separation results in much less difference between the 2-D and 3-D simulations than there was in the C#1-to-C#3 simulations. Thus, the unconfined case behaves more like the confined case when the wells are close together. The borehole storage effects are apparent in the C#2-to-C#3 breakthrough curves, but the exponential decay is faster than in the C#1-to-C#3 curves because of the greater flow rates and hence more rapid flushing of the injection zone that occurs when the wells are closer together.

Because the recirculation breakthrough curves were less affected by borehole storage effects than the injection-only or one-hour-chase curves, the investigation of sensitivities to uncontrolled parameters focused on the 200 gpm production - 20 gpm recirculation strategy. They also focused exclusively on 2-D transport from C#2 to C#3, as many of the transport simulations for C#1 to C#3 resulted in no recovery of sorbing solute. Figures C.17 to C.19 show the effects of fracture porosity and the average fracture aperture on the breakthrough curves of each type of tracer. When the fracture porosity is increased and the aperture remains constant, it is implied that the fracture spacing has decreased. Conversely, when the aperture is increased and the porosity remains constant, it is implied that the fracture spacing has increased. Figure C.17 shows that the fracture flow breakthrough curves are sensitive only to the fracture porosity, and that travel times increase as porosity increases. This trend is expected from the dependence of flow velocity on porosity indicated in equation (5).

Figure C.18 shows that nonsorbing tracer transport is enhanced by increasing the average fracture aperture (with porosity remaining constant), and slowed down by increasing the porosity (with aperture remaining constant). The latter effect is due in

part to the greater groundwater travel time in the fractures when the porosity is greater, but it is also due to the greater opportunity that the tracer has to diffuse into the matrix when fracture flow rates are lower. The nonsorbing tracer actually spends a greater percentage of time in the matrix in the high fracture porosity case because the greater residence time in the fractures allows the tracer to diffuse further into the matrix. The enhanced transport in the larger average aperture case is due to the fewer number of collisions that the tracer has with the fracture walls when the aperture is larger. The fewer collisions results in less opportunity to diffuse into the walls. Figure C.19 shows that the sorbing tracer follows the same trends as the nonsorbing tracer.

Figures C.20 to C.22 show the effects of matrix porosity on the breakthrough curves of each type of tracer. Because the "fracture only" tracer does not enter the matrix, the breakthrough curves of this tracer are identical at the different matrix porosities (Fig. C.20). Figures C.21 and C.22 show that the effective retardation of both the nonsorbing and the sorbing tracers increases as the matrix porosity increases. This can be attributed to the fact that, as matrix porosity increases, particles have a greater probability of entering the matrix when they collide with fracture walls, hence they spend more time in the matrix.

Figures C.23 and C.24 show the effects of the retardation coefficient on the breakthrough curves of nonsorbing and sorbing tracers. As expected, the nonsorbing tracer is unaffected by this parameter (Fig. C.23), but the apparent recovery of sorbing tracer decreases as the retardation coefficient increases (Fig. C.24). However, unlike ideal transport through a porous column, where the first arrival of sorbing tracer is expected to be delayed relative to the nonsorbing tracer by a factor approximately equal to the retardation coefficient, Fig. C.24 shows that the first arrival time of sorbing tracer is not a strong function of the retardation coefficient. A larger retardation coefficient results in a lower apparent tracer recovery but not a significantly delayed first arrival time. This occurs because of the high flow rate through the fractures in the forced-gradient tracer tests. The solute tracers effectively cannot "sense" the vast majority of the stagnant water in the matrix where sorption is assumed to occur, so much less sorption occurs relative to what would be expected if all of the pore water were accessible. If proper consideration is not given to this phenomenon when interpreting sorbing solute tracer tests, one might conclude that there is less sorption occurring in the tests than predicted by batch or column sorption experiments. In reality, the lower apparent sorption can be fully accounted for by mass transfer limitations rather than by a lower sorption coefficient (K_d). It should be noted that the expression "apparent recovery" has been used carefully in this paragraph to describe the decreased recovery of sorbing solute as the retardation coefficient increases. Strictly speaking, when sorption is reversible, recovery should not decrease but rather it should be delayed when the retardation coefficient increases. The recovery appears to decrease as a function of retardation coefficient only because of the finite duration of the simulated tracer tests, which is a practical limitation in any field tracer test.

Figures C.25 and C.26 show the effects of free diffusion coefficient on the breakthrough curves of nonsorbing and sorbing tracer (the fracture flow tracer is unaffected by this parameter because it does not diffuse into the matrix). These figures illustrate that much greater recoveries of both types of solute tracers can be expected as free diffusion coefficients decrease. This occurs because tracers with smaller diffusion coefficients have fewer collisions with fracture walls and hence less opportunity to

diffuse into the matrix than tracers with larger diffusion coefficients. It is interesting to note that the FBAs that the USGS/UNLV intend to use as conservative tracers should have significantly smaller diffusion coefficients than bromide (which will be used as a conservative tracer by Los Alamos). As a first approximation, the differences between the diffusion coefficients may be as much as a factor of 2 to 3 (with the bromide being around 10^{-5} cm^2/sec and the FBA's around 3 x 10^{-6} cm^2/sec), so the differences in the breakthrough curves of the FBA's and bromide might be expected to be nearly as great as those shown in Fig. C.25. The breakthrough curves associated with the diffusion coefficient of 2 x 10^{-7} cm^2/sec in Figs. C.25 and C.26 are essentially identical to those for a tracer that does not diffuse into the matrix. This result is partially an artifact of the manner in which the particle-tracking models account for matrix diffusion. When particle diffusion coefficients are less than or equal to 2 x 10^{-7} cm^2/sec the criteria that N_{DL} must be greater than 0.7 before matrix diffusion is considered (see equation 10) is seldom satisfied in the models. Thus, for tracers with small diffusion coefficients, the models tend to underpredict the amount of matrix diffusion that the tracers will experience. However, the results for the two larger diffusion coefficient tracers in Figs. C.25 and C.26 should be valid, and the trends shown in these figures are certainly valid.

Figures C.27 and C.28 show the effects of Peclet number on the breakthrough curves of the fracture flow and nonsorbing tracers. The curves are labelled with the Peclet numbers used in the simulations. The first number is the longitudinal Peclet number, and the second number is the transverse Peclet number. It is apparent that the inclusion of dispersion in the simulations causes considerable spreading of the fracture flow breakthrough curves (Fig. C.27), which is expected. However, it is also apparent that there is a considerable amount of flow field dispersion even when the dispersion coefficient is equal to zero. This dispersion occurs as a result of the particle trajectories of different lengths and travel times that are inherent in the partial recirculation flow field, and it illustrates the importance of accounting for flow field dispersion when trying to deduce formation dispersion coefficients from tracer breakthrough curves. In essence, the flow field contributes a certain amount of dispersion that, in reality, does not reflect the true dispersive characteristics of the formation and will result in overestimation of formation dispersivity if it is not "subtracted out". Figure C.28 shows that the effect of dispersion on the nonsorbing solute is more subtle than that on the fracture-flow-only tracer, with the shape of the breakthrough curves essentially being the same at different Peclet numbers, but the apparent recoveries decreasing as Peclet number(s) decrease. The observed "dispersion" in this case is a combination of both classical dispersion and matrix diffusion. The apparent tracer recovery decreases as dispersion increases because a larger fraction of the tracer spends a greater amount of time in the flow system and is therefore retarded to a greater extent by matrix diffusion. The increased fraction of tracer that spends a longer time in the flow system is seen qualitatively in the tails of the breakthrough curves of the fracture-flow-only tracer in Fig. C.27 (the mass in the tails increases as the amount of dispersion increases). It can be concluded that for greater amounts of classical dispersion in a flow system, the apparent recovery of solute tracers is expected to decrease, primarily because of increased influence of matrix diffusion.

Figures C.29 to C.31 show comparisons of tracer breakthrough curves assuming different injection/production strategies. The strategies all involve recirculation flow rates of at least 20 gpm so that borehole storage has a minimal effect on the apparent

dispersion in the breakthrough curves. Figure C.29 illustrates that, even with some flushing of the injection zone to minimize borehole storage effects, one can expect different amounts of tracer dispersion as a result of the different flow fields that occur with different recirculation ratios (the breakthrough curves in this figure are unaffected by matrix diffusion, and classical formation dispersion was "turned off" in these simulations). The curves are labelled with two numbers separated by a dash; the first number is the production flow rate and the second number is the recirculation flow rate. The curve in Fig. C.29 that is labelled "100-20 Corr." has been "corrected" by multiplying all times by 0.5 to account for the fact that the production rate was half what it was in the other simulations. This, in effect, normalizes all of the curves to show breakthrough as a function of volume of water produced, which is a more meaningful comparison when production flow rates differ. It is apparent that the breakthrough curve for full recirculation has an earlier first arrival time and more flow field dispersion than the other curves. The earlier first arrival time can be attributed to the larger flow rate out of the injection well, which provides additional "push" of tracer toward the production well. The greater dispersion is due to the much longer particle trajectories and travel times that occur with full recirculation (compare Figs. 10 and 11, for instance). There is slightly more dispersion in the case with 20% recirculation than in the case with 10% recirculation because the flow streamlines tend to "fan out" more between the wells as the amount of recirculation increases. Figures C.30 and C.31 show the nonsorbing and sorbing solute breakthrough curves, respectively, for the same injection/production strategies as in Fig. C.29. It is apparent that greater residence times in the system (caused by lower flow rates) tend to decrease the apparent recoveries of both types of solutes. This effect can be attributed to the increasing influence of matrix diffusion and sorption in the matrix that results when tracers have more access to the matrix.

Figures C.32 to C.34 show how tracer recoveries in tests between C#1 and C#3 could be improved over the "base case" (presented in Figs. C.1 through C.7) by (1) employing full recirculation at 200 gpm, and (2) assuming that the formation parameters all take on their most favorable values for tracer transport (fracture porosity = 0.001, matrix porosity = 0.11, fracture aperture = 0.05 cm, retardation coefficient = 4.0; Note that none of these parameters affect the fracture-flow-only breakthrough curve). It is apparent from these figures that full recirculation at 200 gpm can lead to increased recoveries of solute tracers relative to the base case, primarily because of the faster flow pathways that some of the injected tracer mass will experience. However, it is also clear that favorable transport parameters would have a much more beneficial effect on the recovery of tracers. The "optimal" case is intended to show "the best that can be expected" in a tracer test between C#1 and C#3 if the formation is assumed to be homogeneous and isotropic.

All of the tracer breakthrough curves presented in Appendix C and discussed up to this point have <u>not</u> included the effects of recirculation. Figure C.35 shows how the breakthrough curves are affected when recirculation is taken into account in the case of full recirculation at 200 gpm between C#2 and C#3. The breakthrough curves for sorbing tracer are not shown in this figure because the effects of recirculation are almost unnoticeable for this tracer. Probably the most important practical consideration with recirculation is that it will tend to increase the tailing of breakthrough curves, and this effect must be accounted for when interpreting recirculating tracer tests.

4.0 RECOMMENDATIONS FOR REACTIVE TRACER TESTS AND PREDICTIONS FOR RECOMMENDED TESTS

From the discussion of the simulation results in Section 3.0 and the plots in Appendix C, a case can be made that the best approach to efficiently investigate the effects of matrix diffusion and sorption in reactive tracer tests is to conduct tests at different flow rates between the same wells and in the same formation. The incremental effect of sorption on tracer transport can be qualitatively established in a single test by observing differences between sorbing and nonsorbing solute breakthrough curves. However, without testing at different flow rates, it will be impossible to differentiate between the dispersive effects of flow in the formation and the dispersive effects of matrix diffusion, as both phenomena can give rise to long tails that are frequently observed in tracer breakthrough curves. It will also be difficult to establish whether there is significant sorption occurring on fracture surfaces or if all sorption is occurring in the matrix. Assuming that the flow field dispersion is kept constant in each case (and also assuming that classical formation dispersion does not vary with flow rate, which will be true only if the dispersion coefficient is proportional to fluid velocity [i.e., D =]), tests at different flow rates should allow the effects of matrix diffusion to be observed directly as a decrease in the apparent recovery of conservative tracer with decreasing flow rate. Similarly, apparent decreases in the recovery of sorbing solute as flow rates decrease can be attributed to sorption occurring in the matrix (as opposed to sorption occurring strictly on the fracture walls, which would be indicated by a slight delay in arrival time but little or no difference in apparent recovery). As an alternative to conducting tests at different flow rates, matrix diffusion could be studied by using conservative tracers with significantly different diffusion coefficients in a single test (see Fig. C.25), and sorption could be studied by using sorbing tracers with different retardation coefficients in a single test (see Fig. C.24). However, at the present time, there are only two general classes of conservative solutes with significantly different diffusion coefficients that can be used at the C-Holes (fluorinated benzoic acids and halides [microspheres represent a third class, but they should not diffuse into the matrix at all]); and, more importantly, there is only one sorbing solute (lithium) that can be used at the C-Holes. Because of the time and cost associated with characterizing additional tracers (i.e., measuring diffusion coefficients and/or sorption parameters) and obtaining environmental permits to use such tracers, it is preferable to study matrix diffusion and sorption by conducting tests at different flow rates using currently available tracers.

Because of the shorter distance between C#2 and C#3 (compared to C#1 and C#3), it is advisable to initially conduct tests betweeen these two wells. Although it would ultimately be desirable to study transport between different wells and in different formations, if studying the mechanisms of matrix diffusion and sorption are given top priority (as they should be), it would be prudent to hold as many uncontrolled parameters constant as possible while varying controlled parameters that affect matrix diffusion and sorption. This strategy would dictate conducting tests at different flow rates in the same formation and between the same wells.

The only controlled parameters that can be realistically varied at the C-Holes when conducting tests in a given formation and between the same two wells are the injection/production strategies and the injected tracer mass. It should be clear from Section 3.0 that it is highly desirable to avoid or minimize borehole storage effects that occur as a

result of tracers not being pushed out of the borehole with a water chase or recirculation. A push into the formation is especially important because there is no way of knowing for sure whether the injection zone will truly behave as a well-mixed region (as modeled in this study) or whether the effective volume of the injection zone will be the same as the entire volume of the zone. The uncertainty associated with borehole storage can be minimized only by following tracer injection with two or more injection zone volumes of water, as this amount of water should be sufficient to flush most of the tracer out of the borehole and into the formation. It is also desirable to try to conduct tests with flow fields that are as similar as possible so that flow field dispersion is approximately the same in each test. In this case, all of the differences in tracer breakthrough curves at different flow rates can be attributed to differences in matrix diffusion and/or sorption rather than differences in dispersion resulting from different flow field streamlines. Although flow field dispersion can effectively be "backed out" of the calculations presented in this report because the flow fields are idealized, it will impossible to do this in a real system where the flow fields at different flow rates will not be known.

If flow rates are to be varied in different tests, the dual objectives of flushing boreholes and maintaining similar flow field dispersion can best be accomplished by conducting fully recirculating tests. In fully recirculating tests, the flow streamlines are predicted to be exactly the same regardless of the flow rate, so flow field dispersion should not vary. The same can be said about partial recirculation at different flow rates if the recirculation ratio is kept constant, but it will take longer to flush the boreholes if partial recirculation is employed. Even in fully-recirculating tests there will be a slight difference in the rate of borehole flushing at different flow rates, but for reasonable flow rates, the boreholes should be flushed in a relatively short time compared to travel times between wells, and borehole flushing will always be more rapid with full recirculation than with partial recirculation. These arguments should hold in a real formation that is not homogeneous and isotropic.

Figure 17 shows simulated fracture flow breakthrough curves for full recirculation at different flow rates between C#2 and C#3. The curves are corrected for flow rate differences in Fig. 17a. It is apparent from Fig. 17a that when breakthrough curves are normalized to the volume of water produced at C#3, there is very little difference between the apparent dispersion in the curves. The differences in the peak heights of the curves are an artifact of the manner in which the particle-tracking codes calculate concentrations, not in any real differences. Concentrations are calculated by summing all the particles that exit the system within a given time window and then dividing by the volume of water that was produced during this time window. The time windows are evenly spaced from the time of first tracer arrival until the end of the simulations (up to ~420 hrs), so the early time bins often have a very large number of particles in them. The early windows also tend to have many more particles in the early portion of the window than in the latter portion because of the nature of the dispersion in recirculating flow fields. At lower flow rates, the first arrival of tracer is later, so the time windows are narrower. The narrower windows result in higher peak concentrations because the ratio of particles to time window length increases as the windows get narrower. This artifact is not considered to be an important practical limitation because in a real system dispersion will tend to flatten any sharp peaks that might be predicted in an idealized breakthrough curve.

Figures 18, 18a, 19, and 19a show the predicted breakthrough curves of nonsorbing and sorbing tracers in fully recirculating tests at different flow rates between C#2 and C#3. The "a" figures in each case show the breakthrough curves normalized to the volume of water produced from C#3. Figure 20 shows the breakthrough curves for each tracer in the simulated test with the highest flow rate. These figures illustrate the trends that can be expected as a function of flow rate and as a function of the type of tracer in recirculating tests. As discussed in the first paragraph of this section, the incremental effect of sorption on tracer transport can be investigated by observing the differences between the sorbing and nonsorbing solute breakthrough curves in any given test, and the testing of conceptual models of matrix diffusion and sorption can be accomplished by observing and interpreting differences in the breakthrough curves of the same tracers in tests at different flow rates.

Although full recirculation probably represents the best strategy for conducting a series of tracer tests at different flow rates while maintaining comparable flow field dispersion in each test, it may be impractical at the C-Holes for a variety of reasons:

- The 1.66" injection tubing and cracking valve will not allow recirculation of water at very high flow rates.
- The injection zone may not be permeable enough to accept high recirculation flow rates without excessive pressure increases. The hydrocracking pressure at the C-Holes is believed to be quite low, so if a significant column of water develops in the injection tubing, damage to the formation may occur.
- Experience at other sites (e.g., the WIPP site near Carlsbad, NM) suggests that the permeability of the formation at the injection point can decrease as a function of

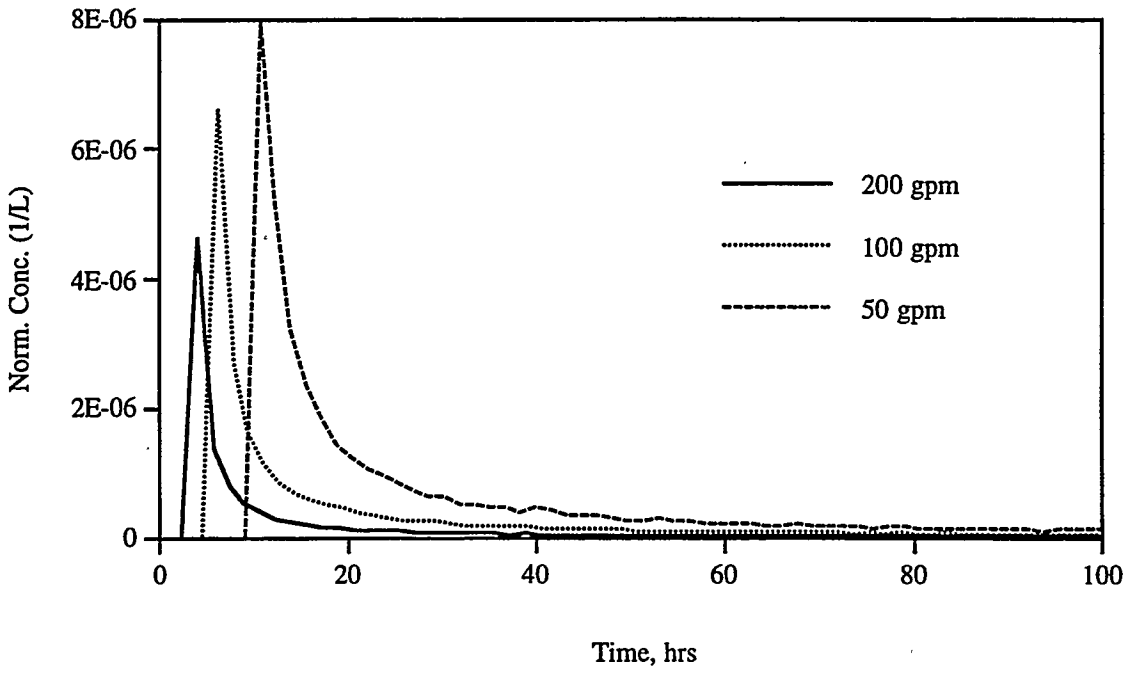

Fig. 17. Predicted breakthrough curves of fracture-flow-only tracer resulting from full recirculation at different flow rates between C#2 and C#3.

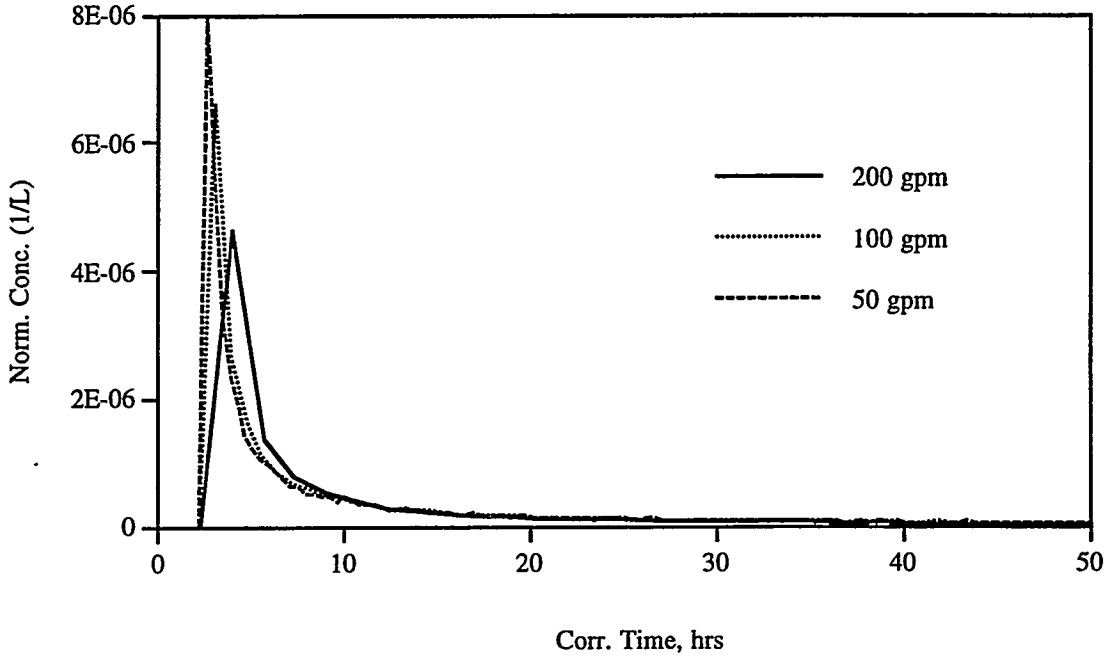

Fig. 17a. Breakthrough curves of Fig. 17 normalized to the volume of water produced (times are corrected by multiplying by flow rate/200 gpm).

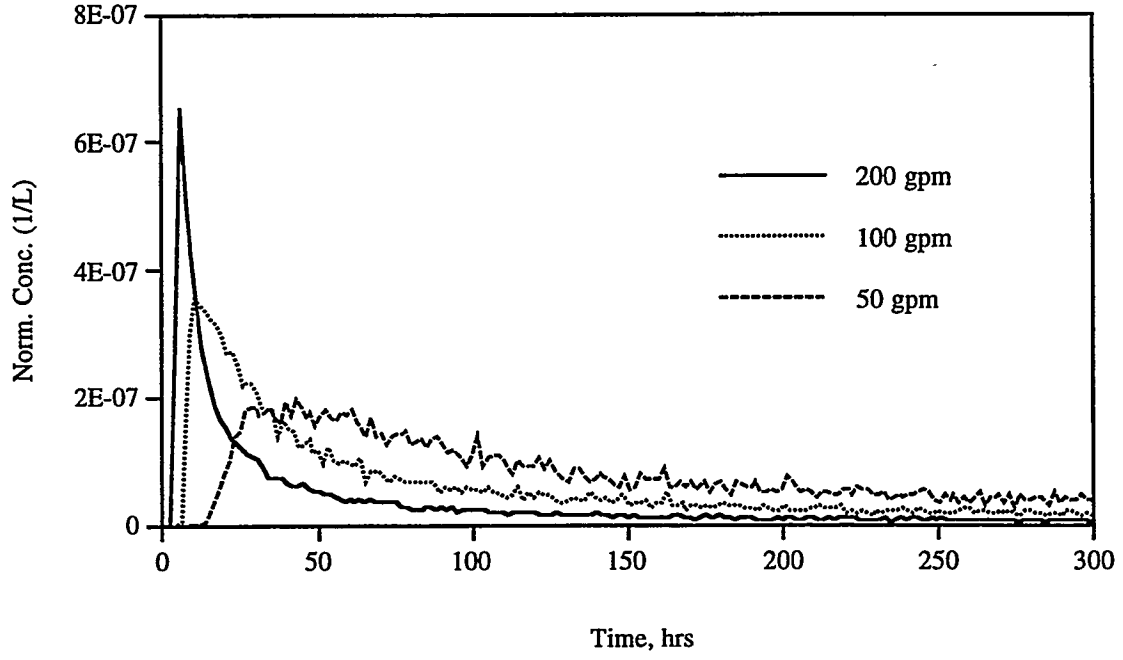

Fig. 18. Predicted breakthrough curves of nonsorbing tracer resulting from full recirculation at different flow rates between C#2 and C#3.

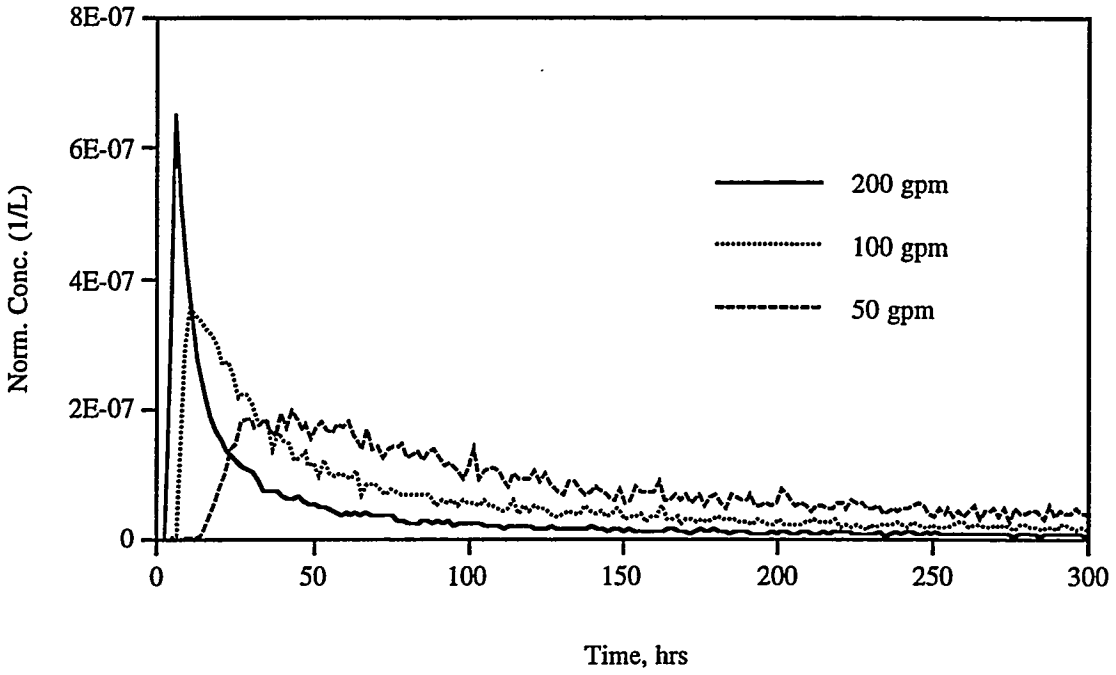

Fig. 18a. Breakthrough curves of Fig. 18 normalized to the volume of water produced (times are corrected by multiplying by flow rate/200 gpm).

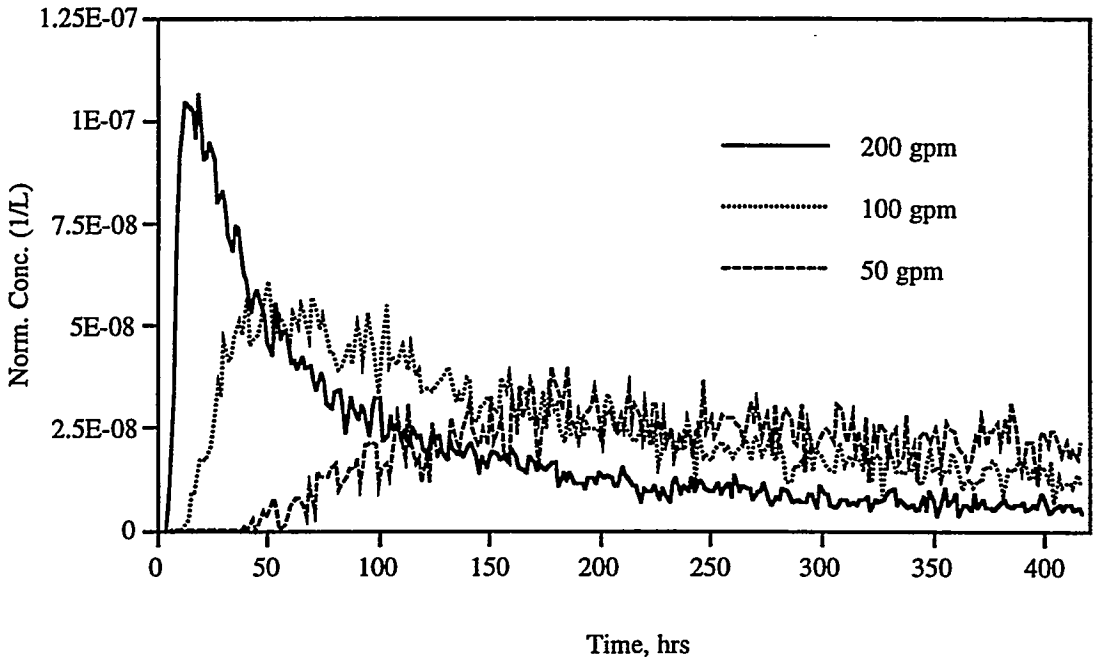

Fig. 19. Predicted breakthrough curves of sorbing tracer resulting from full recirculation at different flow rates between C#2 and C#3.

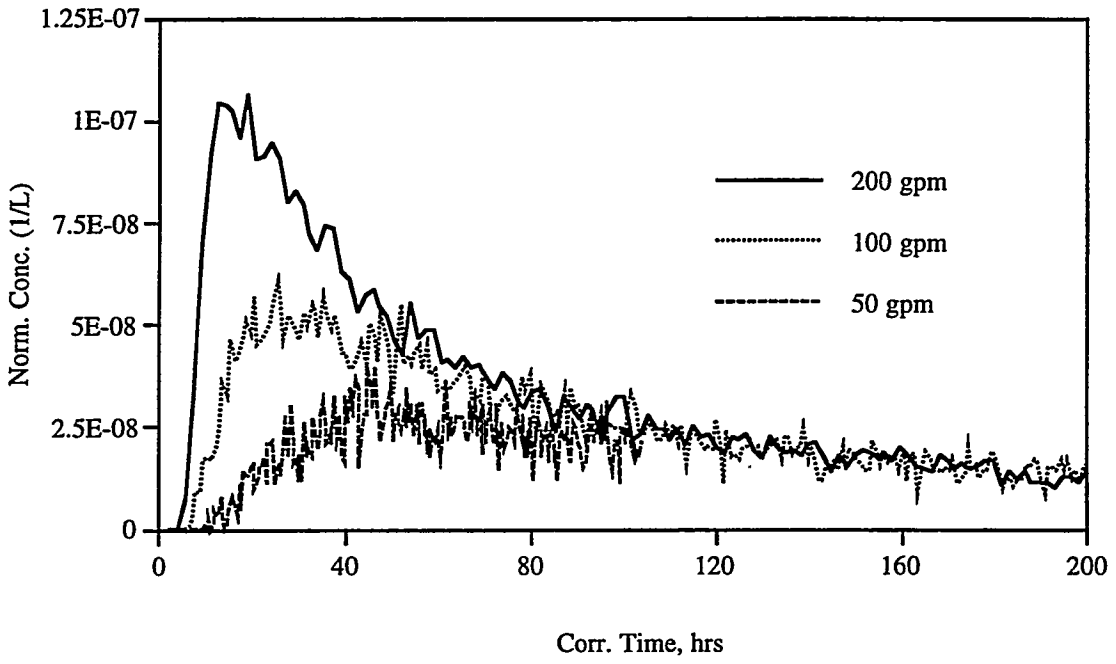

Fig. 19a. Breakthrough curves of Fig. 18 normalized to the volume of water produced (times are corrected by multiplying by flow rate/200 gpm).

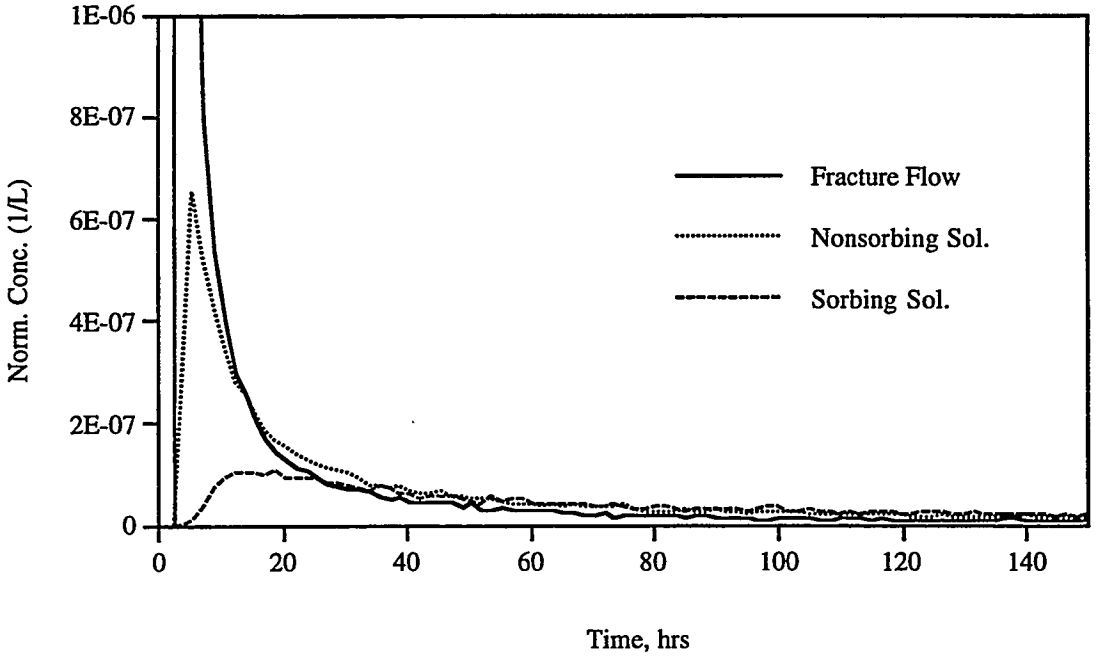

Fig. 20. Predicted breakthrough curves of each tracer resulting from full recirculation at 200 gpm between C#2 and C#3.

time in recirculating tests because of debris that is mobilized in the formation and then redeposited upon reinjection. This occurred at the WIPP site even when a bank of filters was used in the recirculation loop (Stensrud, 1995).

For these reasons, a preferable alternative to full recirculation may be a strategy where convergent tests are conducted at different production rates, but the tracer slug is pushed out of the injection zone by a volume of chase water equal to at least two injection interval volumes. Figures 21 and 21a show the flow field dispersion that can be expected in tests at different production rates between C#2 and C#3 when a 120 gal. slug of tracer solution is followed by a 2-hr chase of water at 20 gpm. This amount of chase water is sufficient to flush the majority of the tracer solution out of the injection zone. Figure 21a is a normalized version of Fig. 21, and it clearly shows that even though the flow streamlines will be different during the time that chasewater is injected, the effective flow field dispersion, when corrected for flow rate differences, is expected to be quite similar in the three scenarios. Figures 22 and 22a show the uncorrected and corrected breakthrough curves, respectively, for a nonsorbing tracer, and Figs. 23 and 23a show the breakthrough curves for a sorbing tracer. Figure 24 illustrates the differences that can be expected in the breakthrough curves of different tracers in the convergent test with the highest flow rate. If full recirculation cannot be employed, it is suggested that a series of convergent tests involving a significant volume of chase water, such as those depicted in Figs. 21 through 24, be utilized at the C-Holes to study matrix diffusion and sorption.

5.0 FUTURE MODELING WORK

As more hydrogeologic data become available, or perhaps as tracer test data are generated, it will undoubtedly become desirable or even necessary to model flow at the C-Holes using an anisotropic and/or spatially-dependent hydraulic conductivity tensor. As discussed in Section 2.8, the particle-tracking models described in this report do not support the use of an anisotropic hydraulic conductivity tensor, so another model would have to be used to conduct flow calculations. At the present time, the plan is to use the FEHMN (Finite Element Heat and Mass Transfer - Nuclear) code, developed at Los Alamos, to conduct such calculations (Zyvoloski et al. 1995a, 1995b). This code could also be used to calculate tracer transport, although tracer transport could be predicted using particle-tracking models in conjunction with flow fields calculated by FEHMN.

Figure 25 shows a 3-D finite-element discretization of the saturated zone in the vicinity of the C-Holes, which has been generated in anticipation of calculating anisotropic flow fields in interwell tracer tests. This grid of tetrahedral elements was generated using GEOMESH, another software package developed at Los Alamos (Gable et al. 1995). The grid is a very coarse discretization that has 14 vertical layers, corresponding to the 14 stratigraphic layers below the water table shown in Fig. 3. The layer boundaries in Fig. 25 have all been approximated as planes that have the same slope, so that none of the layers "pinch out". Each layer can be assigned a different set of hydrologic parameters. Using GEOMESH, the three wells can be superimposed onto this grid, and the grid can be modified to ensure that nodes occur at the wells. GEOMESH also allows the user to "dial in" various levels of mesh refinement within the coarse mesh. This

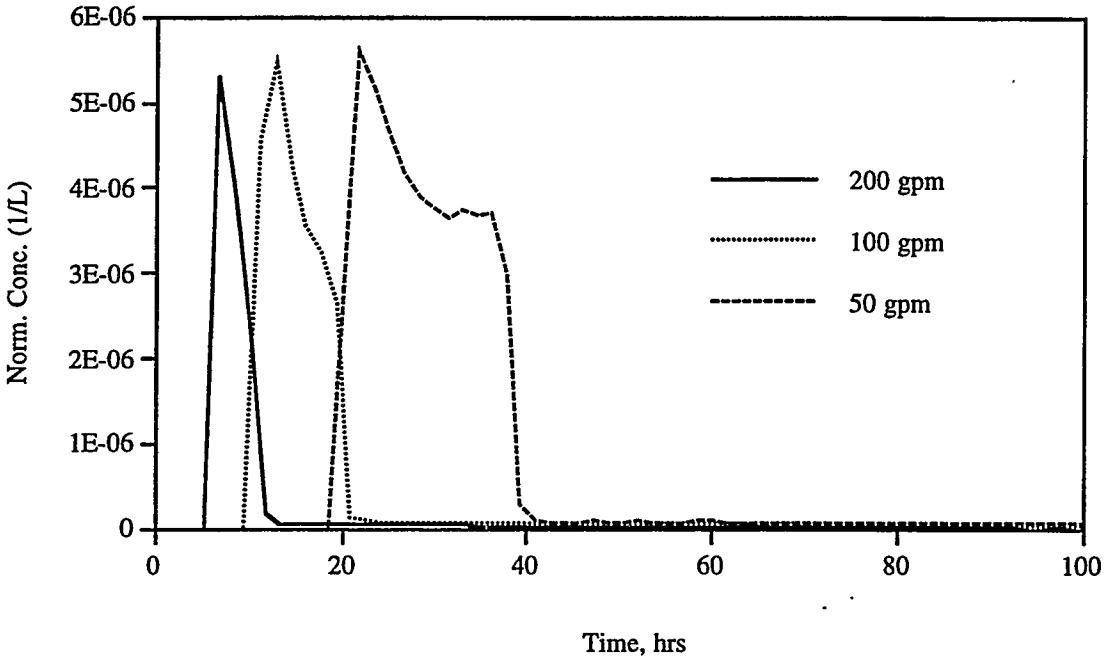

Fig. 21. Predicted breakthrough curves of fracture-flow-only tracer resulting from a 120-gal injection of tracer solution into C#2 followed by a 2-hr chase of water at 20 gpm with different production rates out of C#3.

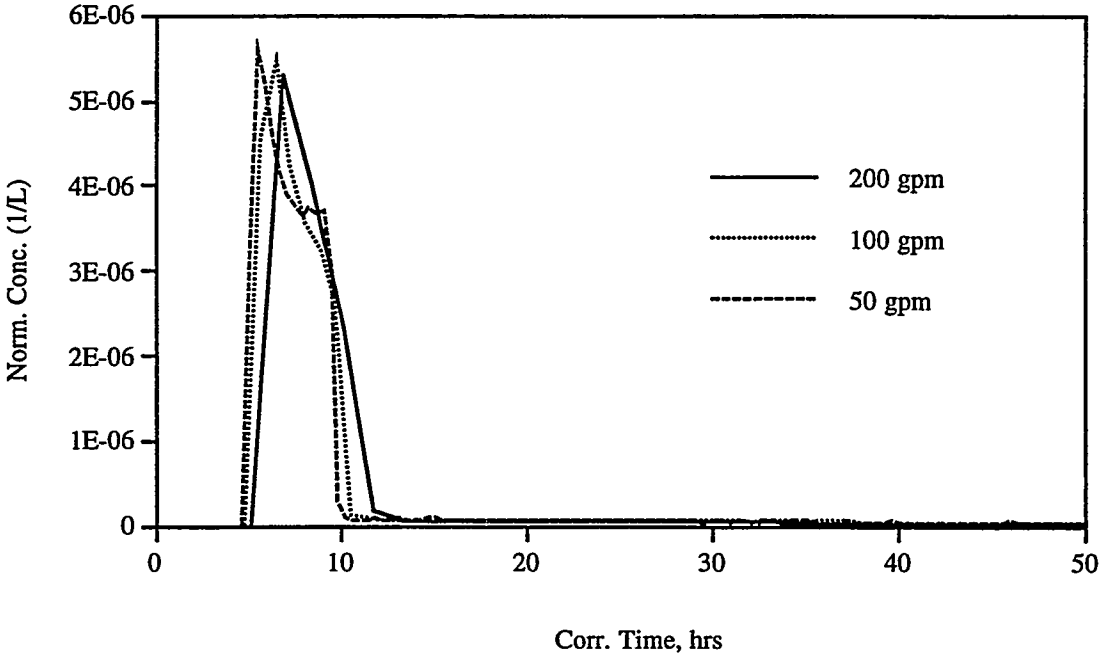

Fig. 21a. Breakthrough curves of Fig. 21 normalized to the volume of water produced (times are corrected by multiplying by production rate/200 gpm).

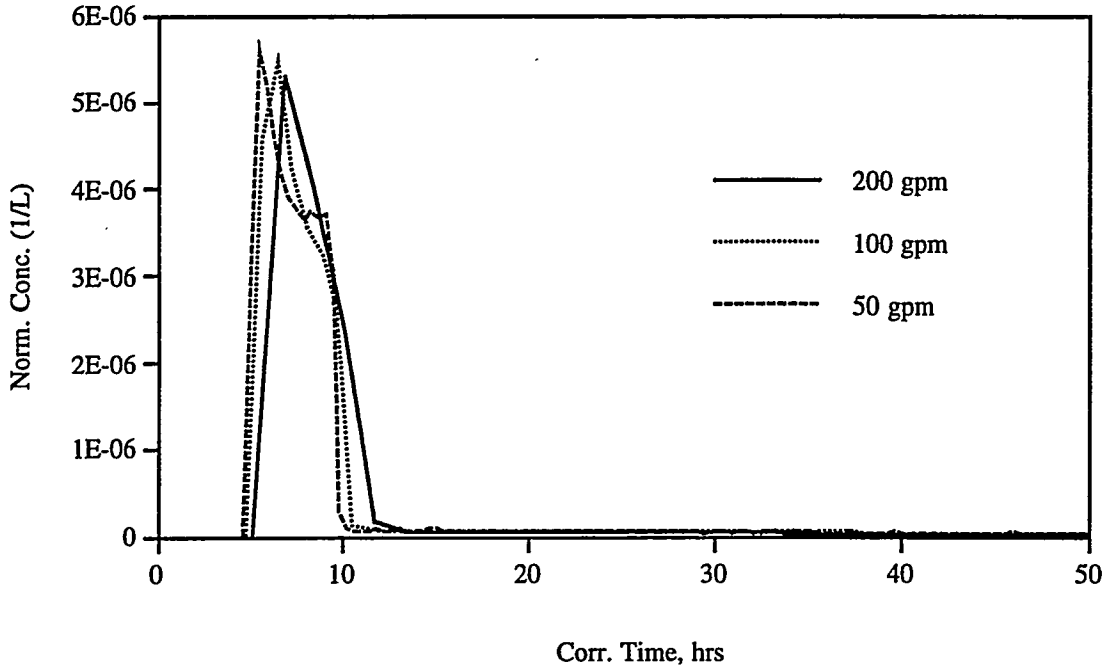

Fig. 22. Predicted breakthrough curves of nonsorbing tracer resulting from a 120-gal injection of tracer solution into C#2 followed by a 2-hr chase of water at 20 gpm with different production rates out of C#3.

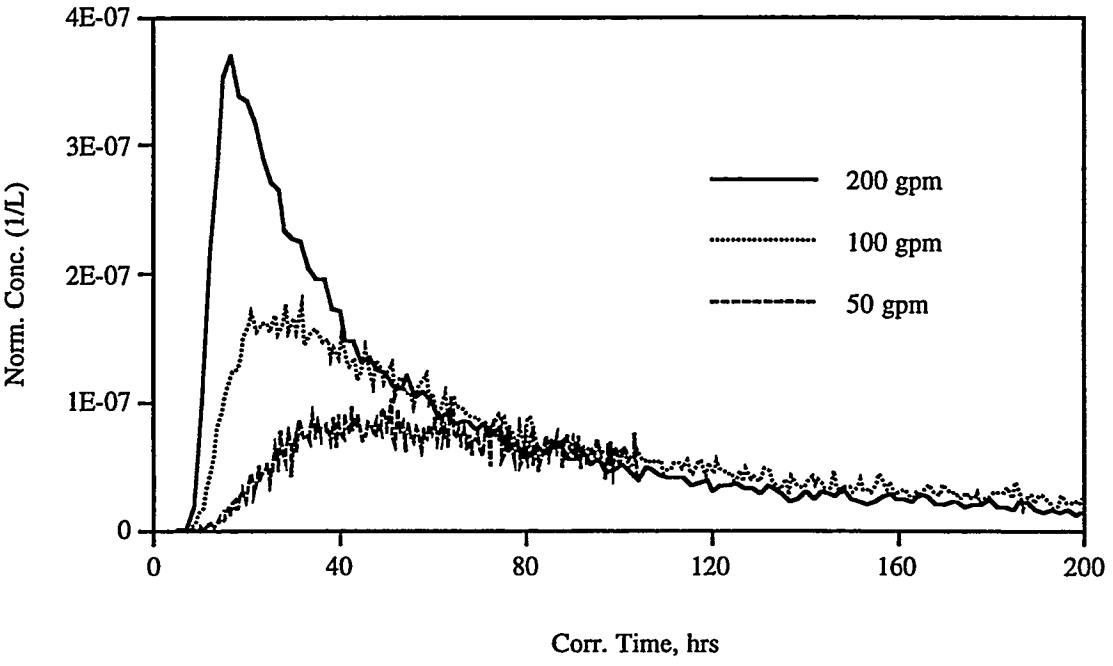

Fig. 22a. Breakthrough curves of Fig. 18 normalized to the volume of water produced (times are corrected by multiplying by production rate/200 gpm).

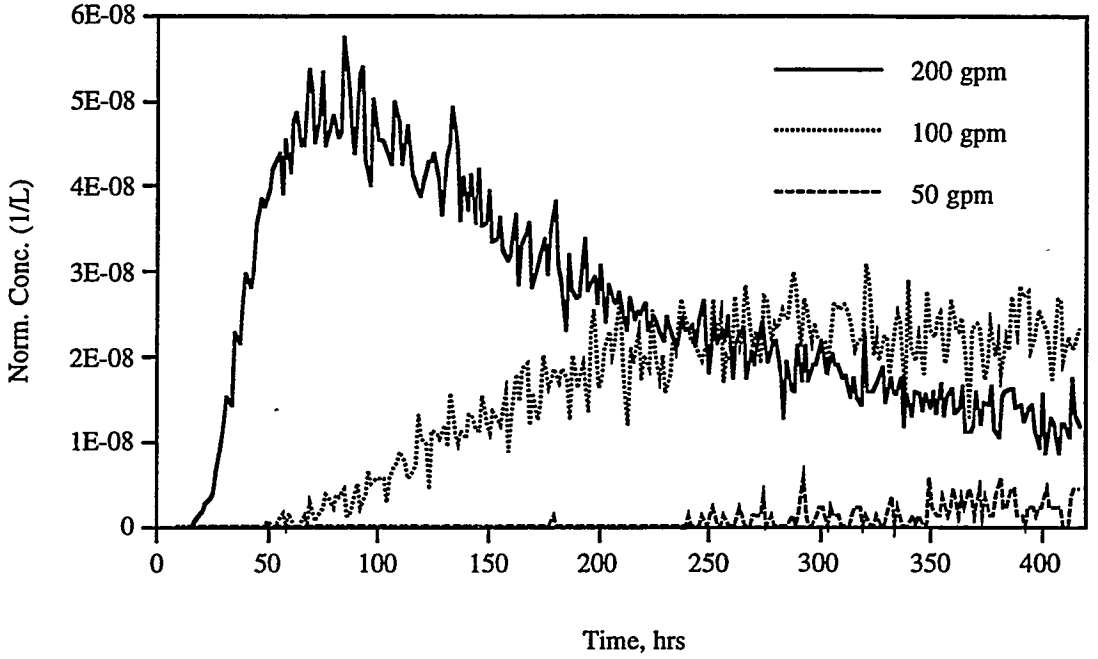

Fig. 23. Predicted breakthrough curves of sorbing tracer resulting from a 120-gal injection of tracer solution into C#2 followed by a 2-hr chase of water at 20 gpm with different production rates out of C#3.

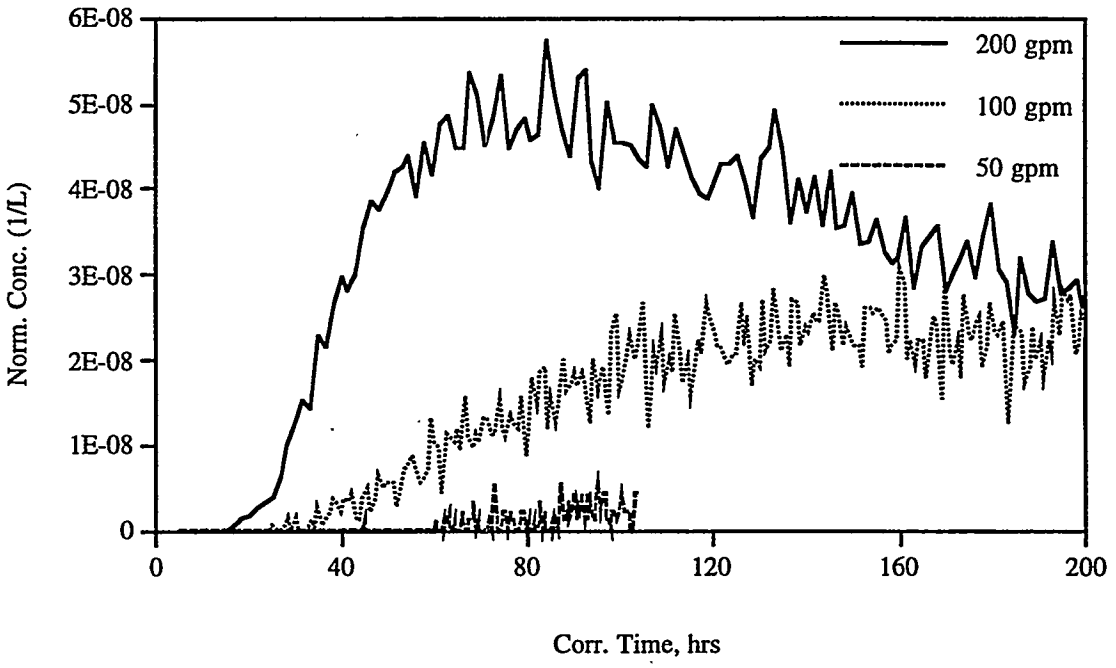

Fig. 23a. Breakthrough curves of Fig. 18 normalized to the volume of water produced (times are corrected by multiplying by production rate/200 gpm).

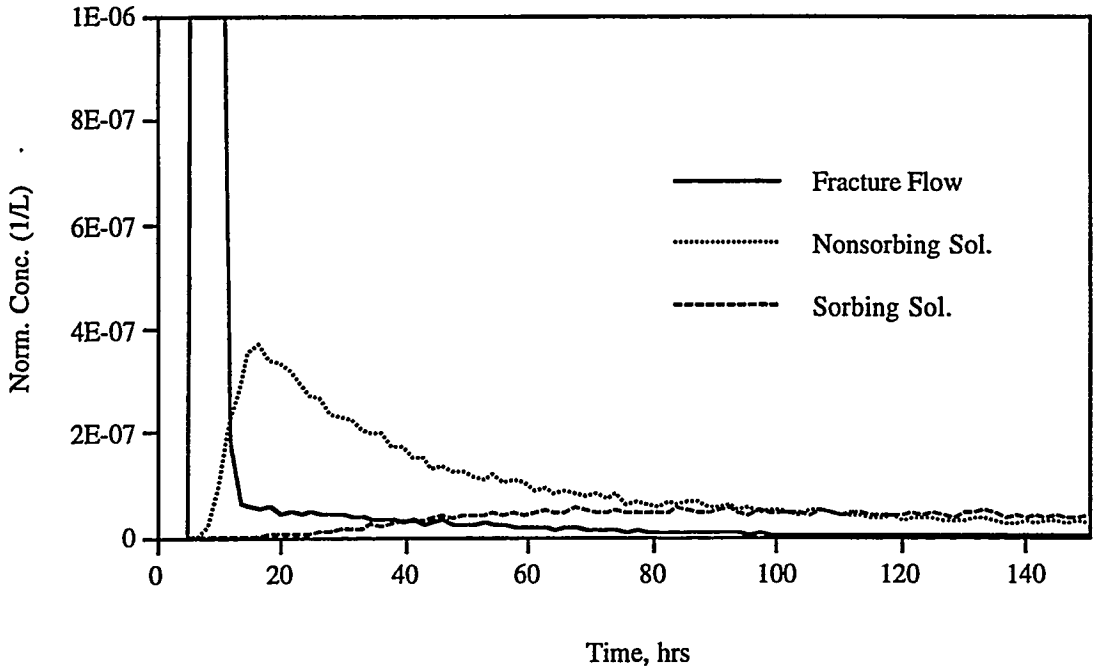

Fig. 24. Predicted breakthrough curves of each tracer resulting from a 120-gal injection of tracer solution into C#2 followed by a 2-hr chase of water at 20 gpm with a 200 gpm production rate out of C#3.

feature will undoubtedly be used to refine the mesh between the wells and in the immediate vicinity of the wells, where most of the flow and transport occurs. It is anticipated that different meshes will be necessary to simulate convergent flow and recirculating flow, as the domains of interest and the areas where pressure gradients are steepest are considerably different in these cases. If flow is considered to be confined in one or a few layers, the computations may be simplified by using 2-D grids instead of 3-D grids.

Tracer transport calculations can be conducted within the framework of FEHMN, as this code allows simulation of matrix diffusion and sorption in dual-porosity media, and it also includes a module for particle tracking. However, these features will have to be tested to ensure that they properly account for some of phenomena that occur in forced-gradient experiments in fractured media. For instance, when fracture flow rates are high, the model should allow solutes to move through fractured blocks with significantly less matrix diffusion than would be predicted by assuming intimate contact between the solute and fracture walls (this is the rationale for the criteria that N_{DL} be greater than 0.7 before matrix diffusion is considered in the particle-tracking models developed for this study — see Section 2.5). Also, the model must account for phenomena such as borehole storage effects and the effects of recirculation on breakthrough curves. Alternatively, it may be more effective to use FEHMN to calculate only flow fields, and then these flow fields can be used in modified versions of the particle-tracking models developed for this report to conduct tracer transport calculations.

6.0 CONCLUSIONS

The best approach to studying the effects of solute matrix diffusion and sorption at the C-Holes is to conduct multiple tracer tests at different flow rates in the same formation and between the same two wells. It is recommended that initial testing be conducted between C#2 and C#3, as tracer travel times are predicted to be much shorter with correspondingly greater tracer recoveries between these two wells than between C#1 and C#3, which are separated by over twice the distance. Subsequent testing could then investigate transport between C#1 and C#3 or in formations other than the one tested initially.

Conceptual models that account for solute matrix diffusion and sorption in fractured media can best be tested in interwell tracer tests by observing and interpreting the differences in (1) breakthrough curves of different tracers in the same test and (2)

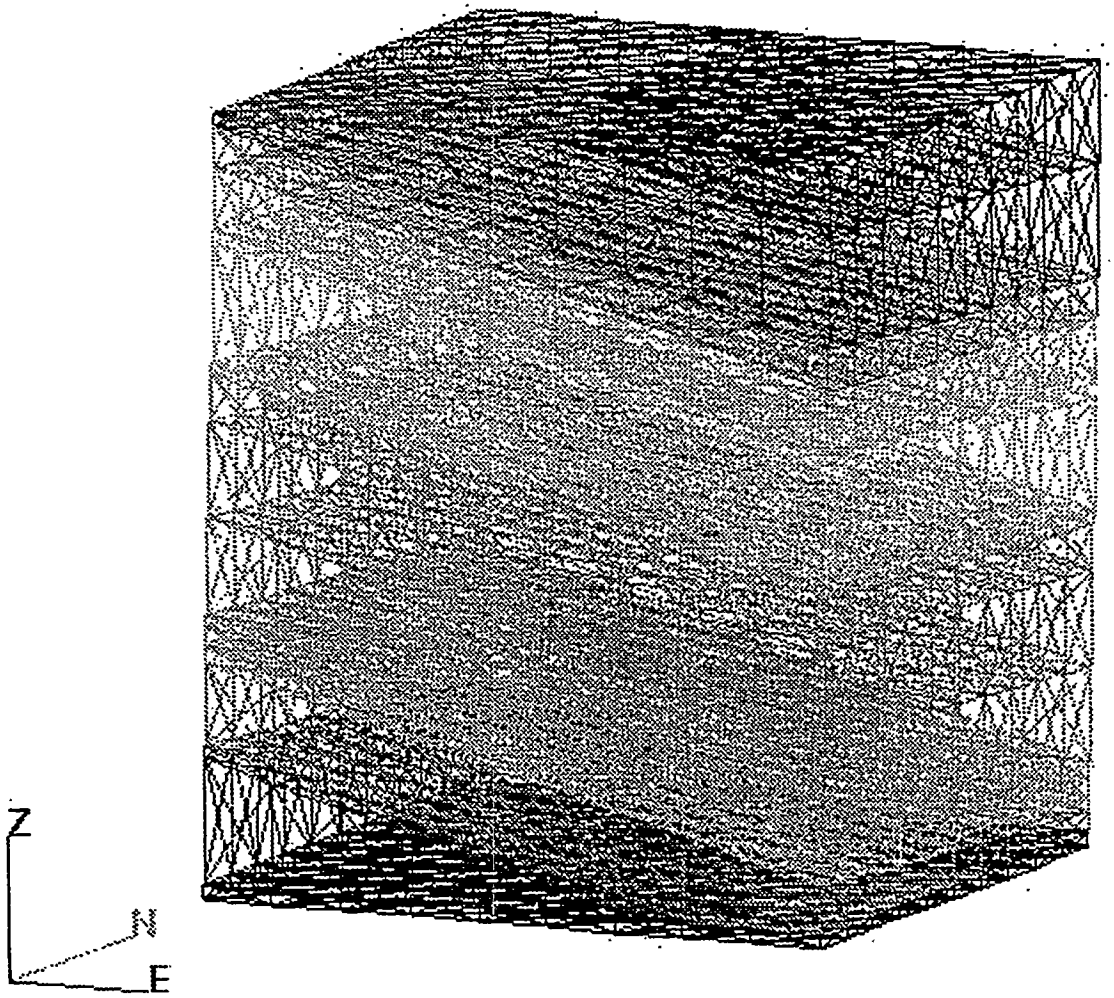

Fig. 25. Finite element grid of the saturated zone in the vicinity of the C-Holes. The layers correspond to the stratigraphy shown in Fig. 3 except that the dips of the planes defining contacts between layers have been averaged so that they all have the same slope.

breakthrough curves of the same tracers in tests at different flow rates. In order to ensure that differences in breakthrough curves from different tests can be attributed primarily to matrix diffusion and/or sorption, it is essential that all tests be conducted with a minimal amount of tracer holdup in the injection boreholes, and that tests at different flow rates be conducted in such a way that flow field dispersion (that is, dispersion due to flow streamlines of different lengths and velocities) is approximately the same in each test. These criteria can best be met by conducting fully-recirculating tests at different flow rates. However, practical considerations at the C-Holes (and in fully-recirculating tests, in general) suggest that it may be better to conduct convergent tracer tests at different flow rates, with the provision that tracer injection be followed by a water chase of at least two injection interval volumes to ensure that tracer is flushed out of the injection borehole. This provision is especially important at the C-Holes because of the large injection interval volumes relative to proposed tracer solution slug volumes.

7.0 REFERENCES

Bureau of Reclamation. 1993. "Final Completion Memorandum for the Saturated Zone Packer System," Yucca Mountain Site Characterization Project, SCP Activity 8.3.1.2.3.1.4. Prepared for the United States Geological Survey.

Drost, W. 1968. "Point Dilution Methods of Investigating Ground Water Flow by Means of Radioisotopes," Water Resour. Res. 4(1), 124-146.

Freeze, R. A. and Cherry, J. A. 1979. *Groundwater.* Prentice-Hall, Inc., Englewood Cliffs, NJ.

Fuentes, H. R., Polzer, W. L., Essington, E. H., and Newman, B. D. 1989. "Characterization of Reactive Tracers for C-Wells Field Experiments I: Electrostatic Sorption Mechanism, Lithium." LA-11691-MS, Los Alamos National Laboratory, Los Alamos, NM.

Gable, C.W., Cherry, T. A., Trease, H., and Zyvoloski, G. A. 1995. *GEOMESH User's Manual.* Prepared for YMP Milestone 4074, Los Alamos National Laboratory, Los Alamos, NM.

Geldon, A. L. 1993. "Preliminary Hydrogeologic Assessment of Boreholes UE-25c#1, UE-25c#2, and UE-25c#3, Yucca Mountain, Nye County, Nevada." Water-Resources Investigations Report 92-4016, United States Geological Survey, Denver CO.

Geldon, A. L. In Press. "Results and Interpretation of Preliminary Aquifer Tests in Boreholes UE-25c#1, UE-25c#2, and UE-25c#3, Yucca Mountain, Nye County, Nevada." Water-Resources Investigations Report 94-W-0412, United States Geological Survey, Denver CO.

Happel, J. and Brenner, H. 1965. Low Reynolds Number Hydrodynamics with Special Applications to Particulate Media, Appendix A. Prentice-Hall, Inc., Englewood Cliffs, NJ.

Kinzelbach, W. 1987. "The Random Walk Method in Pollutant Transport Simulation," in Groundwater Flow and Quality Modeling, E. Custodio, A. Gurgui, and J. P. Lobo Ferriera, eds., D. Riedel, Dordrecht, The Netherlands, pp. 227-245.

Krolikowski, C. 1965. "The Influence of Measuring Probes on the Examination of the Filtration Rate of Underground Waters in Bore Holes and Piezometers," Atomkernenergie **10**(1/2), 57-61.

Levenspiel, O. 1972. *Chemical Reaction Engineering*, 2nd ed. John Wiley and Sons, New York, NY.

Los Alamos National Laboratory (LANL). 1989." Study Plan for Testing of the C-Hole Sites with Reactive Tracers." LANL-SP-8.3.1.2.3.1.7, R2, Los Alamos National Laboratory, Los Alamos, NM.

Moreno, L. and Neretnieks, I. 1993. "Flow and Nuclide Transport in Fractured Media: The Importance of the Flow-Wetted Surface for Radionuclide Migration," J. Contam. Hydrol. **13**, 49-71.

Office of Civilian Radioactive Waste Management. 1988. *Site Characterization Plan,* Yucca Mountain Site, Nevada Research and Development Area, Nevada. Department of Energy Report DOE/RW-0199.

Reimus, P.W. 1995. Los Alamos National Laboratory. Unpublished results.

Reimus, P. W. 1995. "The Use of Synthetic Colloids in Tracer Transport Experiments in Saturated Rock Fractures." LA-13004-T (PhD Dissertation), Los Alamos National Laboratory, Los Alamos, NM.

Robinson, B. A. and Tester, J. 1984. "Dispersed Fluid Flow in Fractured Reservoirs: An Analysis of Tracer Determined Residence Time Distributions," J. Geophys. Res. **89**(B12), 10374-10384.

Robinson, B. A., et al. In Press. "YMP Milestone Report" (Milestone 3249). Los Alamos National Laboratory, Los Alamos, NM.

Starr, R. C. Gillham, R. W., and Sudicky, E. A. 1985. "Experimental Investigation of Solute Transport in Stratified Porous Media 2. The Reactive Case," Water Resour. Res. **21**(7), 1043-1050.

Steinkamp, J. A., Habbersett, R. C., and Hiebert, R. D. 1991. "Improved Multilaser/ Multiparameter Flow Cytometer for Analysis and Sorting of Cells and Particles," Rev. Sci. Instrum. **62**(11), 2751-2764.

Stensrud, Wayne. 1995. INTERA. Personal communication.

Tompson, A. F. B., Vomvoris, E. G., and Gelhar, L. W. 1987. "Numerical Simulation of Solute Transport in Randomly Heterogeneous Porous Media: Motivation, Model

Development, and Application." UCID-21281, Lawrence Livermore National Laboratory, Livermore, CA.

Tompson, A. F. B. and Gelhar, L. W. 1990. "Numerical Simulation of Solute Transport in Three-Dimensional, Randomly Heterogeneous Porous Media," Water Resour. Res. **26**(10), 2541-2562.

United States Geological Survey (USGS). 1990. "Characterization of the Site Saturated-Zone Ground-Water Flow System." Study Plan 8.3.1.2.3.1-6, United States Geological Survey, Denver, CO.

Zyvoloski, G.A., Robinson, B. A., Dash, Z.V., and Trease, L. L. 1995a. "Models and Methods Summary for the FEHMN Application." LA-UR-94-3787, Rev. 1., Los Alamos National Laboratory, Los Alamos, NM.

Zyvoloski, G.A., Robinson, B. A., Dash, Z.V., and Trease, L. L. 1995b. *Users Manual for the FEHMN Application.* LA-UR-94-3788, Rev. 1., Los Alamos National Laboratory, Los Alamos, NM.

Appendix A: 3-D Flow Fields to/from a Vertical Well in Homogeneous, Isotropic Media

The natural coordinate system to use to describe flow to/from a packed-off interval in vertical well in 3-dimensional, homogeneous, isotropic media is prolate spheroidal coordinates, which is a conjugate coordinate system of revolution about the z-axis (see Fig. 8 and Happel and Brenner 1965, Appendix A). This (ξ, η, ϕ) coordinate system, where $0 \le \xi < \infty$, $0 \le \eta \le \pi$, and $0 \le \phi < 2\pi$ and $0 \le \phi < 2\pi$, is defined by the following coordinate transformations:

$$z = c \cosh\xi \cos\eta \tag{A.1}$$

$$\rho = \sqrt{x^2 + y^2} = c \sinh\xi \sin\eta \tag{A.2}$$

$$x = \rho \cos\phi \tag{A.3}$$

$$y = \rho \sin\phi \tag{A.4}$$

where, c = half-length of injection/production zone (see Fig. 8).
x, y, z are the cartesian coordinates.

It can be shown that the inverse transformation is given by:

$$a = \sinh\xi = \sqrt{\frac{z^2 + \rho^2 - c^2 + \sqrt{\left(z^2 + \rho^2 - c^2\right)^2 + 4\rho^2 c^2}}{2c^2}} \tag{A.5}$$

$$\xi = \ln\left(a + \sqrt{a^2 + 1}\right) \tag{A.6}$$

$$h = \cos^{-1}\left(\sqrt{\frac{z^2 + \rho^2 + c^2 - \sqrt{\left(z^2 + \rho^2 + c^2\right)^2 - 4z^2 c^2}}{2c^2}}\right) \tag{A.7}$$

$$\phi = \mathrm{Tan}^{-1}\left(\frac{y}{x}\right) \tag{A.8}$$

The reason that the prolate spheroidal coordinate system is "natural" for 3-D flow to/from a well is that flow will always be directed in the ξ-direction. The analogy in 2-dimensions is that flow is always directed in the radial direction. Flow velocities in 2-D are inversely proportional to the radial distance, r, from the well (or, more specifically, to the circumference of a circle with radius r), so, by analogy, flow velocities in 3-D are inversely proportional to the surface area of the prolate spheroidal surface of constant ξ. The ξ-directed velocity, $v_\xi(\xi)$, at any ξ is given by

$$v_\xi(\xi) = \frac{Q \cdot (\text{surface area of wellbore})}{(\text{surface area of prolate spheroid of constant } \xi)} \tag{A.9}$$

where, Q = volumetric flow rate into/out of well.

Because the cylindrical wellbore is not a surface of constant , it is convenient to determine the value of that results in a surface that has the same surface area as the wellbore. Mathematically, the equating of surface areas is stated as

$$2c \cdot 2\pi r = 2\int_0^c 2\pi \left[\rho_{\xi_o}(z)\right] dz \tag{A.10}$$

Using equation (A.2) for ρz, and differentiating equation (A.1) with respect to η, we can change the variable of integration in (A.10) from z to η:

$$2c \cdot 2\pi r = -2 \int_{\frac{\pi}{2}}^{\eta_o} 2\pi c^2 \sinh\xi_o \cosh\xi_o \sin^2\eta \, d\eta \tag{A.11}$$

or

$$2c \cdot 2\pi r = -4\pi c^2 \sinh\xi_o \cosh\xi_o \left[\frac{\eta}{2} - \frac{\sin(2\eta)}{4}\right]_{\frac{\pi}{2}}^{\eta_o} \tag{A.12}$$

where, $\eta_o = \eta(z = c, \rho \approx r)$

If c is large relative to the well radius r (as it almost always will be), then, $\eta_o \approx 0$, $\xi_o \approx 0$, and $\cosh \xi_o \approx 1$. Equation (A.12) then becomes

$$\sinh\xi_o = \frac{4r}{\pi c} \tag{A.13}$$

ξ_o can be solved using equation (A.6) with $a = \frac{4r}{\pi c}$.

If we integrate equation (A.11) between $\eta = \pi/2$ and $\eta = 0$ at two different values of ξ, we see that the ratio of the surface areas of two different surfaces of constant ξ is given by

$$\text{surface area ratio} = \frac{\sinh\xi_1 \cosh\xi_1}{\sinh\xi_2 \cosh\xi_2} \tag{A.14}$$

Using equations (A.9) and (A.14), we can now determine $v_\xi(\xi)$ as a function of ξ:

$$v_\xi(\xi) = \left(\frac{Q}{4\pi c\varepsilon r}\right)\frac{\sinh\xi_o \cosh\xi_o}{\sinh\xi \cosh\xi} \tag{A.15}$$

where, ε = porosity of formation (fracture porosity in dual-porosity medium).

Using this methodology, the wellbore is approximated as a cigar-shaped region of constant $\xi = \xi_o$, where ξ_o is small.

Because we are interested in the superposition of flow fields from two different wells, it is necessary to convert the velocity in the natural coordinate system to velocity components in a common coordinate system, which, for convenience, is chosen to be cartesian coordinates. The velocity components in the - and z-directions are given by

$$v\rho = v_\xi h_\xi \frac{\partial\rho}{\partial\xi} = v_\xi h_\xi \, c \cosh\xi \sin\eta \tag{A.16}$$

$$v_z = v_\xi \, h_\xi \, \frac{\partial z}{\partial\xi} = v_\xi \, h_\xi \, c \sinh\xi \cos\eta \tag{A.17}$$

where, $h_\xi = \dfrac{\sqrt{2}}{c\sqrt{\cosh 2\xi + \sin 2\eta}}$ = a metrical coefficient defined by Happel and Brenner (1965).

The x- and y-velocity components are then given by

$$v_x = v_\rho \cos\phi \tag{A.18}$$

$$v_y = v_\rho \sin\phi \tag{A.19}$$

Thus, the procedure for determining the x-, y-, and z-velocity components at any arbitrary location (x, y, z) in 3-dimensions can be summarized as follows:

(1) Use equations (A.2), (A.5), (A.6), and (A.7) to determine ξ and η in the natural coordinate system for one well.
(2) Use equation (A.15) to determine $v_\xi(\xi)$.
(3) Use equations (A.16) to (A.19) to determine v_x,v_y, and v_z.
(4) Repeat steps 1-3 for the second well.
(5) Sum the x-, y-, and z-velocity components from each well (and the natural velocity vector components as well) to get the resulting v_x,v_y, and v_z.

Appendix B: 2-D Flow Field Distortion Near a Borehole

In pure potential flow, the potential distribution must satisfy the Laplace equation. In 2-D cylindrical coordinates, the Laplace equation can be written as (Krolikowski 1965):

$$\frac{\partial^2 U}{\partial r^2} + \frac{\partial U}{r\partial r} + \frac{\partial^2 U}{r^2 \partial \theta^2} = 0 \qquad \text{(B.1)}$$

where, U = potential.

If the potential field, U, is known, the velocity components are determined from

$$v_r = -K\frac{\partial U}{\partial r} \qquad \text{(B.2)}$$

$$rv_\theta = -K\frac{\partial U}{r\partial \theta} \qquad \text{(B.3)}$$

where, K = hydraulic conductivity.

Krolikowski (1965) has shown that the general solution of equation (B.1) has the form:

$$U = A\,r\cos\theta + B\,\frac{\cos\theta}{r} \qquad \text{(B.4)}$$

where, A, B = integration constants.

We now define two regions of interest: the formation (region 1) and the borehole (region 2). The general solution holds for both regions, so

$$U_1 = A_1\,r\cos\theta + B_1\,\frac{\cos\theta}{r} \qquad \text{(B.5)}$$

$$U_2 = A_2\,r\cos\theta + B_2\,\frac{\cos\theta}{r} \qquad \text{(B.6)}$$

Referring to Fig. B.1, we define the following terms:

$$r = \sqrt{(x - R_o)^2 + y^2}\,,$$

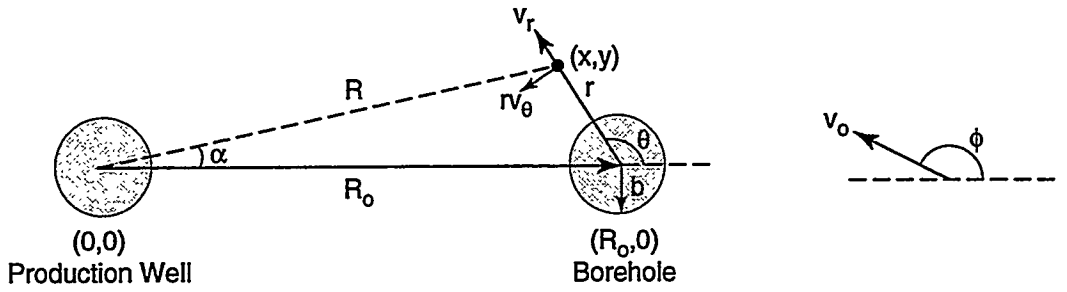

Figure B.1. Illustration of terms used to solve for flow field distortion around a borehole.

$R = \sqrt{x^2 + y^2}$,
b = radius of borehole,
R_o = distance from production well to borehole,

$$\alpha = \text{Tan}^{-1}\left(\frac{y}{x}\right),$$

$$\theta = \text{Tan}^{-1}\left(\frac{y}{(x - R_o)}\right),$$

v_o = ambient flow velocity vector,
ϕ = angle between ambient velocity vector and positive x-axis,
v_o = radial velocity in (r,) coordinate system,
v_θ = angular velocity in (r,) coordinate system.

After a considerable amount of trigonometry, it can be shown that the undistorted radial velocity, $v_{r\infty}$, in the cylindrical coordinate system defined by (r,θ) [i.e., with origin at (R_o,0)] is given by

$$v_{r\infty} = -q(R)\cos(\pi - \theta + \alpha) + v_o \cos(\theta - \phi) \qquad \text{(B7)}$$

where, $q(R) = \dfrac{-Q}{4\pi c \eta R}$

Q = volumetric flow rate out of production well,
c = half-length of production interval,
η = effective porosity of formation.

Similarly, the undistorted angular velocity in the (r, θ) coordinate system is given by

$$(r\, v_\theta)_\infty = -q(R)\sin(\pi - \theta + \alpha) - v_o \sin(\theta - \phi) \qquad \text{(B.8)}$$

The integration constants in equations (B.5) and (B.6) are found by applying the following boundary conditions:

$$v_r = v_{r\infty} \text{ as } r \rightarrow \infty \tag{B.9}$$

$$v_r = \text{finite at } r = 0 \tag{B.10}$$

$$U_1 = U_2 \text{ at } r = b \tag{B.11}$$

$$K_1 \frac{\partial U_1}{\partial r} = K_2 \frac{\partial U_2}{\partial r} \text{ at } r = b \tag{B.12}$$

This procedure leads to the following values of the integration constants:

$$A_1 = \frac{-v_{r\infty}}{K_1 \cos\theta} \tag{B.13}$$

$$B_1 = \frac{\left(\frac{K_2}{K_1} - 1\right) b^2 v_{r\infty}}{(K_1 + K_2)\cos\theta} \tag{B.14}$$

$$A_2 = \frac{-v_{r\infty}}{K_1 \cos\theta} + \frac{\left(\frac{K_2}{K_1} - 1\right) v_{r\infty}}{(K_1 + K_2)\cos\theta} \tag{B.15}$$

$$B_2 = 0 \tag{B.16}$$

Substituting equations (B.5) and (B.13) through (B.16) into equations (B.2) and (B.3) leads to the following expressions for the distorted velocity components in the formation (region 1):

$$v_r = v_{r\infty}\left(1 + \frac{K_1\left(\frac{K_2}{K_1} - 1\right)b^2}{(K_1 + K_2) r^2}\right) \tag{B.17}$$

$$rv_\theta = (r\,v_\theta)_\infty \left(1 - \frac{K_1\left(\frac{K_2}{K_1} - 1\right)b^2}{(K_1 + K_2)\,r^2} \right) \tag{B.18}$$

Equations (B.17) and (B.18) can be qualitatively verified by noting that they reduce to equations (B.7) and (B.8) when $K_1 = K_2$. Also, $v_r = 2v_{r\infty}$ and $rv_\theta = 0$ when $K_2 >> K_1$ and $r = b$. This result is in agreement with Krolikowski's (1965) result for the special case of $q(R) = 0$.

The velocity components in cartesian coordinates are given by

$$v_x = v_r \cos\theta - rv_\theta \sin\theta \tag{B.19}$$

$$v_y = v_r \sin\theta + rv_\theta \cos\theta \tag{B.20}$$

Any radial flow out of the borehole as a result of injection into the hole can be added linearly to these components without correcting for distortion because there is no distortion in pure outward radial flow.

Appendix C: Simulated Breakthrough Curves

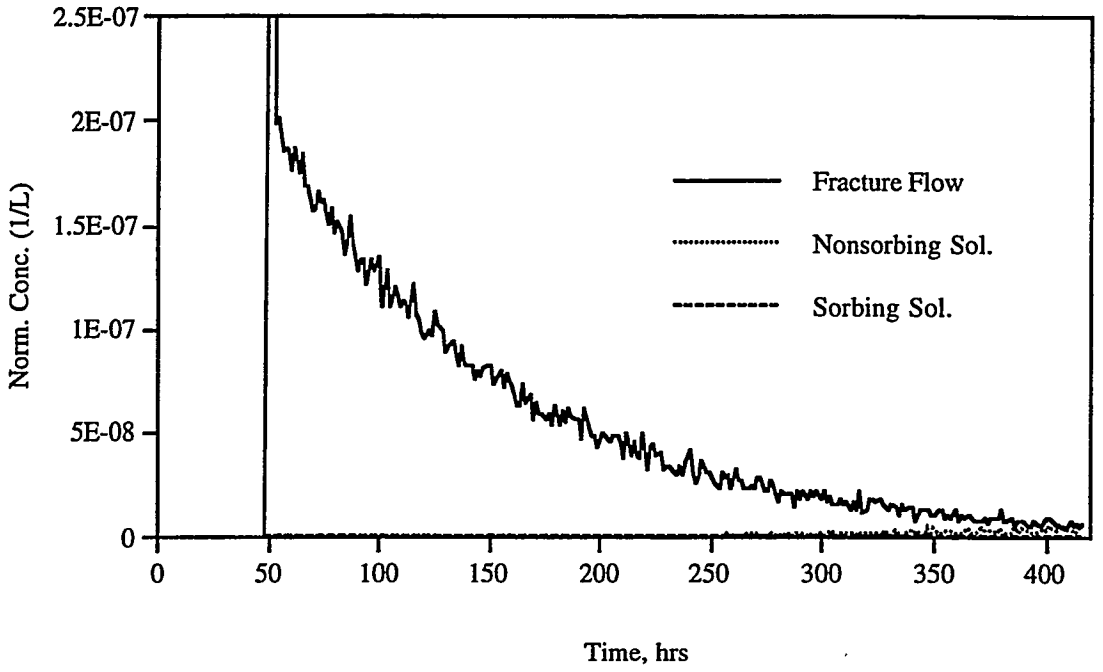

Figure C.1. Breakthrough curves for 20 gpm injection into C#1 for 6 min. with 200 gpm production out of C#3. No chase or recirculation. Base case parameter values. Fracture flow peak is at 4.7 X 10^{-7}/L.

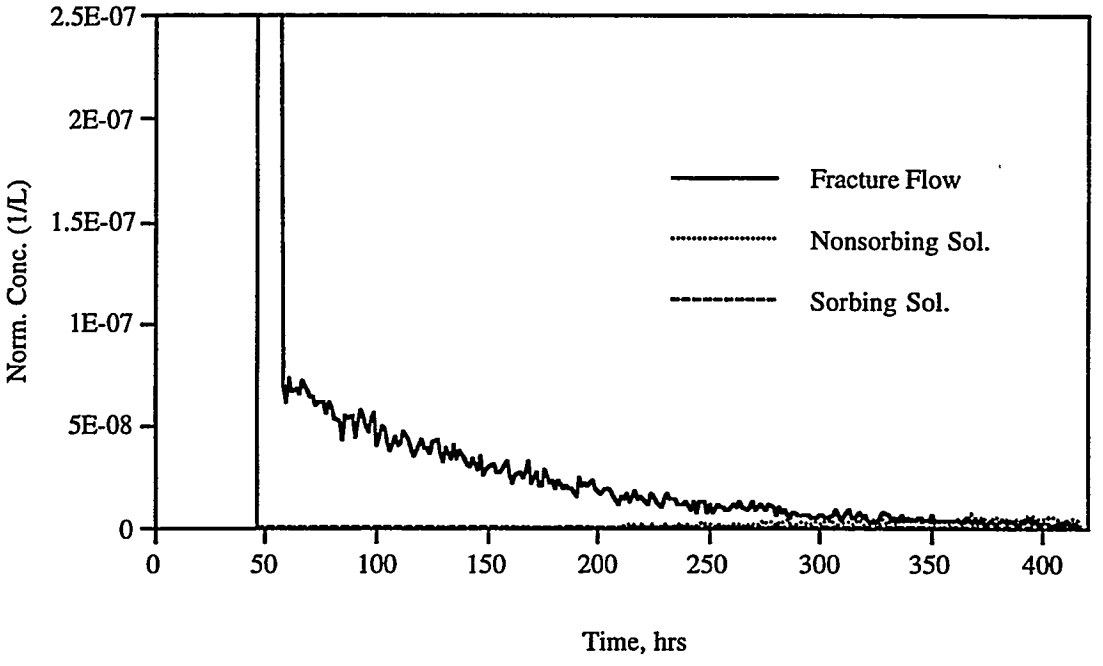

Figure C.2. Breakthrough curves for 20 gpm injection into C#1 for 6 min. followed by 20 gpm chase for 1 hr. with 200 gpm production out of C#3. No recirculation. Base case parameter values. Fracture flow peak is at 1.8 X 10^{-6}/L.

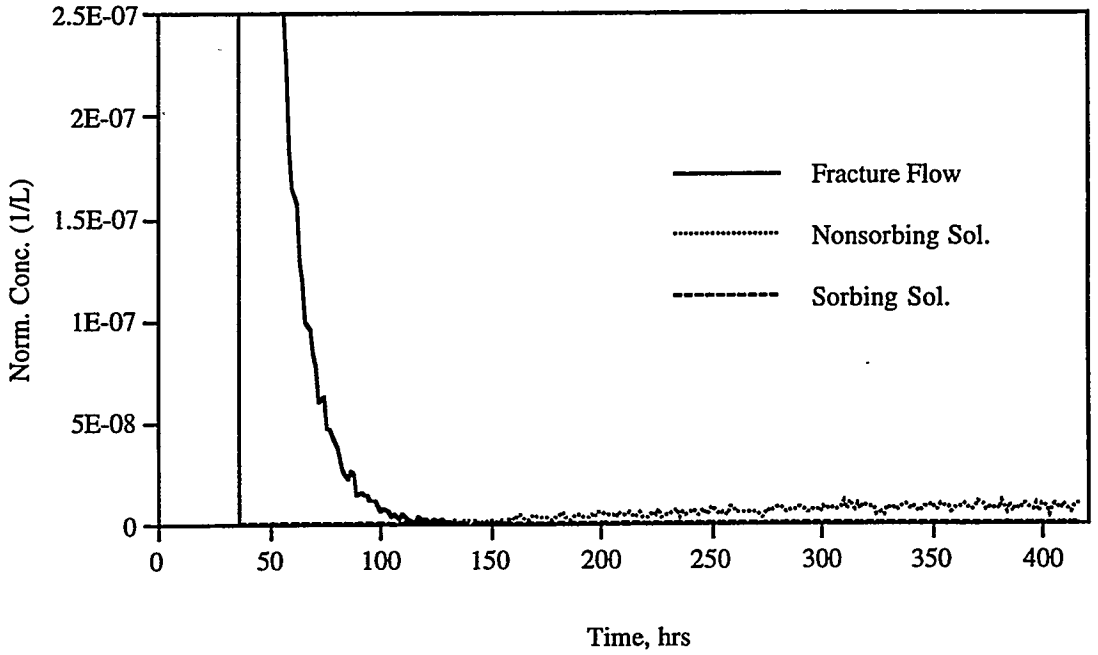

Figure C.3. Breakthrough curves for 20 gpm injection into C#1 for 6 min. followed by 20 gpm recirculation with 200 gpm production out of C#3. Base case parameter values. Fracture flow peak is at 2.7 X 10^{-6}/L.

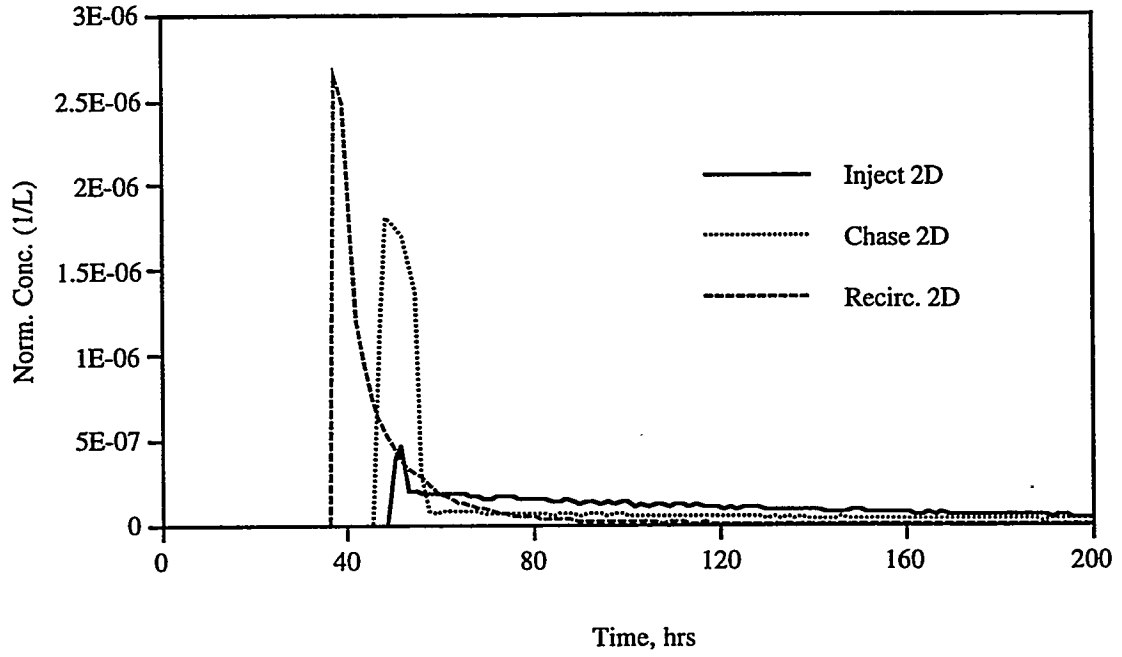

Figure C.4. Breakthrough curves of fracture-flow-only tracer between C#1 and C#3 for each of the three different injection/production strategies of Figs. C.1 to C.3.

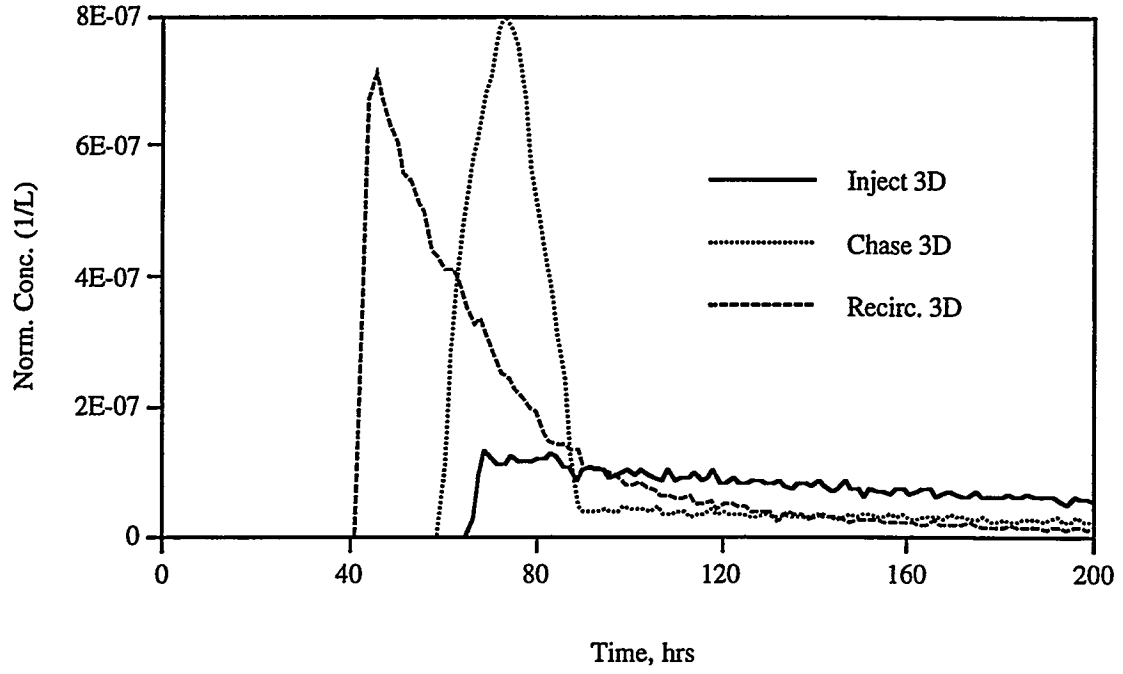

Figure C.5. Breakthrough curves of fracture-flow-only tracer between C#1 and C#3 for each of the three different injection/production strategies of Figs. C.1 to C.3 using the 3-D particle-tracking model.

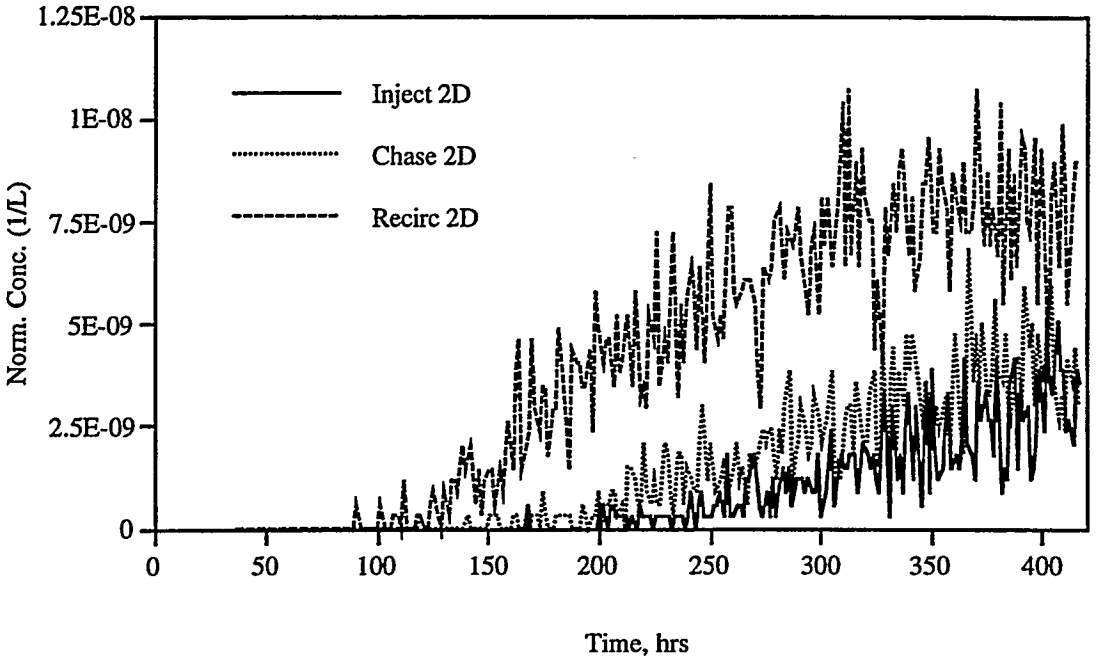

Figure C.6. Breakthrough curves of nonsorbing tracer between C#1 and C#3 for each of the three different injection/production strategies of Figs. C.1 to C.3.

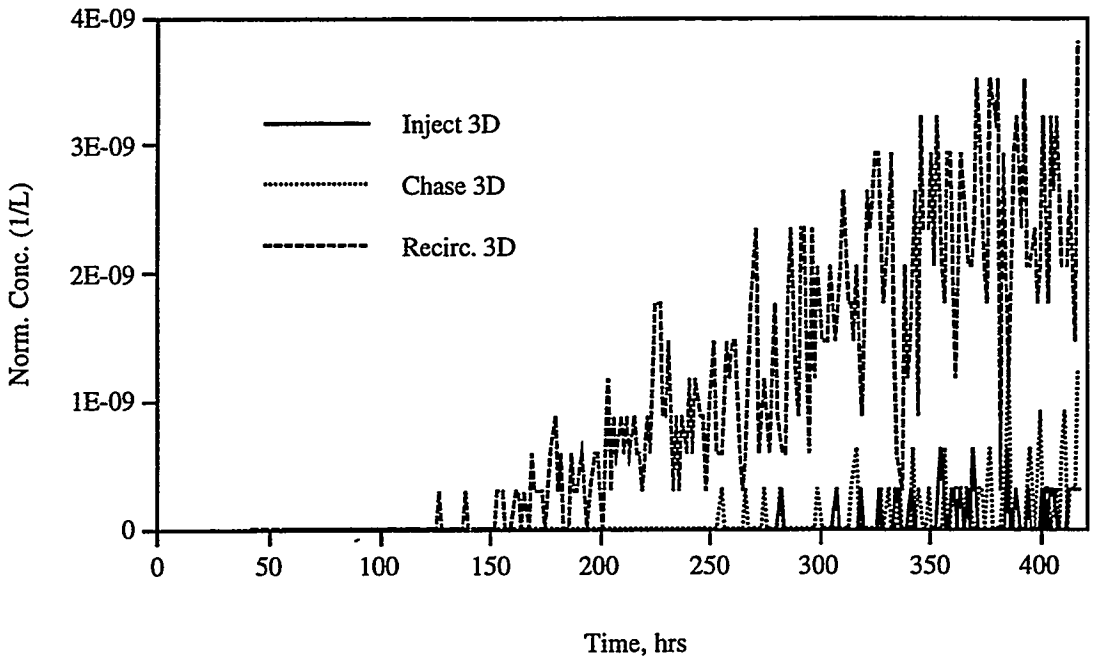

Figure C.7. Breakthrough curves of nonsorbing tracer between C#1 and C#3 for each of the three different injection/production strategies of Figs. C.1 to C.3 using the 3-D particle-tracking model.

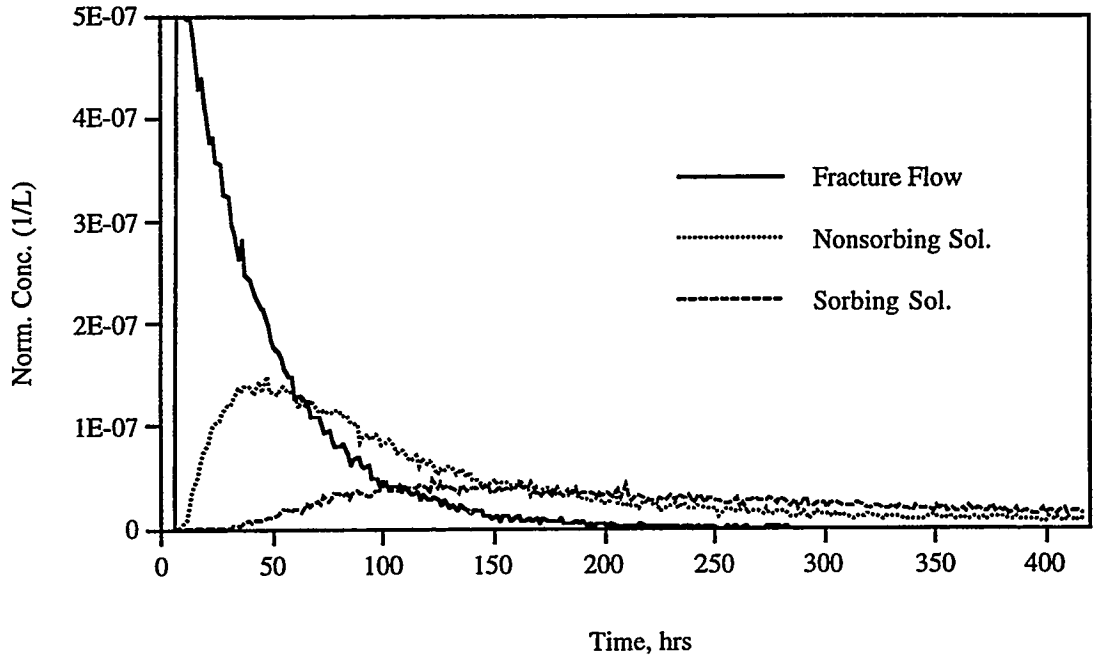

Figure C.8. Breakthrough curves for 20 gpm injection into C#2 for 6 min. with 200 gpm production out of C#3. Base case parameter values. Fracture flow peak is at 9.5 X 10^{-7}/L.

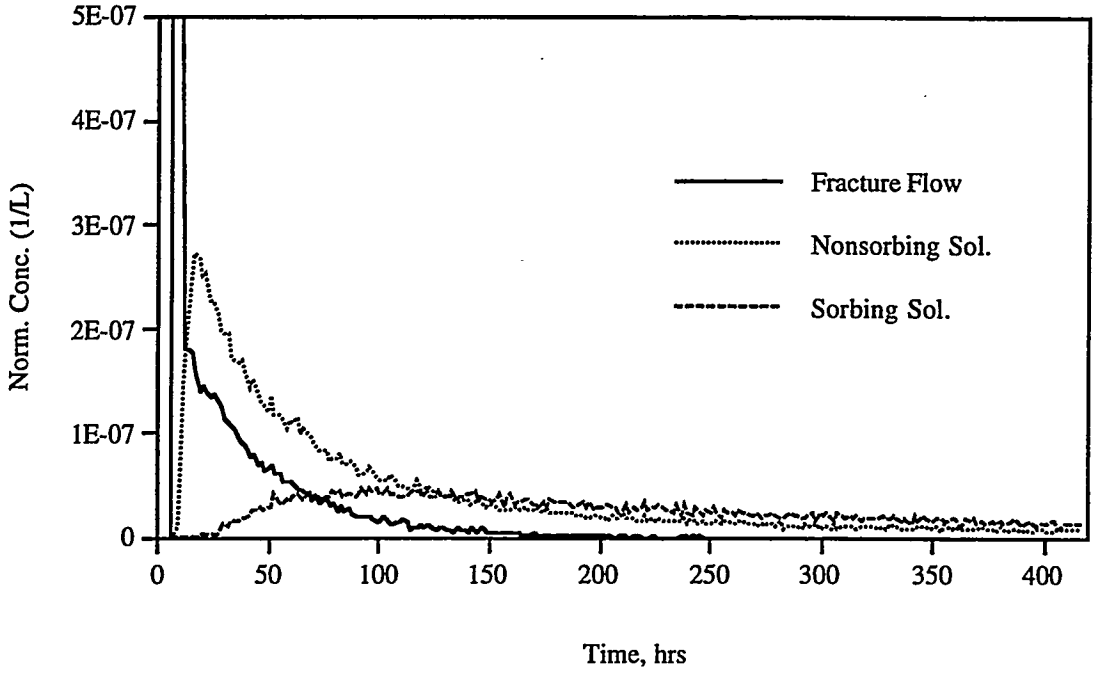

Figure C.9. Breakthrough curves for 20 gpm injection into C#2 for 6 min. followed by 20 gpm chase for 1 hr. with 200 gpm production out of C#3. Base case parameter values. Fracture flow peak is at 4.7 X 10^{-6}/L.

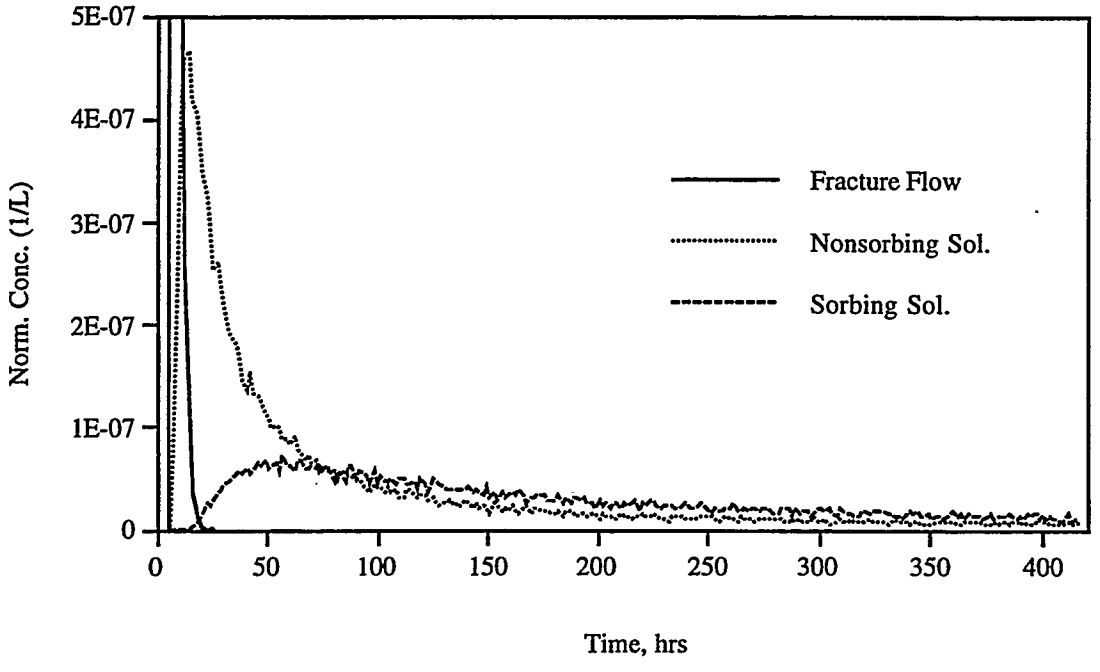

Figure C.10. Breakthrough curves for 20 gpm injection into C#2 for 6 min. followed by 20 gpm recirculation with 200 gpm production out of C#3. Base case parameter values. Fracture flow peak is at 6.6 X 10^{-6}/L.

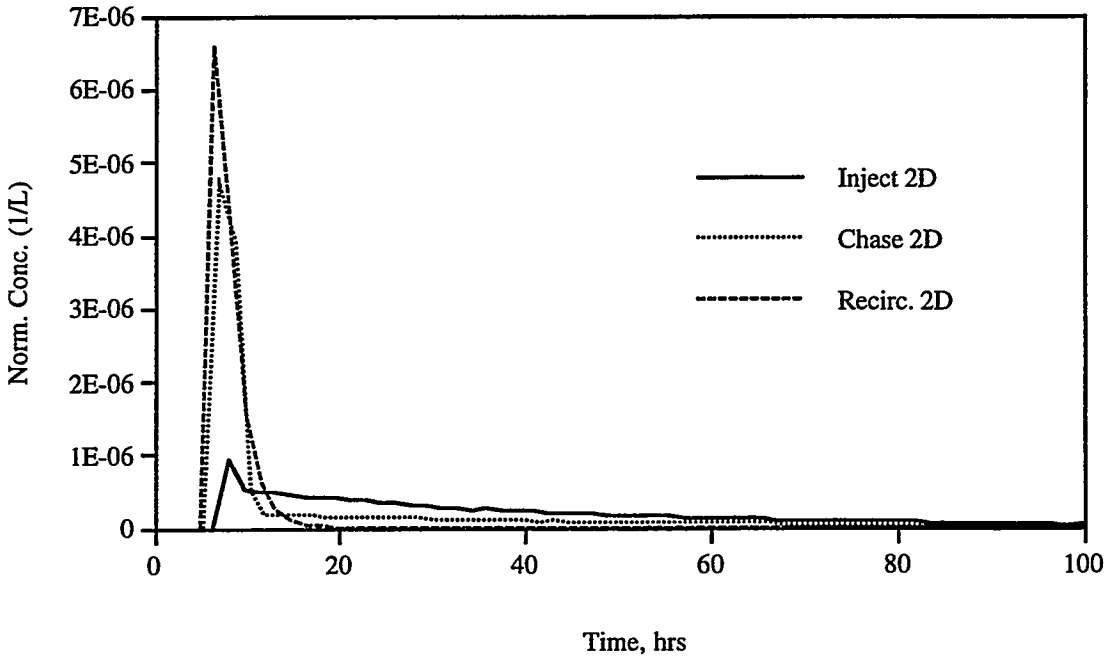

Figure C.11. Breakthrough curves of fracture-flow-only tracer between C#2 and C#3 for each of the three different injection/production strategies of Figs. C.8 to C.10.

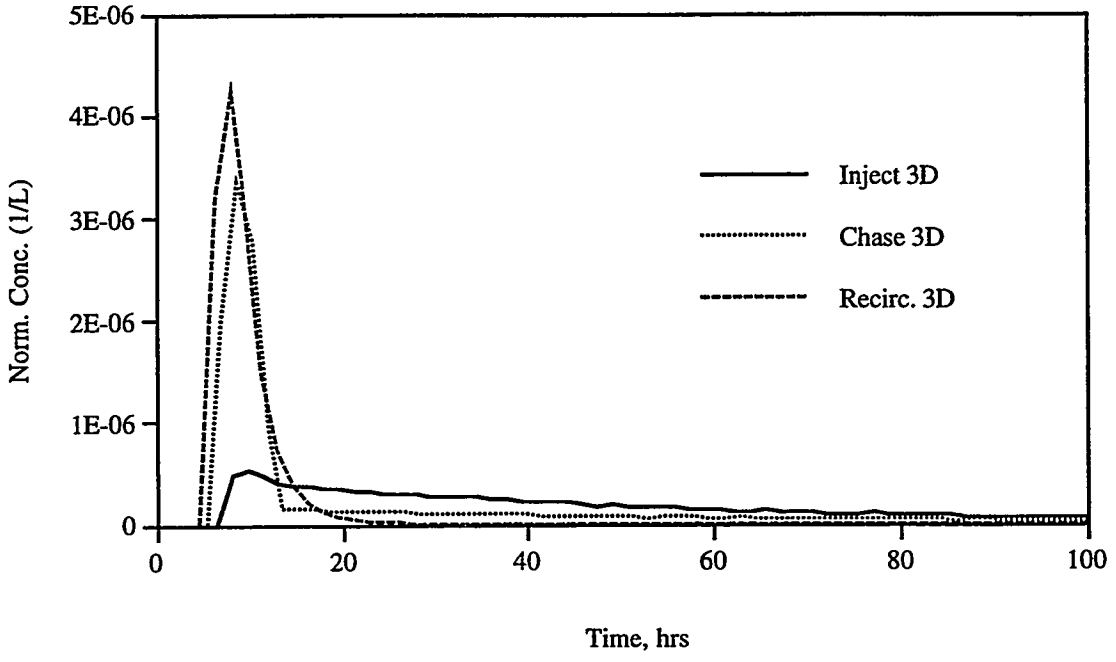

Figure C.12. Breakthrough curves of fracture-flow-only tracer between C#2 and C#3 for each of the three different injection/production strategies of Figs. C.8 to C.10 using the 3-D particle-tracking model.

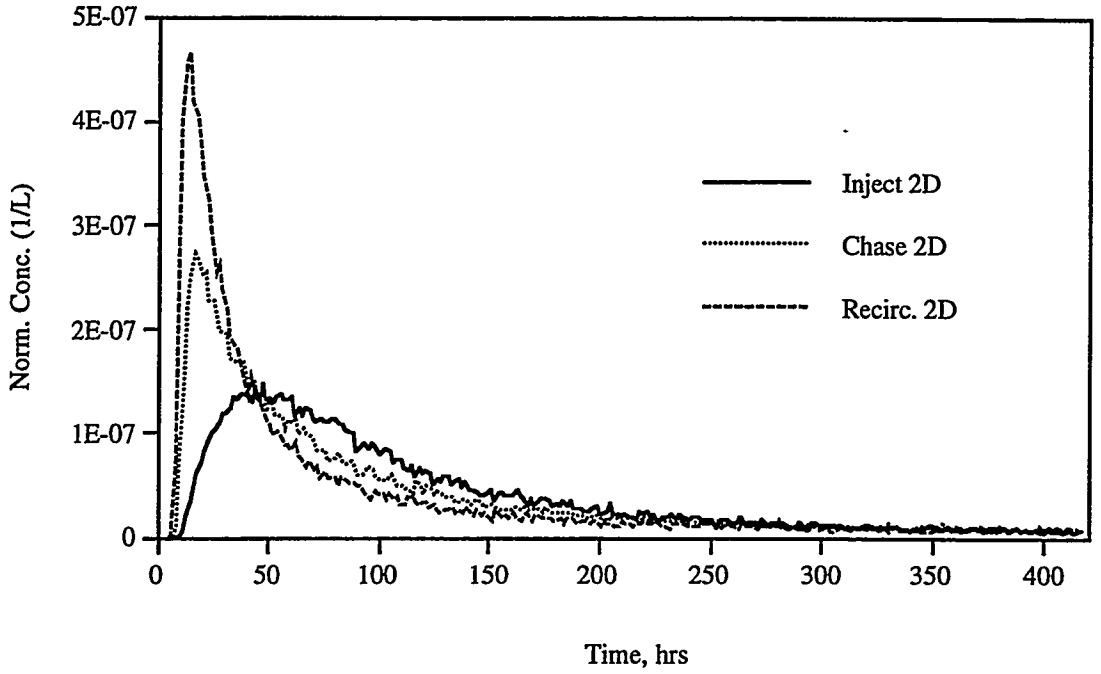

Figure C.13. Breakthrough curves of nonsorbing tracer between C#2 and C#3 for each of the three different injection/production strategies of Figs. C.8 to C.10.

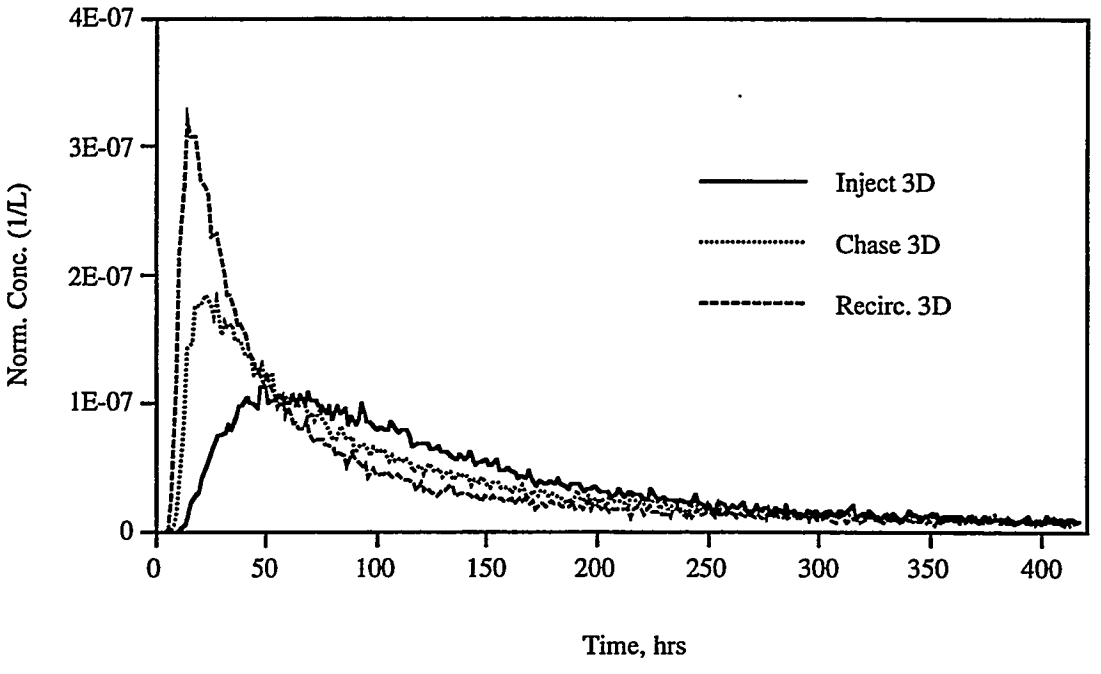

Figure C.14. Breakthrough curves of nonsorbing tracer between C#2 and C#3 for each of the three different injection/production strategies of Figs. C.8 to C.10 using the 3-D particle-tracking model.

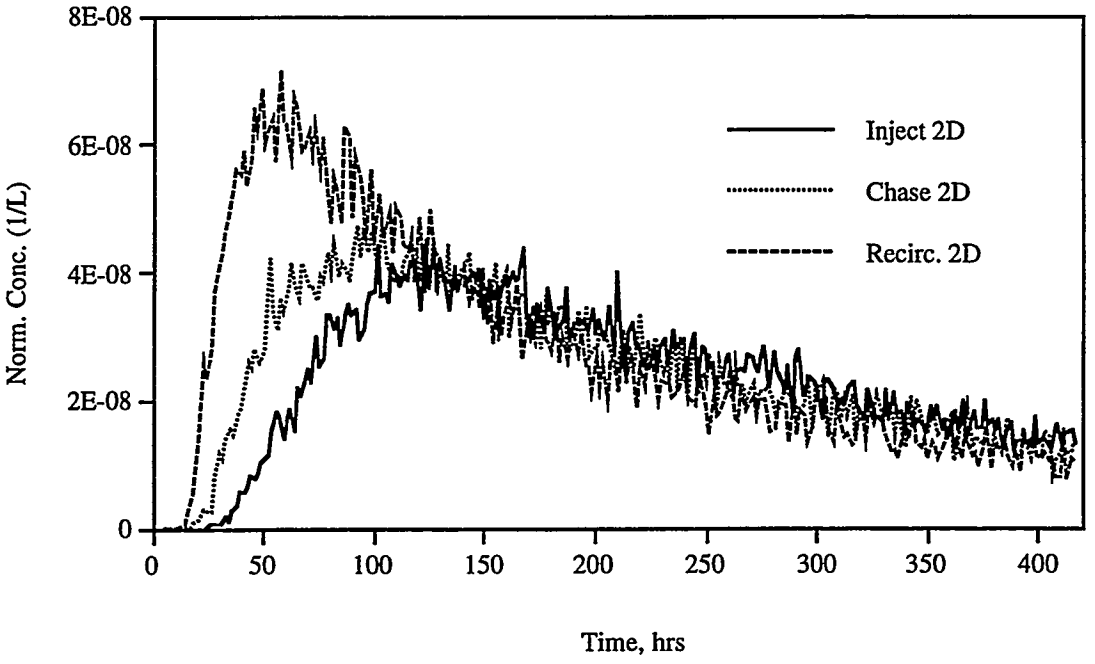

Figure C.15. Breakthrough curves of sorbing tracer between C#2 and C#3 for each of the three different injection/production strategies of Figs. C.8 to C.10.

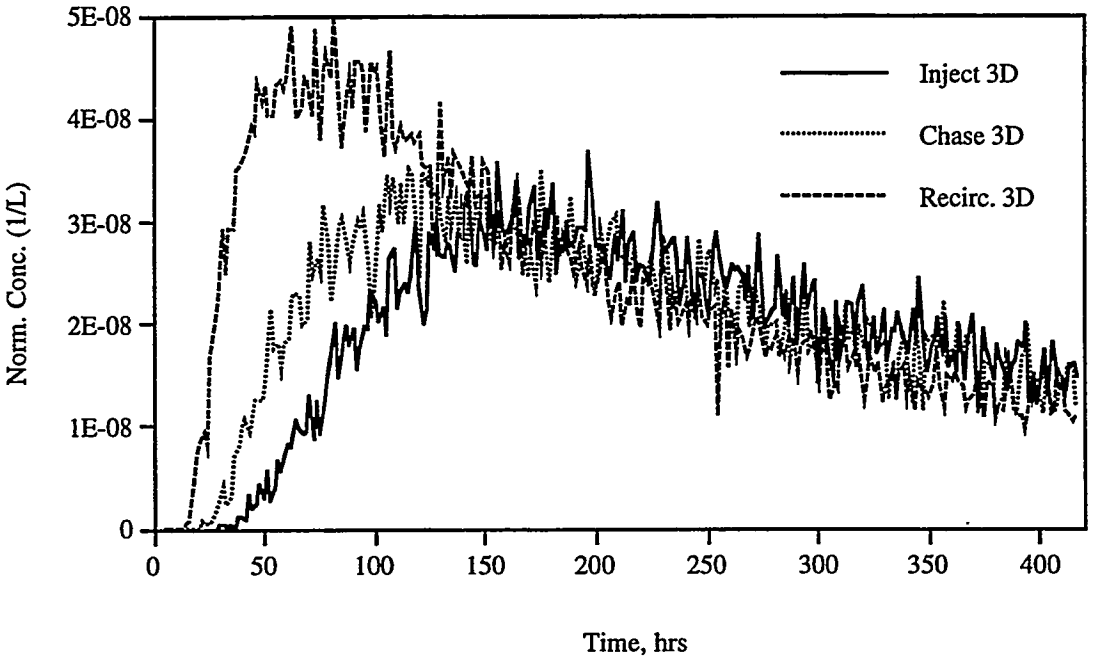

Figure C.16. Breakthrough curves of sorbing tracer between C#2 and C#3 for each of the three different injection/production strategies of Figs. C.8 to C.10 using the 3-D particle-tracking model.

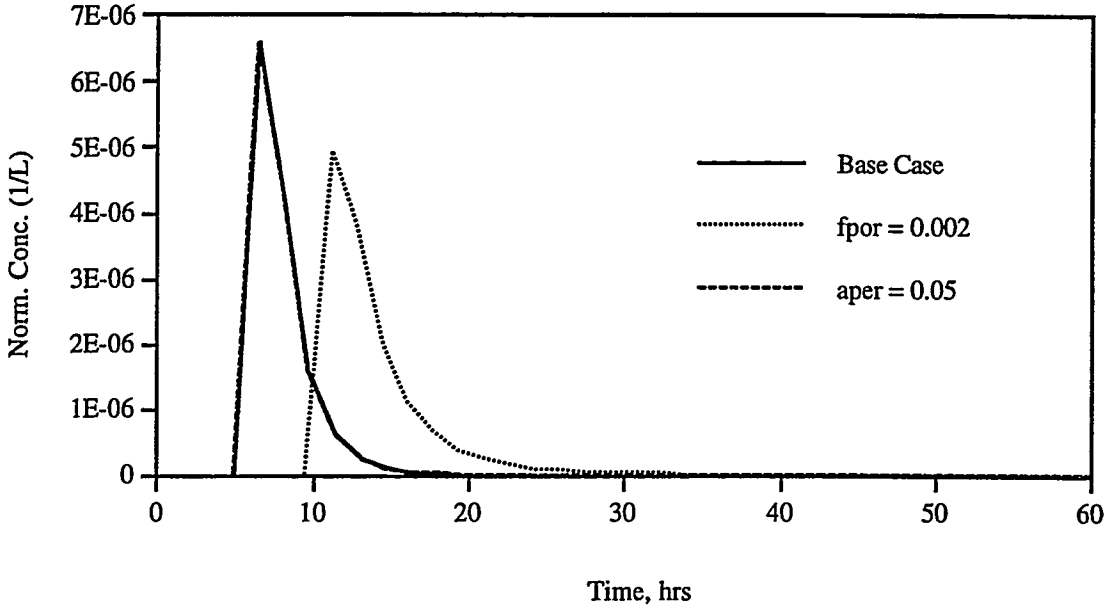

Figure C.17. Breakthrough curves of fracture-flow-only tracer between C#2 and C#3 with 200 gpm production and 20 gpm recirculation. "fpor = 0.002" denotes fracture porosity of 0.002 (base case value is 0.001), and "aper = 0.05" denotes average fracture aperture of 0.05 cm (base case value is 0.02 cm).

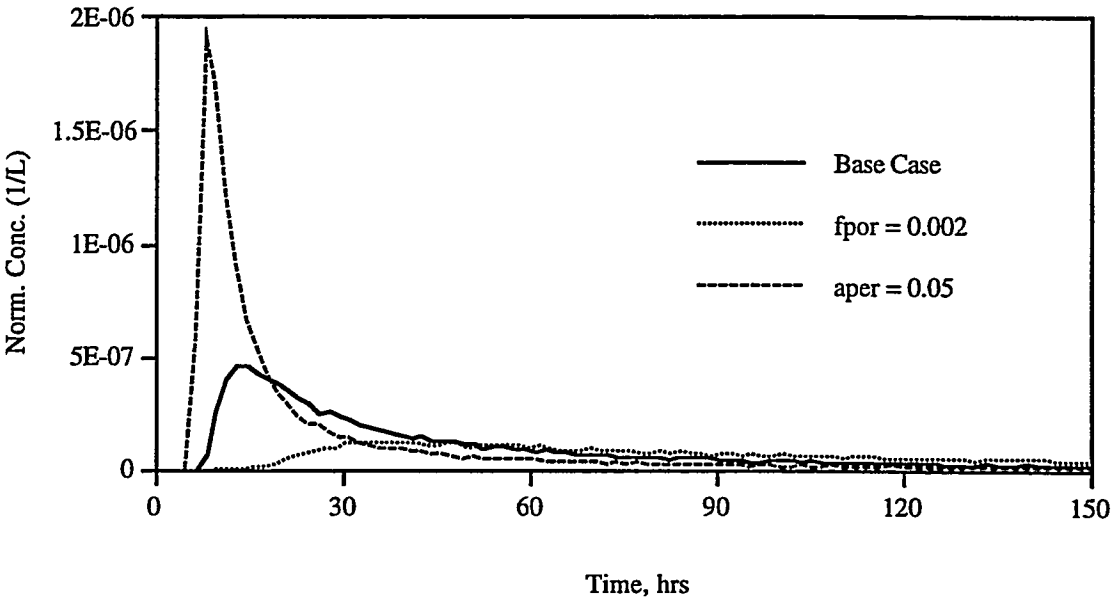

Figure C.18. Breakthrough curves of nonsorbing tracer between C#2 and C#3 with 200 gpm production and 20 gpm recirculation. "fpor = 0.002" denotes fracture porosity of 0.002 (base case value is 0.001), and "aper = 0.05" denotes average fracture aperture of 0.05 cm (base case value is 0.02 cm).

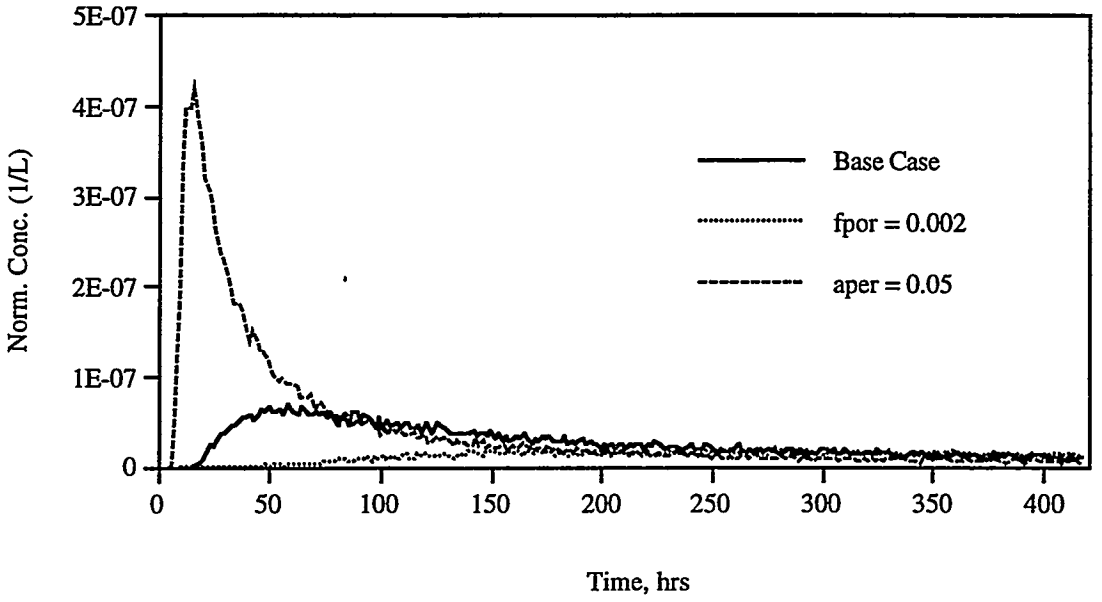

Figure C.19. Breakthrough curves of sorbing tracer between C#2 and C#3 with 200 gpm production and 20 gpm recirculation. "fpor = 0.002" denotes fracture porosity of 0.002 (base case value is 0.001), and "aper = 0.05" denotes average fracture aperture of 0.05 cm (base case value is 0.02 cm).

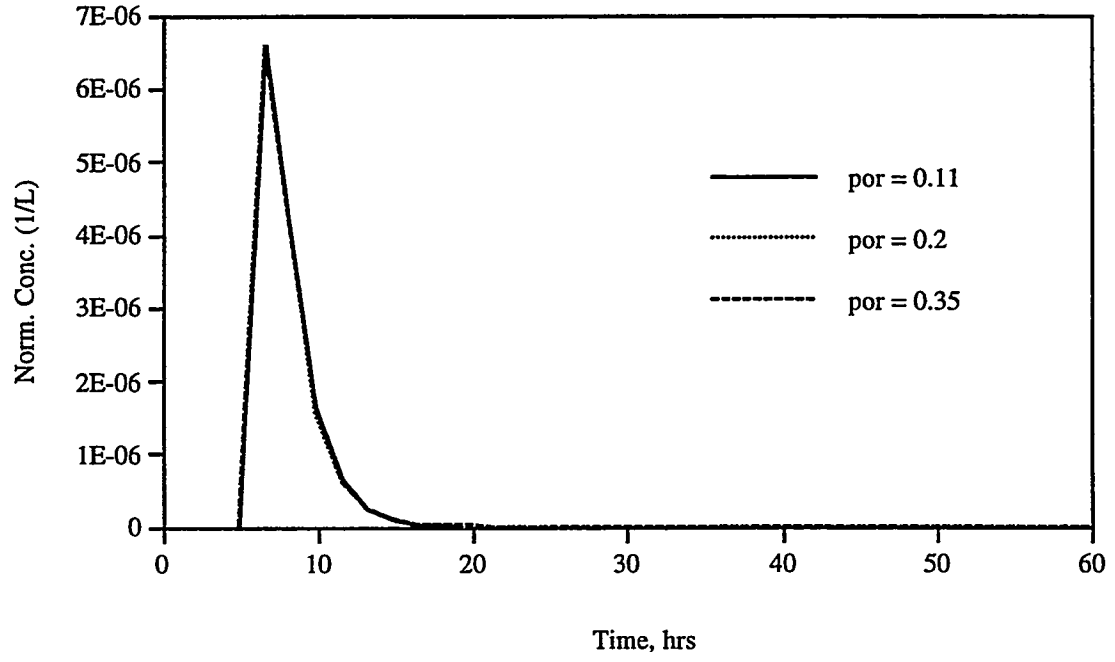

Figure C.20. Breakthrough curves of fracture-flow-only tracer as a function of matrix porosity for transport between C#2 and C#3 with 200 gpm production and 20 gpm recirculation.

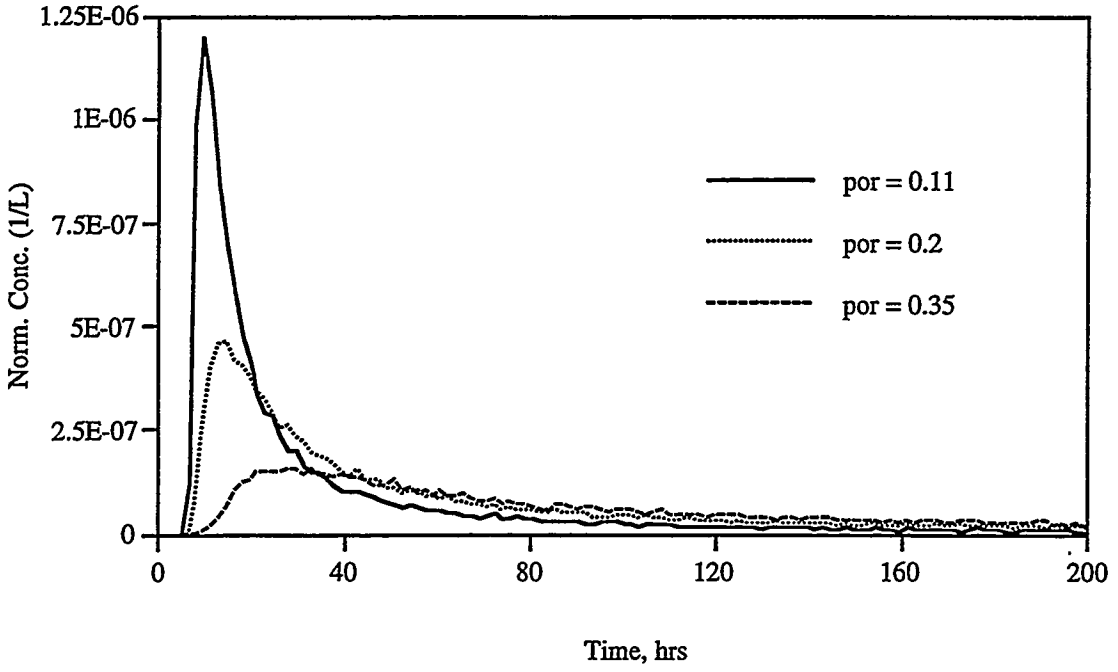

Figure C.21. Breakthrough curves of nonsorbing tracer as a function of matrix porosity for transport between C#2 and C#3 with 200 gpm production and 20 gpm recirculation.

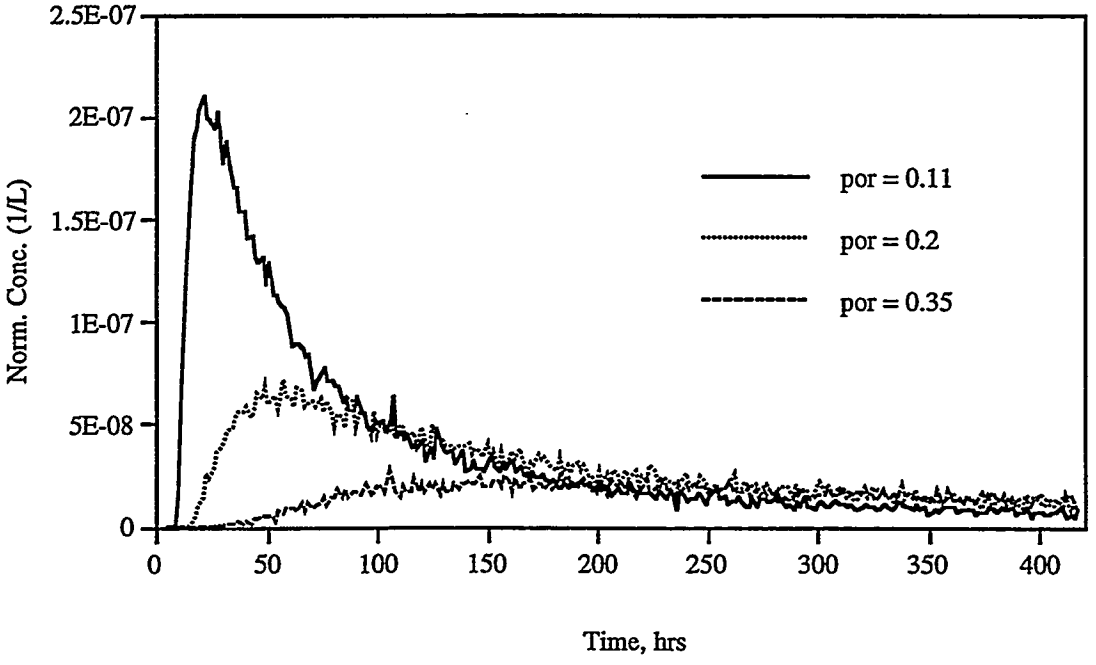

Figure C.22. Breakthrough curves of sorbing tracer as a function of matrix porosity for transport between C#2 and C#3 with 200 gpm production and 20 gpm recirculation.

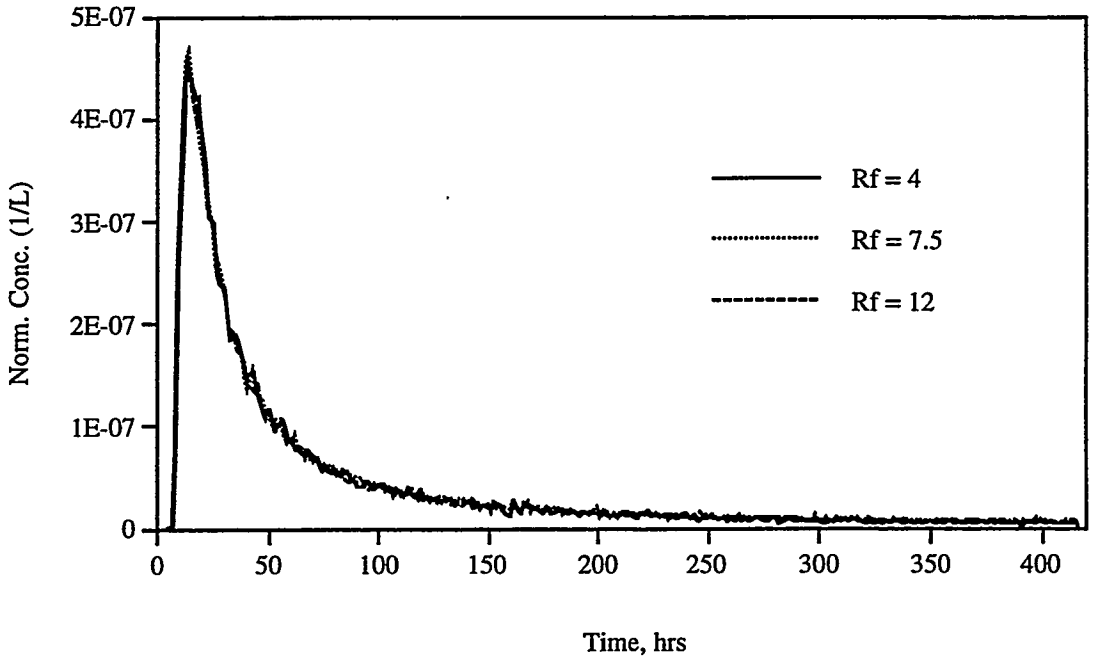

Figure C.23. Breakthrough curves of nonsorbing tracer as a function of retardation coefficient for transport between C#2 and C#3 with 200 gpm production and 20 gpm recirculation.

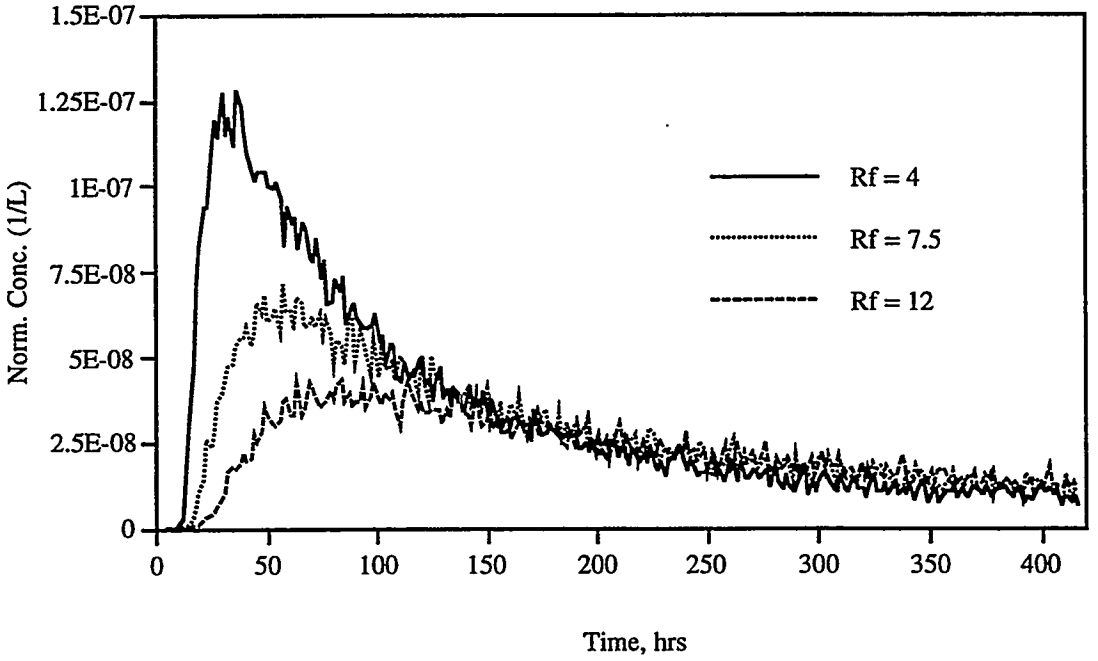

Figure C.24. Breakthrough curves of sorbing tracer as a function of retardation coefficient for transport between C#2 and C#3 with 200 gpm production and 20 gpm recirculation.

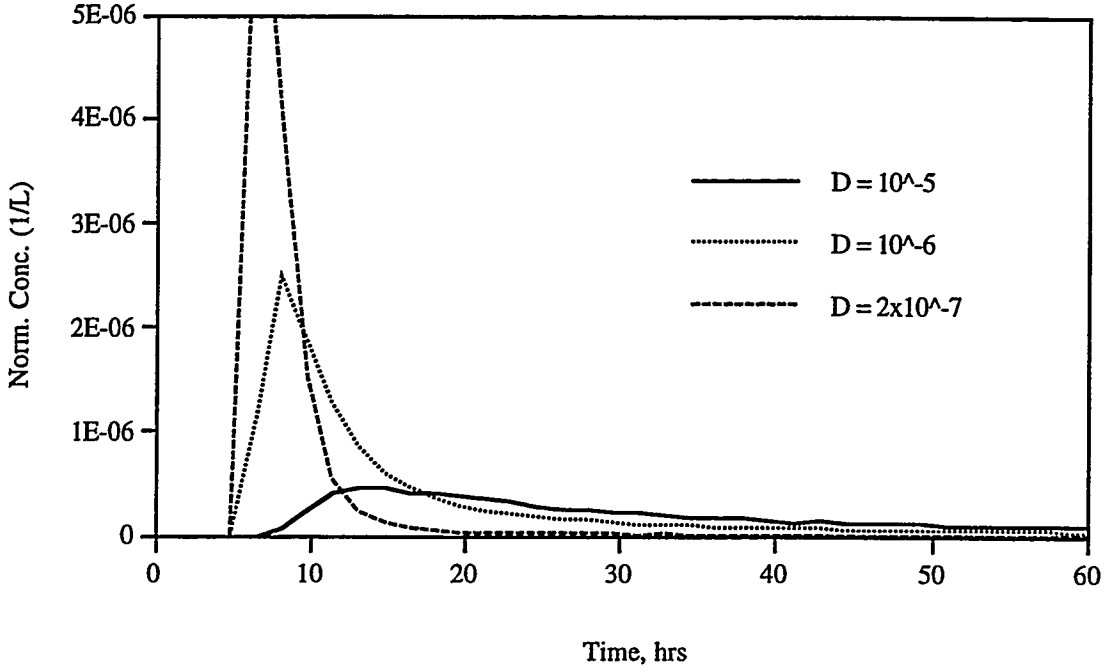

Figure C.25. Breakthrough curves of nonsorbing tracer as a function of free diffusion coefficient for transport between C#2 and C#3 with 200 gpm production and 20 gpm recirculation.

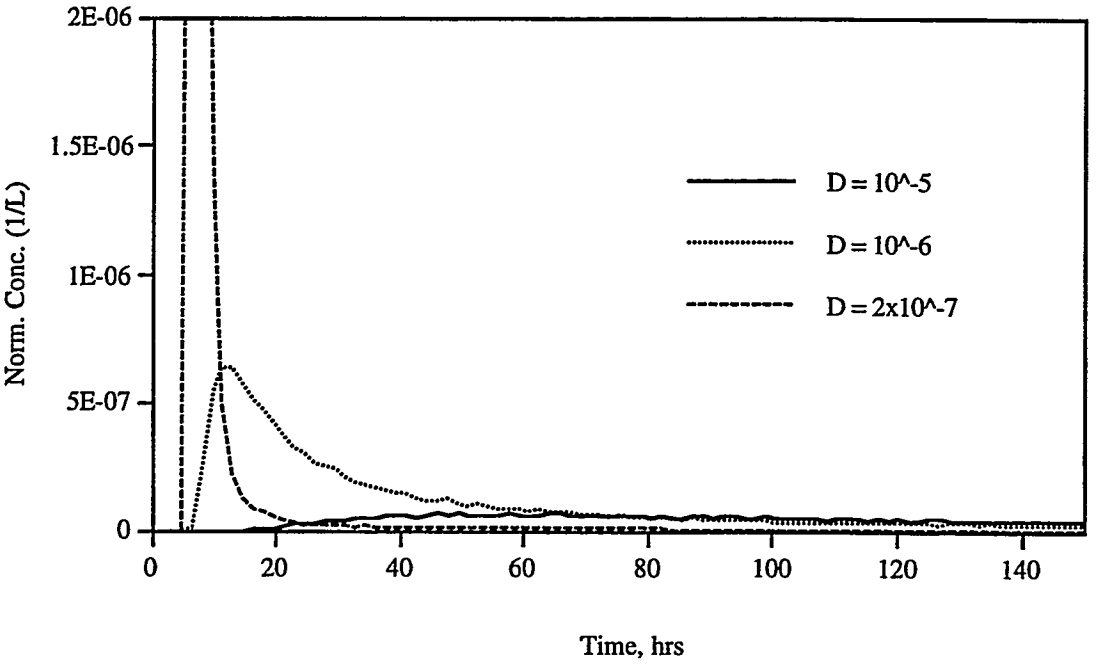

Figure C.26. Breakthrough curves of sorbing tracer as a function of free diffusion coefficient for transport between C#2 and C#3 with 200 gpm production and 20 gpm recirculation.

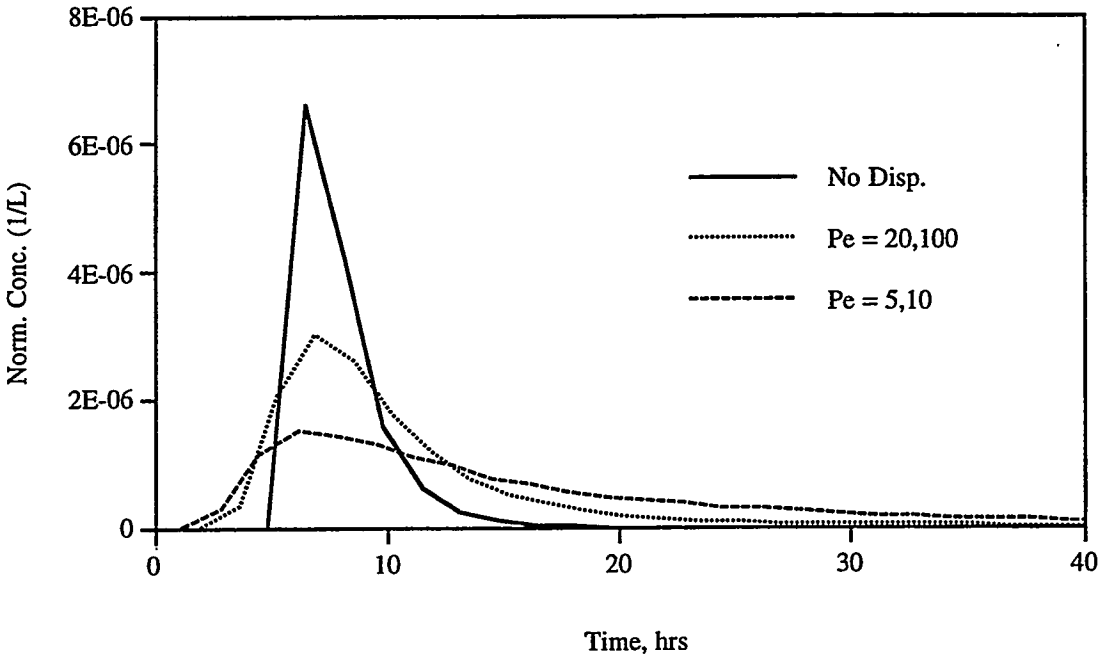

Figure C.27. Breakthrough curves of fracture-flow-only tracer as a function of Peclet number(s) for transport between C#2 and C#3 with 200 gpm production and 20 gpm recirculation.

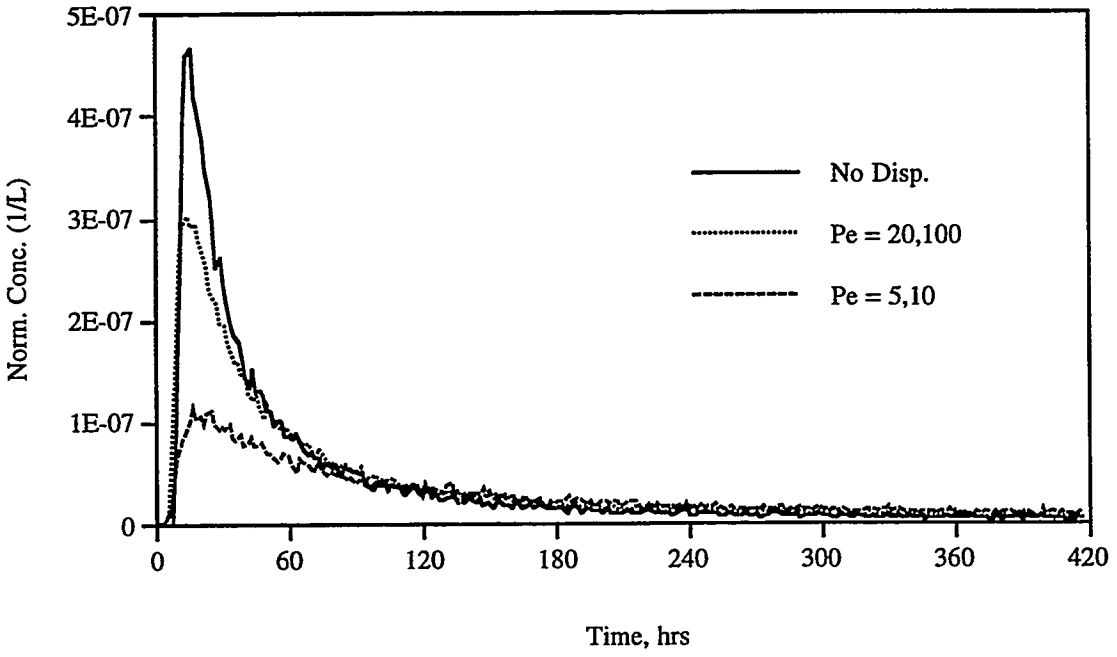

Figure C.28. Breakthrough curves of nonsorbing tracer as a function of Peclet number(s) for transport between C#2 and C#3 with 200 gpm production and 20 gpm recirculation.

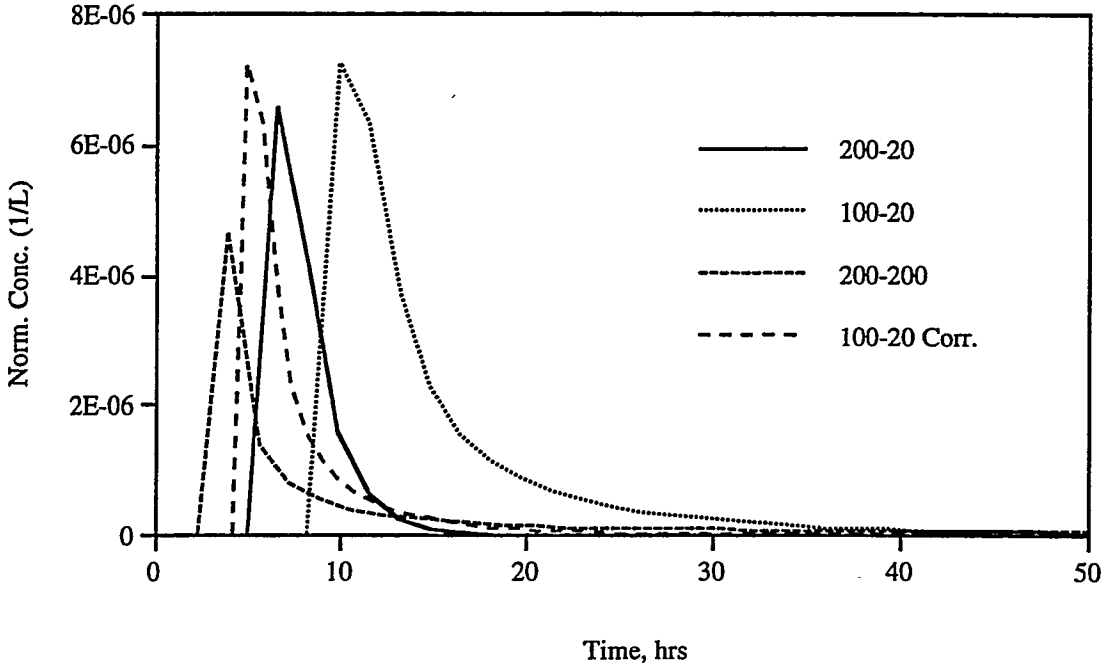

Figure C.29. Breakthrough curves of fracture-flow-only tracer for different injection/ production strategies between C#2 and C#3. See text for discussion of curves.

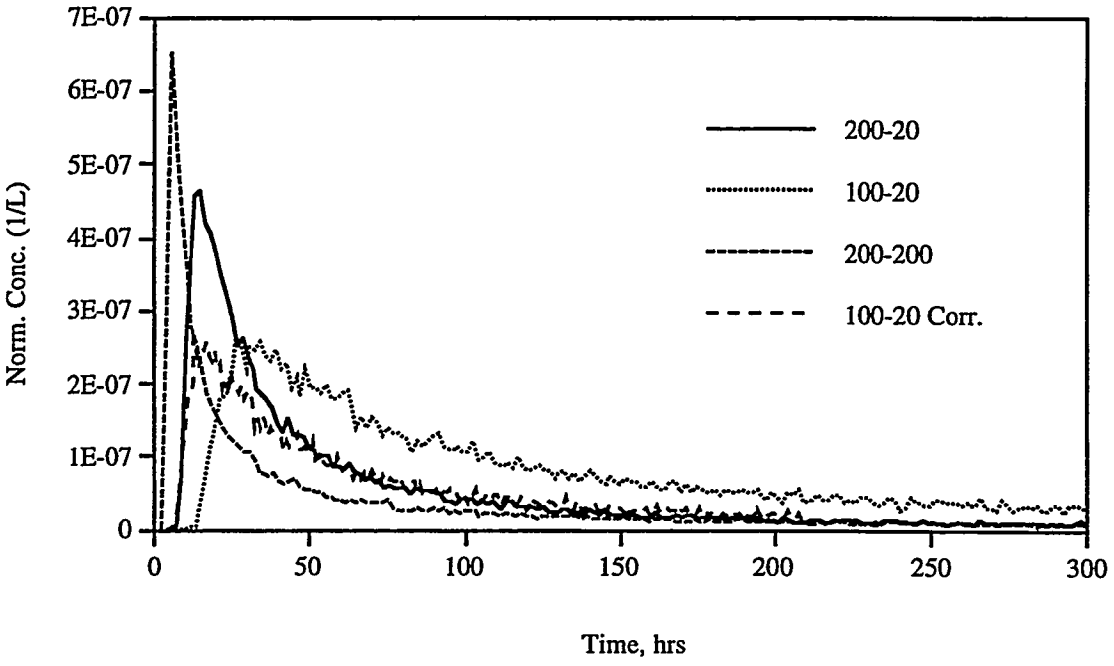

Figure C.30. Breakthrough curves of nonsorbing tracer for different injection/production strategies between C#2 and C#3. See text for discussion of curves.

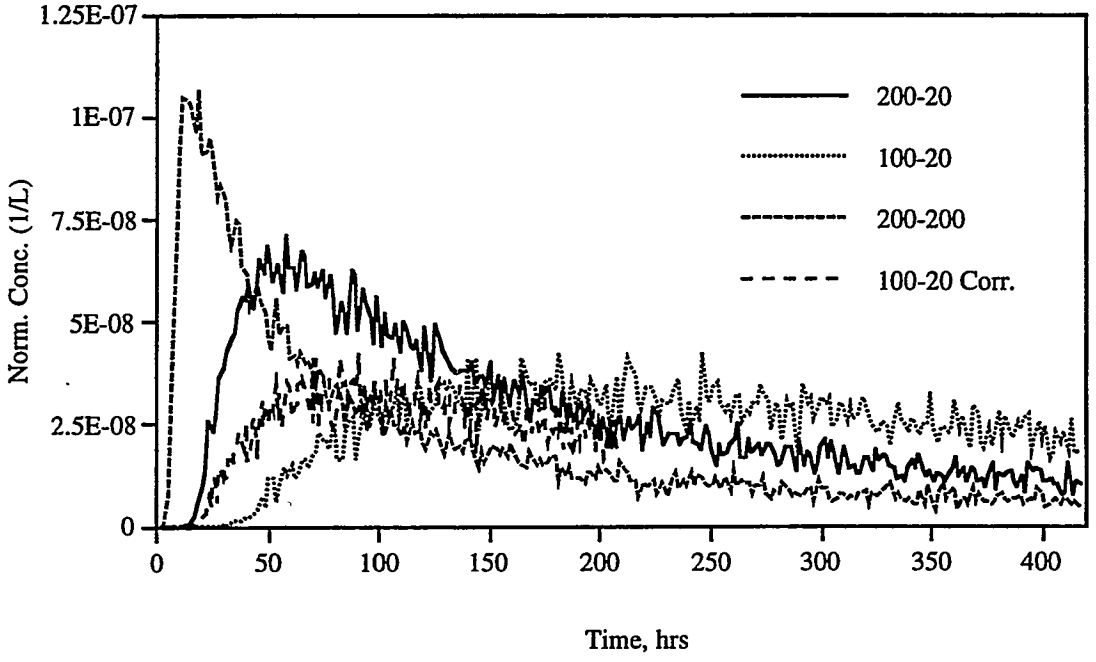

Figure C.31. Breakthrough curves of sorbing tracer for different injection/ production strategies between C#2 and C#3. See text for discussion of curves.

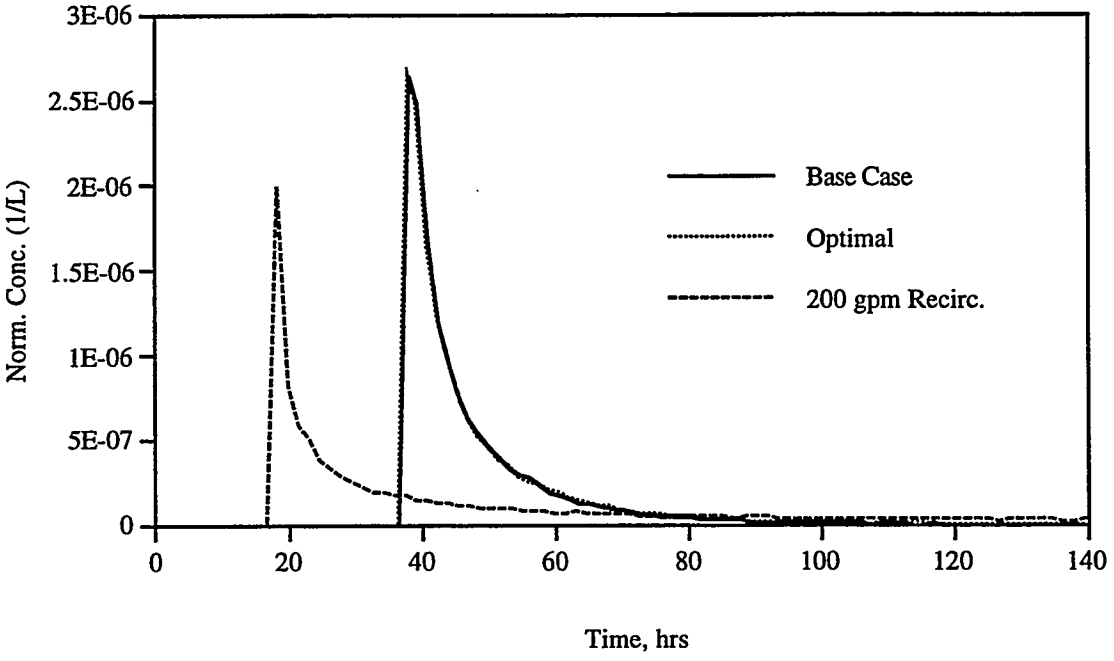

Figure C.32. Breakthrough curves of fracture-flow-only tracer for base case, "optimal" formation parameter values, and full recirculation at 200 gpm for transport between C#1 and C#3. See text for discussion of curves.

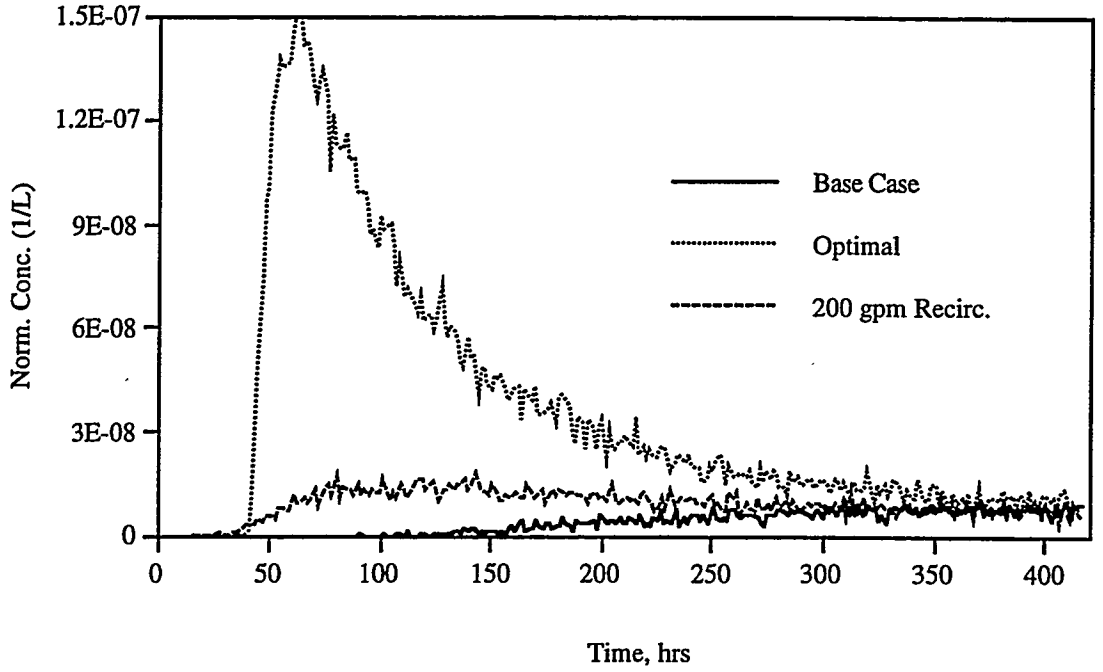

Figure C.33. Breakthrough curves of nonsorbing tracer for base case, "optimal" formation parameter values, and full recirculation at 200 gpm for transport between C#1 and C#3. See text for discussion of curves.

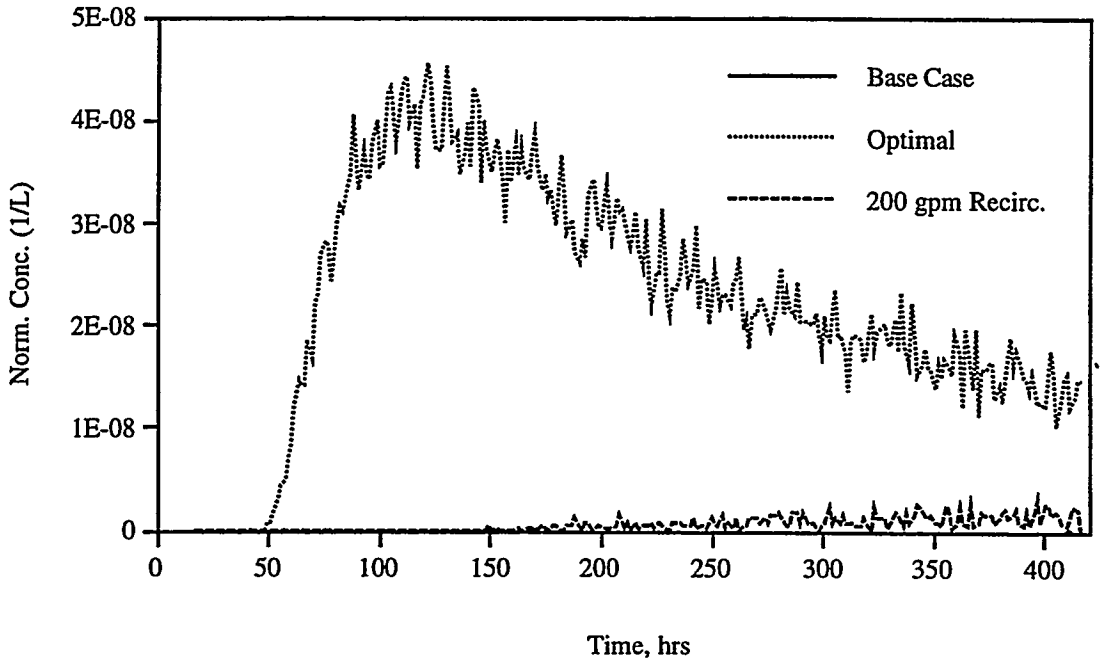

Figure C.34. Breakthrough curves of sorbing tracer for base case, "optimal" formation parameter values, and full recirculation at 200 gpm for transport between C#1 and C#3. See text for discussion of curves.

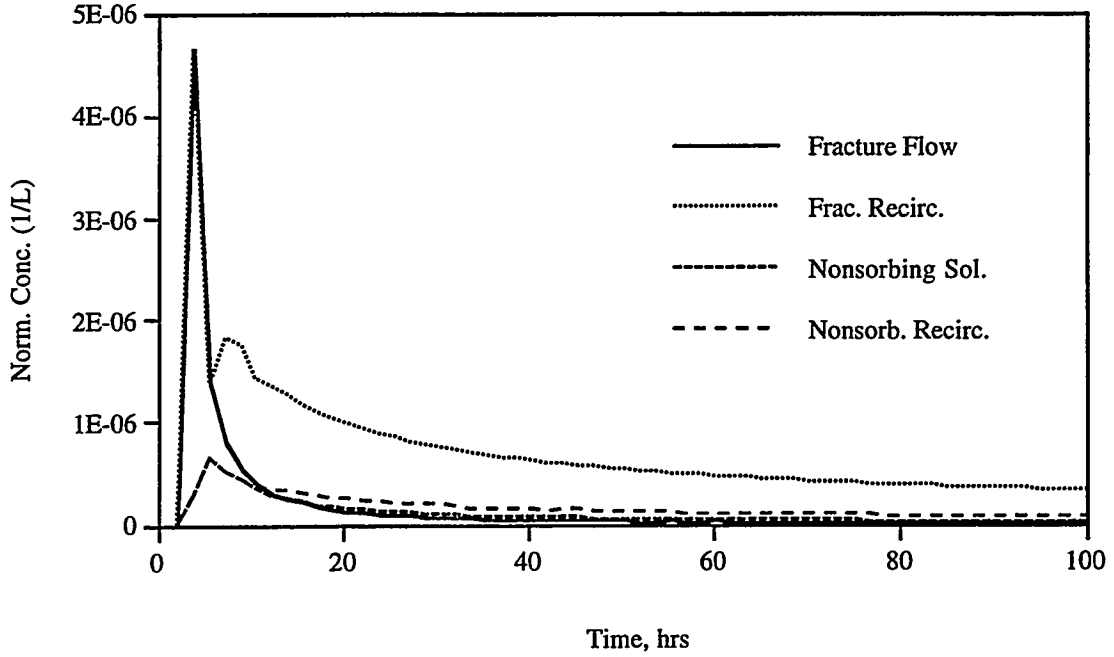

Figure C.35. Breakthrough curves of fracture-flow-only and nonsorbing tracers for full recirculation at 200 gpm between C#2 and C#3 showing the effects of recirculation on apparent tracer recoveries.